信州大学審査学位論文

Synthesis and Characterization of Nano-Structured Amorphous Inorganic Oxides

March, 2012

Wataru   Shimizu

Contents

CHAPTER   1

General Introduction

1.1. General Synthetic Approaches to Nanostructured Materials

Nano-size materials are generally characterized by their morphology; i.e. nanoparticles[1-3], nanofibers[4-6], and nanosheets[7-9] Such nanomaterials are the basic building blocks that constitute porous inorganic structures.[10-12] Nanostructured inorganic materials have been synthesized by finely-controlled bottom-up approaches such as solution based synthesis or physical vapor deposition.[13] The sol–gel technique is an example of a bottom-up fabrication method based on solution chemistry. It has widely been used to prepare inorganic polymers, which can be subsequently converted to inorganic oxides under milder conditions than other synthetic techniques.[14-17] As the nanostructure can be controlled in atomic to molecular regime under

rmild conditions, the sol-gel technique has versatility in the form of the final product, allowing fabrication of thin to thick films, particles and monoliths. The sol–gel technique has a long history, dating back to the beginning of the 19th century, and chemists have used this technology for almost a century now. It was introduced in the process of oxide film preparation by Geffcken in a patent applied in 1939. Schott glass company (Germany) further developed this process and successfully used it as optical coatings for glass in the 1960s.[18] From the middle of 1980s, various catalysts for the sol-gel reaction was studied, allowing better control over the shape of solid materials, e.g., particles, fibers, monoliths and so forth. Sol-gel synthesis of inorganic oxides, such as SiO_2,[19] TiO_2,[20] Al_2O_3,[21] ZrO_2,[22] Nb_2O_5[23] and their composites, have been studied in detail with a wide range of applications.

Inorganic polymers prepared by sol-gel techniques can be converted into materials other than oxides; for example, nitrides and carbides. Metallic frameworks can also be synthesized from such inorganic polymers by reduction of ionic species. Platinum group metals can be readily reduced by chemical reduction,[24,25] allowing fabrication of various nanostrucutured metals, with most emphasis on metal nanoparticle synthesis.

1.2. Synthetic Approaches

1.2.1. Three Dimensional Nanostructure

Porous materials composing nano-sized pore structure are recognized as a typical three dimensional (3-d) nanostructure material. On the other hand, dense materials who have little pores can be also dealt with as a 3-d nanostructure material. Unless the sintering process is conducted at a high temperature, the sol-gel process is able to use as an advantageous method for the fabrication of porous solid materials. The polymeric precursors are synthesized by hydrolysis and polycondensation reactions of metal alkoxides or metal salts, e.g., chlorides, nitrates and acetates.[14] Inorganic oxide solids are fabricated via drying and heating processes of the precursor sols comprising inorganic oxide polymers. For instance, a metal oxide thin film possessing nanostructure like

nano-porous can be obtained by dip or spin coating of sols produced from a reaction–controlled sol–gel process.[14,26-29]

1.2.1.1. Porous Structures

Aluminum oxide (alumina), which has multiple crystalline structures, is famous for a porous material possessing a number of nano-sized pores in a matrix, referred to such as α-, β-, and γ-alumina. Alumina is fabricated from aluminum hydroxide purified from bauxite with high temperature calcination (T >1000 °C). Pore-sizes are generally affected by the size of precursor nanoparticles of aluminum hydroxide (Scheme 1.1).

As for the sol-gel process, silicon dioxide (silica) is the most common material. In addition to the wide range of applications of silica, the slow rate of hydrolysis of silicon alkoxide allows easy manipulation of precursor synthesis. In light of applicative aspects, silica is commonly used in a porous form, owing to fundamental properties, such as chemical and thermal stability, mechanical strength, availability, not to mention that it is an environmental benign material. Many approaches have been suggested to generate pores in the form of xerogels, aerogels or particles (Table1.1).[19,30-38]

Monolithic porous silica consists of a solid skeleton and voids in the gel structure. Pore formation is usually controlled by molecular templating techniques using organic-functionalized silicon alkoxides[39-42] or additives such as polymers and surfactants[43-47] (Scheme 1.1). Heat treatment above 400 °C is often necessary for these synthetic methods to remove the organic species, resulting in inevitable collapse of pores. Development of alternative processes to fabricate monolithic porous silica without calcination is desired.

Table 1.1.   Selected synthesis routes to porous silica.

Sources	Catalysts	Template Agents	T^a (°C)	d^b (nm)	V_p^c (%)	Remarks	Ref.
TEOS	HCl	Fluorocarbon	600	0.7			45
PMSSQ	PPG	tCD	430	~ 1.0	63	Aero gel	48
VTES, MTES	NH$_4$OH	CTAB	550	1.3	20		43
TEOS	HCl	C$_{12}$TAC	600	1.7			44
SSQ		tCD	420	1.7	20		47
VTES, MTES	NH$_4$OH	CTAB	550	2.1	43		43
TMOS	HCl	[C$_4$mim]$^+$BF$_4$	90	2.5			33
TEOS	HNO$_3$		105	3.4	5		36
TEOS	HCl	Tween80	400	4.2	58		49
TEOS	HCl	Pluronic F127	550	~6.5			50
TEOS	NH$_3$		105	9.4	49	Particle-like	36

^{a} Calcination temperature. ^{b} Average pore diameter . ^{c} Pore volume fraction. tCD: heptakis (2,3,6-tri-O-methyl)-β-cyclodextrin, CTAB: cetyltrimethylammonium bromide, C$_{12}$TAC: dodecaalkylammonium chloride, [C$_4$mim]$^+$BF$_4$: 1-butyl-3-methyl-imidazolium-tetrafluoro -borate, Tween80; polyoxyethylene sorbitan monooleate, Pluronic F127: poly-(ethylene oxide)-b-poly(propylene oxide)-b-poly(ethylene oxide).
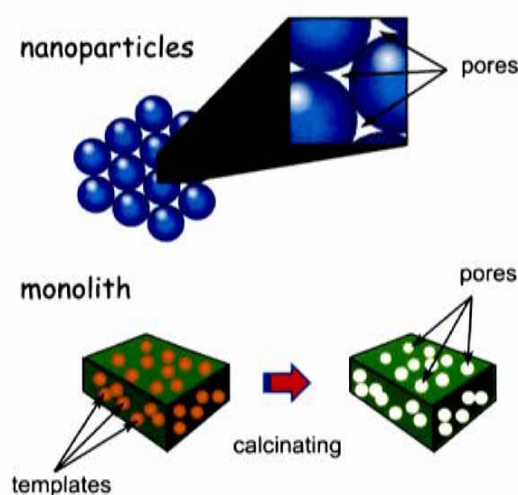
Scheme 1.1.   Images of pore formation with nanoparticles and templates in monolithic structure.

When targeting the precise control of the pore size and its uniformity aimed at the silicous materials without using the templates, the geometry control of the precursor polymers with an optimized hydrolysis/condensation reaction represents a challenge. It is established that use of a base catalyst in sol–gel process produces highly branched Si-O polymer networks that easily create voids among them (Scheme 1.2).[14] This leads to mesopore (2 nm $< d <$ 50 nm) or macropore ($d >$ 50 nm) formation[51] due to the fact that the void size, i.e., pore diameter, is governed by the particle geometry, size and packing.[14,52,53] On the other hand, the use of acid catalysts produces weakly branched silica precursor polymers characterized by a low–fractal dimension.[14,54-57] Polymers with a low-fractal dimension should produce a dense monolithic structure with no large pore formation (Scheme 1.2). Micropores ($d <$ 2 nm) are usually produced via an acid-catalyzed system, while the pore volume is not necessarily large.

1.2.1.2. Dense Structures

The physical properties of solid are influenced by the density of the material after drying or heating. The structure of polymeric matters depend on the primary conformation of the precursor polymers in the solution, i.e., either a low–fractal dimension (weakly–branched) structure or high–dimensional (highly–branched) one.[14] The density of the heat treated solids should reflect the geometry of initial precursor structure, in particular, for materials that are heat treated at low temperatures. In other words, weakly–branched polymeric precursors are expected to provide a dense solid, while highly-branched structures should lead to a low density, porous solid (Scheme 1.2). The dimensionality of polymers during growth is determined by the hydrolysis and polycondensation rate, which depends on the metal species. For example, silicon alkoxides have slow hydrolysis rate and fast polycondensation rate, whereas transition metal alkoxides such as titanium alkoxide are easily hydrolyzed but the polycondensation rate is slow. Most titanium alkoxides are easily attacked by water, thus producing highly-branched particle-like polymer aggregates resulting in porous structures. Thus, dense solids are prepared by further heat treatment at high temperatures to initiate necking and particle growth. In

other words, the synthesis of dense non-porous transition metal oxides via conventional sol-gel processes is not straightforward, and a method to prepare low–fractal dimension (weakly–branched) structure by inhibiting hydrolysis and/or enhancing polycondensation rate must be developed.
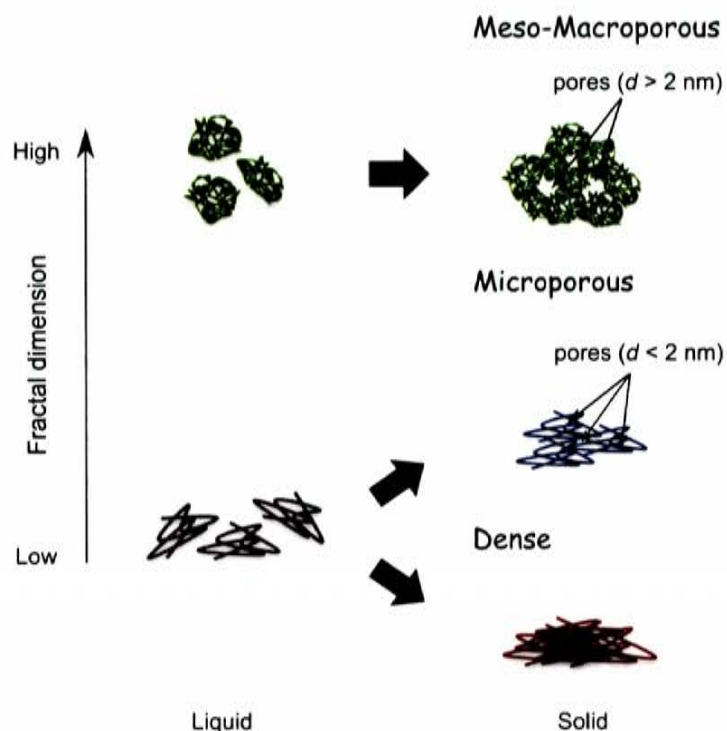
Scheme 1.2. Schematic showing the effect of conformation of liquid precursors (fractal dimension of polymeric precursors) and final product.

1.2.2. One Dimensional Nanostructure

Owing to their unique geometries, one dimensional (1-d) nanostructured materials often possess characteristic properties that are not observed in bulk. Various 1-d nanostructures such as nanowires and nanotubes have been fabricated from diverse materials by the solution based synthesis. Use of templating agents, e.g., cetyltrimethylammonium bromide (CTAB),[58] lyotropic liquid crystal,[59] sorbitan monostearate (Tween60), and nonaethyleneglycol dodecylether ($C_{12}EO_9$),[59] have been conducted for the preparation of 1-d

platinum nanostructures (Scheme 1.3). The metal complex in the 1-d nanostructure can be easily reduced by a reductant such as NaBH$_4$, producing nanostructured platinum.[58,60]
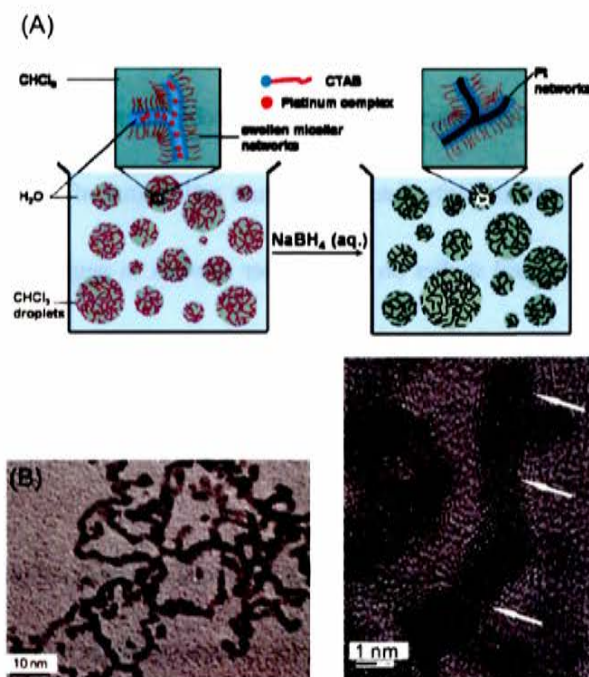
Scheme 1.3. Scheme of platinum nanowire formation by using sodium borohydride and TEM images of resulting platinum nanowire. Reprinted from ref. 58(A), (B) and 60(C). The grain boundaries are highlighted by the arrows (C).

1.3. Characterization of Polymeric Nanostructure

In order to understand the relation between the nanostructure of solid and physical properties, the solid must be carefully characterized in the nanometer scale. The morphology can be visually recognized by transmission electron microscopy (TEM), scanning electron microscopy (SEM) and atomic force microscopy (AFM). The crystal structural is revealed by electron diffraction, X-ray diffraction (XRD) and grazing incidence x-ray scattering. The microscopic geometry of the precursor polymers is conducted by scattering techniques such as; dynamic light scattering (DLS), small angle neutron scattering (SANS) and small angle x-ray scattering (SAXS). Among the scattering techniques, SAXS has become a popular analytical tool to gather information on the polymeric materials in solution.

SAXS records elastically-scattered x-rays in low angles by nm-scale objects. Distance distribution functions estimated from the scattering intensities contains information regarding conformation, shape, sizes and periodicity. This method has long been used to investigate the structure of protein colloids, revealing long-range ordered structures and particulate structures. Strobl extended the SAXS analysis to general macromolecules, discussing self-similarity, internal structure and degree of swelling.[61] In sol-gel chemistry, SAXS has been used for structural studies on the polymer network in aggregation of silicious colloids and porous gels.[62-64] To explain the branched structure of polymeric sols, fractal dimension d_f was applied to polymeric silica precursor sols.[14,55,57,65,66] SAXS has recently been extended to the structural investigation of titania precursor polymers.[67-70]

As shown in Scheme 1.2, one can easily image that the fractal dimension of precursor polymers influence the nanostructures of resulting solid materials.[4,65] However, the relationship between conformations of precursor liquid polymers, nanostructures of solid materials and their physical properties of sol-gel derived inorganic polymers is still poorly defined. A detailed, systematic, and quantitative study is clearly necessary, especially since most SAXS studies on polymeric sols have not discussed scattering intensities normalized by absolute scale. Such studies is expected to advance material design in the nanoscale, identifying structure-property relations.

1.4. Application of Nanostructured Materials

1.4.1. Optical Thin Films

When light enters second medium with refractive index n_2 from first medium with refractive index n_1, both reflection and refraction of the light may occur at the interface of these media. A typical example of the reflection loss, also called Fresnel loss, is observed at an air-glass interface such as the end-face of an optical fiber. The reflectance affected by polarization of incident ray is explained by Fresnel equations on each s- and p-polarized ray. If the ray is normally incident on the plane, there are no difference between the s- and p-polarized rays. In this case, the reflectance is obtained from

$$R = \left(\frac{n_0 - n_s}{n_0 + n_s} \right)^2 \quad (1)$$

where n_0 and n_s are refractive indices of first and second media. The reflectance can be controlled by placing a third medium with a refractive index n_1 between the first and second media. As for this single-layer film model, the reflectance is described by

$$R = \left(\frac{n_1^2 - n_0 n_s}{n_1^2 + n_0 n_s} \right)^2. \quad (2)$$

When the reflectance is zero, reflection loss is the smallest. The optimum refractive index of the intermediate layer is deduced from

$$n_1 = \sqrt{n_0 n_s}. \quad (3)$$

For example, in the case of fused quartz ($n_s = 1.46$) in air ($n_0 = 1.0$), the optimum refractive index is $n_1 = 1.21$. From eq.(2) and (3), it is obvious that low refractive index materials (e.g., $1.15 < n_1 < 1.3$) are appropriate to reduce reflection, $R < 0.5\%$ (Fig.1.1). Low refractive index materials have been employed as antireflective (AR) thin films for optical applications including display devices, lenses and solar cells.[36,38,71-78]

For example, magnesium fluoride is a low-n ($n = 1.38$) material that is widely used in commercial applications (Table 1.2). The reflectance of the single-layer films is determined by the indices of the thin layer. Films with lower indices are desired for obtaining low reflection loss and high transmittance. High refractive index films

are used for optical devices, such as planar waveguides, dielectric multilayer mirrors, and interference filters.[77-85] High refractive index films are also used in combination with a low refractive index film for low reflectance films in a wide wavelength range.
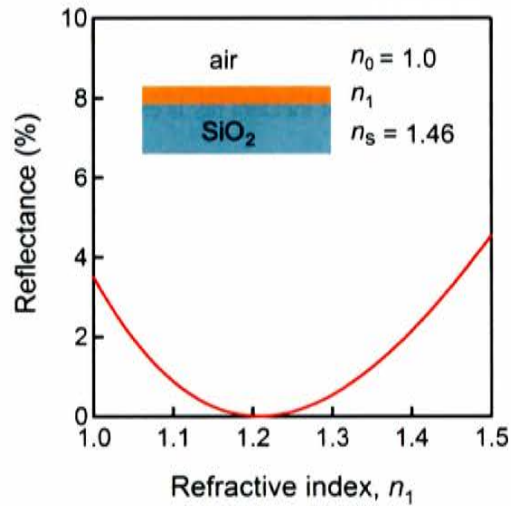
Figure 1.1. Reflectance of the model material composed of the single-layer film/SiO$_2$ plotted against the refractive index of the single-layer film, n_1.

Table 1.2. Typical Refractive Indices of Transparent Solid Materials in Visible Wavelengths.

Materials/Trade name	Chemical formula	n	λ (nm)	Remarks	Ref.
Water (ice)	H_2O	1.31	589		86
Sodium fluoride	NaF	1.32	633	Hygroscopic	87
Potassium fluoride	KF	1.36	633	Deliquescent	87
Magnesium fluoride	MgF_2	1.38	633		88
Fused quartz	SiO_2	1.46	589		89
Sodium chloride	NaCl	1.54	633	Hygroscopic	88
Aluminum oxide	Al_2O_3	1.66	633	Thin film (PVD[a])	90
Zirconium dioxide	ZrO_2	2.21	633	Thin film (PVD)	90
Niobium pentoxide	Nb_2O_5	2.32	633		91
Diamond	C	2.42	589		89
Titanium dioxide (rutile)	TiO_2	2.49	633		88
Lead titanate	$PbTiO_3$	2.67	633		88
Teflon® AF (fluoropolymers)	$(C_2F_4)_n$	1.315			92
Cytop (fluoropolymers)	$(C_2F_4)_n$	1.34			93
Poly(methylmethacrylate)	$(C_5H_8O_2)_n$	1.49	633		94
Polyethylene terephthalate	$(C_{10}H_8O_4)_n$	1.58			95
Polycarbonate	$(C_{16}H_{14}O_3)_n$	1.58	633		94
Polystyrene	$(C_8H_9)_n$	1.59	633		94

[a] Physical vapor deposition.

1.4.1.1. Low Refractive Index Materials

Due to high transparency in visible light, silica thin films have been applied to optical thin films. The refractive index of silica, $n=1.46$, is relatively low compared to other inorganic materials (Table1.2). The refractive index is influenced by pore volume of a bulk material, i.e., porosity, as described by a Lorentz-Lorenz equation

$$\left(1 - V_p\right) \times \left(\frac{n_1^2 - 1}{n_1^2 + 2}\right) = \left(\frac{n_f^2 - 1}{n_f^2 + 2}\right) \quad (4)$$

where V_p is the volume fraction of pores, n_1 and n_f are refractive index of a framework materials composing a film and a porous film, respectively. According to this equation, lower indices of silica matrices would be attained by incorporation of nanosized pores filled with air, $n_0 = 1.0$, increasing their porosity. Increasing the content of nanosized pores is generally expected to greatly deteriorate the mechanical strength of the film.[35] Consequently, many studies[96-100] have investigated reinforcement of porous silica (Table 1.3).

Table 1.3. Optical and Physical Properties of Sol–Gel Derived Porous SiO_2 Thin Films.[a]

Source	d (nm)	n	V_p (%)	t (nm)	E (GPa)	T (°C)	Remarks	Ref.
TEFS		1.19	52	150–400	5.0	–	Fluorosilane, Aerogel	98
TEOS		1.22	48		6.0	400		100
TEOS MTEOS	~10	1.22		82		450	Templates (Pluronic F127)	101
TEFS	20	1.24	40	150–400	14	–	Fluorosilane	98
TEOS	4.2	1.25		–	9.2	400	Templates (Tween80)	49
SSQ	10–20	1.27	34		3.9	420	Templates (bCD)	38
TEOS		1.28	35	–	16.6	400	Particles and templates	100
MSQ		1.29		–	1.8	425		102
TEOS		1.32	~28	~450	–	550	Templates (Pluronic F127)	32

[a] Notation: d, average pore diameter; n, refractive index; λ, wave length; t, film thickness; E, elastic modulus (Young's modulus); T, heating temperature. bCD; heptakis (2,3,6-tri-O-benzoyl)-β-cyclodextrin.

1.4.1.2. High Refractive Index Materials

Titania is a typical example of a high refractive index material. This titania films that are transparent in the visible light region are thus one of the most promising candidates for optically–functionalized films exhibit high refractive indices. Anatase and rutile forms exhibit $n = 2.54$ and 2.75 at $\lambda = 550$ nm, respectively. Amorphous

titania has considerably lower n values; highest reported values are around n=2.2.[103] Nevertheless, amorphous

titania is still preferable for optical films to suppress multiple light scattering[103] because polycrystalline titania

films will always have grain boundaries and particles having various anisotropic orientation, which induces

birefringence of the films. Additionally, when one needs to use plastic substrates, polycrystalline titania are

unfavorable because of its photocatalytic activity that may decompose the substrates.

Amorphous titania thin films can be deposited by spin or dip coating of a solution prepared via the sol–gel

process.[27-29,104-111] Resulting films are formed at room temperature under atmospheric pressure. Such mild and

moderate condition should be useful when one targets the use of plastic substrates. However, when fabricated

without high temperature calcination, porous amorphous titania thin films are obtained. The apertures between

the particle-like structures of amorphous titania precursors constitute the pores, resulting in a decrease in the

refractive index. In order to increase the refractive indices of amorphous titania films, dense films containing a

reduced amount of air must be derived from precursors having suitable conformations.

1.4.2. Hydrophilic Coatings

Hydrophilic coatings have been used for anti-fogging, self-cleaning and enhancement of heat-transfer

efficiency. With respect to organic materials, polyalcohol and fatty acid ester serve as an anti-fogging agent, and

has been widely used in food packages. Inorganic hydrophilic coatings have the advantage in terms of

durability of the coating. Titania has attracted attention due to its superhydrophilic properties (contact angle,

θ<5°) which is caused by the photocatalytic activity.[112] The drawback of hydrophilic titania coatings is that heat

treatment is necessary to convert the film into the active crystalline phase, and that superhydrophility is lost in

the absence of UV light. Silica also can provide hydrophilic nature without UV light radiation; however its

hydrophilicity is not enough (typically θ>10°).

It is known that the surface topology of thin films affect the hydrophilicity or hydrophobicity. According to

the Cassie-Baxter equation,[113] if the pores of a film is filled with air, hydrophobicity is enhanced, while

hydrophilicity is increased when the pores are filled with water. Thus, hydrophilic/hydrophobic properties are influenced by size and the number of pores exposed on surface of thin films.

1.5. Aim of Thesis

The nanostructured materials promise development of distinguishing properties different from that of bulk structures. For the application perspective, nanostructure design is important to develop physical properties what we want. In general, nanostructures of solid materials are controlled by a synthesis condition. The resulting solids are closely researched on relationship between their nanostructures and properties.

On the solution based synthesis for nanostructured material, we can consider two-step: growth of precursor polymers in solution and formation of solids from the solution by drying (Scheme 1.4). In this process, conformation of the precursor polymers probably influences design of nanostructures of the solid materials, also affecting physical and chemical properties. The present study focuses on manifestation of relations ranging from conformation of precursor polymers to nanostructures of resulting solids and their diverse properties.

Here, nanostructured materials will be fabricated by the sol-gel technique as a solution based synthesis. Solid materials fabricated via the sol-gel process using metal alkoxide as a starting reagent are typified by silica, titania and alumina. In this work, sample fabrication is conducted by using silicon alkoxide having slow hydrolysis and titanium alkoxide having fast hydrolysis. The nanostructures of solids are controlled by the conformations of precursor liquid polymers derived from each of those alkoxides. Additionally, platinum precursor polymers are synthesized via a polymerized complex process being a type of the sol-gel technique, producing 1-d networked platinum whose nanostructure reflects a precursor geometry. This research also demonstrates that the resulting nanostructured materials have excellent properties on optical, mechanical and electrochemical characteristics, which are definite advantages over conventional materials. Definitions of the structural relationships, which are the goal of this work, would contribute to the development of synthesis

technique and design of various nanostructured materials. In terms of synthesis and applications of silica, titania

and platinum materials, detailed targets of each chapter are outlined in the following description.
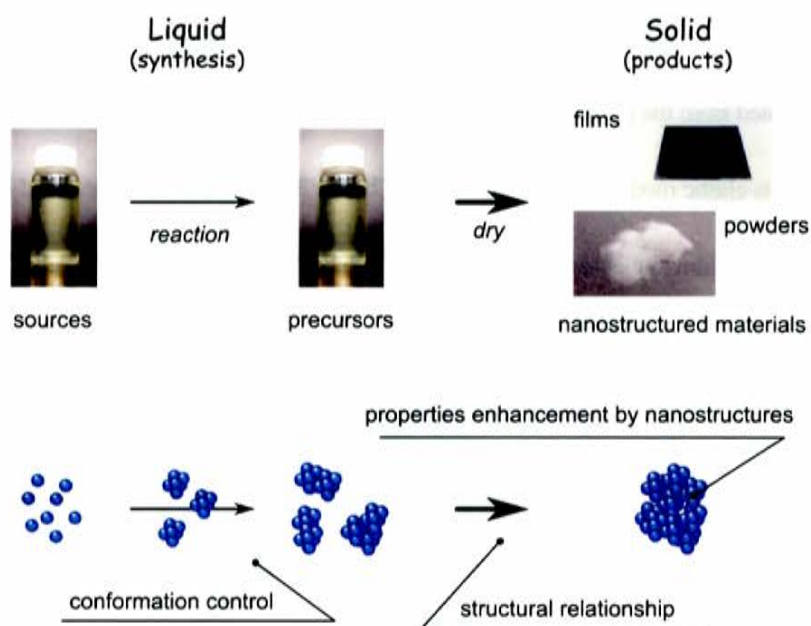
Scheme 1.4. A scheme of nanostructured materials fabrication and points of focus on this study.

Chapter 2 will present fabrication of microporous silica from tetramethyl orthosilicate (TMOS) using a

catalytic sol–gel process based on the non–ionic hydroxyacetone catalyst. Small angle X-ray scattering (SAXS),

nitrogen adsorption porosimetry, and transmission electron microscope (TEM) allowed to observe the whole

structural evolution. SAXS is certainly a suitable technique to confirm the generation of weakly–branched

polymeric objects because one can easily distinguish such low–fractal dimension characteristics from those of

high fractal dimension or globular particle–like objects ($d_f \approx 3$) owing to their markedly different scattering

behavior. Furthermore, a set of the structural parameters describing the geometry of the polymer chains, e.g.,

the radius of gyration reflecting the extent of the spatial distribution of the polymer chains, the fractal dimension

corresponding to the internal self–similarity, the correlation length often referred to as the mesh size of the

transient polymer network, and the persistent length related to the internal flexibility of the polymer chains, can

be evaluated from the measured scattering intensity. The data demonstrate the influence of conformation and microstructure, i.e., mesh–size, of liquid precursor polymers aggregates on pore structures of resulting silica.

From the perspective of an applicative aspect of porous silica, refractive indices of the microporous silica thin films fabricated from the precursor solution are characterized by means of spectroscopic ellipsometry, and simultaneously, its elastic modulus is investigated (in Chapter 3). Here it demonstrates that the advantage of the micropores silica thin film in mechanical strength that is obvious drawbacks of porous silica.

The evolution of superhydrophilicity on the microporous silica film is discussed in Chapter 4. In this section, it demonstrates that the apparently smooth and microporous surface can be readily formed below 80 °C not from silica nanoparticles or silicon alkylalkoxide, but from low–fractal dimension polymeric silica precursor derived from tetramethyl orthosilicate with the hydroxyacetone catalyst. The superhydrophilic coating on a polyethylene terephthalate (PET) substrate prevents water droplets from forming on the surface.

As for amorphous titania material, Chapter 5 will demonstrate rapid generation and growth of low–fractal dimension titanium oxide polymers in the precursor solution derived from titanium-n-butoxide via the catalytic sol-gel process with the hydrazine monohydrochloride catalyst by mean of time-resolved small angle X-ray scattering (Tr–SAXS). In order to obtain a transparent sol or gel with no organic stabilizer for titanium alkoxides, previously, it takes a very long time (>1 month) before the low–fractal dimension polymers are grown. Results exhibited here realize the efficient fabrication of the low–fractal dimension titanium oxide polymers, highly transparent solutions.

Chapter 6 will offer the fabrication of an amorphous dense titania film with a high refractive index from low–fractal dimension titanium oxide precursor solutions below 60°C, overcoming negatives of sol–gel derived titania solids revealed in previous studies, i.e., creation of void space or inhomogeneous grains, high heating temperature, and side effects of an organic residue. Furthermore, it is revealed that the correlation length confirmed from the liquid polymers influences the dense structure of the resulting solid film. Also, a successful

production of a high refractive index amorphous TiO_2 film ($n > 2.0$) on poly(methyl methacrylate) (PMMA) substrates is shown.

Applicative study of platinum nanowire network is shown in Chapter 7. The platinum precursors are produced by the polymerized complex process being a type of the sol-gel technique, and the platinum nanowire network is created by the hydrogen reduction of dried precursor powders. The platinum nanowire network is supported on silica nanoparticles. The large electrically-conductive network of crystalline platinum enables to use insulating inorganic oxides like silica.. The high chemical stability of silica improves durability of the catalyst for the oxygen reduction reaction.

References

1. Bruchez, M.; Moronne, M.; Gin, P.; Weiss, S.; Alivisatos, A. P. Science 1998, 281, 5385.

2. Poizot, P.; Laruelle, S.; Grugeon, S.; Dupont, L.; Tarascon, J. M. Nature, 2000, 407, 6803.

3. Daniel, M. C.; Astruc, D. Chem. Rev. 2004, 104, 293.

4. Li, D.; Wang, Y. L.; Xia, Y. N. Nano Lett. 2003, 3, 1167.

5. Xu, C. X.; Sun, X. W.; Chen, B. J. Appl. Phys. Lett. 2004, 84, 1540.

6. Kim, I. D.; Rothschild, A.; Lee, B. H.; Kim, D. Y.; Jo, S. M.; Tuller, H. L. Nano Lett. 2006, 6, 2009.

7. Sasaki. T.; Ebina, Y. Kitami, Y.; Watanabe, M.; Oikawa, T. J. Phys. Chem. B 2001, 105, 6116.

8. Omomo, Y.; Sasaki, T.; Wang, L. Z.; Watanabe, M. J. Am. Chem. Soc. 2003, 125, 3568.

9. Liang, Z. H.; Zhu, Y. J.; Hu, X. L. J. Phys. Chem. B 2004, 108, 3488.

10. Kresge, C. T.; Leonowicz, M. E.; Roth, W.J.; Vartuli, J. C.; Beck, J. S. Nature 1992, 359, 710.

11. Zhao, D. Y.; Feng, J. L.; Huo, Q. S.; Melosh, N.; Fredrickson, G. H.; Chmelka, B. F.; Stucky, G. D. Science 1998, 279, 548.

12. Davis, M. E. Nature 2002, 417, 813.

13. Xi, J. Q.; Schubert, M. F.; Kim, J. K.; Schubert, E. F.; Chen, M. F.; Lin, S. Y.; Liu, W.; Smart, J. A. Nature Photonics 2007, 1, 176.

14. Brinker, C. J.; Scherer, G. W. In Sol–gel Science, The Physics and Chemistry of Sol–gel Processing, Academic Press: New York, 1990.

15. Lev, O.; Wu, Z.; Bharathi, S.; Glezer, V.; Modestov, A.; Gun, J.; Rabinovich, L.; Sampath, S. Chem. Mater. 1997, 9, 2354.

16. Zhong, Z. Y.; Yin, Y. D.; Gates, B.; Xia, Y. N. Adv. Mater. 2000, 12, 206.

17. Caro, J.; Noack, M.; Kölsch, P. Schäfer, R. Micropore Mesopore Mater. 2000, 38, 3.

18. Schroeder, H. Phys. Thin Films 1969, 5, 87.

19. Beck, J. S.; Vartuli, J. C.; Roth, W. J.; Leonowicz, M. E.; Kresge, C. T.; Schmitt, K. D.; Chu, C. T. W.; Olson, D. H.; Sheppard, E. W.; Mccullen, S. B.; Higgins, J. B.; Schlenker, J. L. J. Am. Chem. Soc. 1992, 114, 10834.

20. Wang, C. C.; Ying, J. Y. Chem. Mater. 1999, 11, 3113.

21. Tadanaga, K.; Katata, N.; Minami, T. J. Am. Ceram. Soc. 1997, 80, 1040.

22. Patra, A.; Friend, C. S.; Kapoor, R.; Prasad, P. N. J. Phys. Chem. B 2002, 106, 1909.

23. Viswanathamurthi, P.; Bhattarai, N.; Kim, H. Y.; Lee, D. R.; Kim, S. R.; Morris, M. A. Chem. Phys. Lett. 2003, 374, 79.

24. Murphy, C. J.; San, T. K.; Gole, A. M.; Orendorff, C. J.; Gao, J. X.; Gou, L.; Hunyadi, S. E.; Li, T. J. Phys. Chem. B 2005, 109, 13857.

25. Sun, Y. G.; Yin, Y. D.; Mayers, B. T.; Herricks, T.; Xia, Y. N. Chym. Mater. 2002, 14, 4736.

26. Schroeder, H. Phys. Thin Films 1969, 5, 87.

27. Hu, L. L.; Yoko, T.; Kozuka, H.; Sakka, S. Thin Solid Films 1992, 219, 18.

28. Stathatos, E.; Lianos, P.; Tsakiroglou, C. Langmuir 2004, 20, 9103.

29. Sheng, Y.; Liang, L.; Xu, Y.; Wu, D.; Sun, Y. Opt. Mater. 2008, 30, 1310.

30. Zhao, D. Y.; Feng, J. L.; Huo, Q. S.; Melosh, N.; Fredrickson, G. H.; Chmelka, B. F.; Stucky, G. D. Science 1998, 279, 548.

31. Lu, Y. F.; Ganguli, R.; Drewien, C. A.; Anderson, M. T.; Brinker, C. J.; Gong, Y. X.; Soyez, H.; Dunn, B.; Huang, M. H.; Zink, J. I. Nature 1997, 389, 364.

32. Falcaro, P.; Grosso, D.; Amenitsch, H.; Innocenzi, P. J. Phys. Chem. B 2004, 108, 10942.

33. Zhou, Y.; Schattka, J. H.; Antonietti, M. Nano Lett. 2004, 4, 477.

34. Hrubesh, L. W.; Pekala, R. W. J. Mater. Res. 1994, 9, 731.

35. Leventis, N.; Sotiriou-Leventis, C.; Zhang, G. H.; Rawashdeh, A. -M. M.; Nano Lett. 2002, 2, 957.

36. Vincent, A.; Babu, S.; Brinley, E.; Karakoti, A.; Deshpande, S.; Seal, S. J. Phys. Chem. C 2007, 111, 8291.

37. Thomas, I. M. Appl. Opt. 1992, 31, 6145.

38. Prevo, B. G.; Hwang, Y.; Velev, O. D. Chem. Mater. 2005, 17, 3642.

39. Brinker, C. J.; Ward, T. L.; Sehgal, R.; Raman, N. K.; Hietala, S. L.; Smith, D. M.; Hua, D. W.; Headley, T. J. J. Membrane Sci. 1993, 77, 165.

40. Raman, N. K.; Brinker, C. J. J. Membrane Sci. 1995, 105, 273.

41. Lu, Y.; Cao, G.; Kale, R. P.; Prabakar, S.; López, G. P.; Brinker, C. J. Chem. Mater. 1999, 11, 1223.

42. Wei, Q.; Wang, F.; Nie, Z. -R.; Song, C. -L.; Wang, Y. -L.; Li, Q. -Y. J. Phys. Chem. B 2008, 112, 9354.

43. Kruk, M.; Asefa, T.; Jaroniec, M.; Ozin, G. A. J. Am. Chem. Soc. 2002, 124, 6383.

44. Endo, A.; Miyata, T.; Akiya, T.; Nakaiwa, M.; Inagi, Y.; Nagamine, S. J. Mater. Sci. 2004, 39, 1117.

45. Di, Y.; Meng, X.; Wang, L.; Li, S.; Xiao, F. -S. Langmuir 2006, 22, 3068.

46. Wang, R.; Han, S.; Hou, W.; Sun, L.; Zhao, J.; Wang, Y. J. Phys. Chem. C 2007, 111, 10955.

47. Lee, K. H.; Yim, J. -H.; Baklanov, M. R. Microporous Mesoporous Mater. 2006, 94, 113.

48. Rajagopalan, T.; Lahlouh, B.; Lubguban, J. A.; Biswas, N.; Gangopadhyay, S.; Sun, J.; Huang, D. H.; Simon, S. L.; Mallikarjunan, A.; Kim, H. C.; Volksen, W.; Toney, M. F.; Huang, E.; Rice, P. M.; Delenia, E.; Miller, R. E., Appl. Phys. Lett., 2003, 82, 4328.

49. Ting, C. -Y.; Sheu, H. -S.; Wu, W. -F.; Wan, B. -Z. J. Electrochem. Soc. 2007, 154, G1.

50. Kim, T. -W; Ryoo, R.; Kruk, M.; Gierszal, K. P.; Jaroniec, M.; Kamiya, S.; Terasaki, O. J. Phys. Chem. B 2004, 108, 11480.

51. Sing, K. S. W.; Everett, D. H.; Haul, R. A. W.; Moscou, L.; Pierotti, R. A.; Rouquérol, J.; Siemieniewska, T. Pure Appl. Chem. 1985, 57, 603.

52. Tilgner, I. C.; Fischer, P.; Bohnen, F. M.; Rehage, H.; Maier, W. F. Micropor. Mater. 1995, 5, 77.

53. Lee, D. W.; Yu C. Y.; Lee, K. H. J. Phys. Chem. C 2008, 112, 5136.

54. Brinker, C. J.; Sehgal, R.; Hietala, S. L.; Deshpande, R.; Smith, D. M.; Loy, D.; Ashley, C. S. J. Membr. Sci. 1994, 94, 85.

55. Nair, B. N.; Elferink, W. J.; Keizer, K.; Verweij, H. J. Colloid Interface Sci. 1996, 178, 565.

56. Elferink, J. W.; Nair, B. N.; de Vos, R. M.; Keizer, K.; Verweij, H. J. Colloid Interface Sci. 1996, 180, 127.

57. Nair, B. N.; Elferink, J. W.; Keizer, K.; Verweij, H. J. Sol-Gel Sci. Technol. 1997, 8, 471.

58. Song, Y.; Garcia, R. M.; Dorin, R. M.; Wang, H. R.; Qiu, Y.; Coker, E. N.; Steen, W. A.; Miller, J. E.; Shelnutt, J. A. Nano Lett. 2007, 7, 3650.

59. Sakai, G.; Yoshimura, T.; Isohata, S.; Uota, M.; Kawasaki, H.; Kuwahara, T.; Fujikawa, D.; Kijima, T. Adv. Mater. 2007, 19, 237.

60. Wang, S. Y.; Jiang, S. P.; Wang, X.; Guo, J. Electrochim. Acta 2011, 56, 1563.

61. Strobl, G. R. The Physics of Polymers: Concepts for Understanding Their Structures and Behavior, 3rd ed., Springer, Berlin, 2007.

62. Schaefer, D. W.; Martin, J. E.; Keefer, K. D. In Physics of Finely Divided Matter, eds. Bocarra, N. and Daoud, M.; Springer, Berlin, 1985.

63. Martin, J. E.; Hurd, A. J. J. Appl. Cryt. 1986, 20, 61.

64. Vollet, D. R.; de Sousa, W. A. T.; Donatti, D. A.; Ibañez Ruiz, A. J. Non-Cryst. Solids 2007, 353, 143.

65. D. W. Schaefer, Science 1989, 24, 1023.

66. de Lange, R. S. A.; Hekkink, J. H. A.; Keizer, K.; Burggraaf, A. J. J. Non-Cryst. Solids 1995, 191, 1.

67. Kallala, M.; Sanchez, C.; Cabane, B. J. Non-Cryst. Solids 1992, 147&148, 189.

68. Kamiyama, T.; Mikami, M.; Suzuki, K. J. Non-Cryst. Solids. 1992, 150, 157.

69. Kallala, M.; Sanchez, C.; Cabane, B. Phys. Rev. B 1993, 48, 3692.

70. Pattier, B.; Henderson, M.; Brotons, G.; Gibaud, A. J. Phys. Chem. B 2010, 114, 5227.

71. Yoldas, B. E. Appl. Opt. 1980, 19, 1425.

72. Thomas, I. M. Appl. Opt. 1992, 31, 6145.

73. Ibn-Elhaj, M.; Schadt, M. Nature 2001, 410, 796.

74. Xi, J. -Q.; Kim, J. K.; Schubert, E. F. Nano Lett. 2005, 5, 1385.

75. Cho, J.; Hong, J.; Char, K.; Caruso, F. J. Am. Chem. Soc. 2006, 128, 9935.

76. Konjhodzic, D.; Schroter, S.; Mariow, F. Phys. Stat. Sol. A 2007, 204, 3676.

77. Chhajed, S.; Schubert, M. F.; Kim, J. K.; Schubert, E. F. Appl. Phys. Lett. 2008, 93, 251108.

78. Hoshikawa, Y.; Yabe, H.; Nomura, A.; Yamaki, T.; Shimojima, A.; Okubo, T. Chem. Mater. 2010, 22, 12.

79. Bange, K.; Ottermann, C. R.; Anderson, O.; Jeschkowski, U.; Laube, M.; Feile, R. Thin Solid Films 1991, 197, 279.

80. Orignac, X.; Barbier, D.; Du, X. M.; Almeida, R. M. Appl. Phys. Lett. 1996, 69, 895.

81. Yang, P. D.; Wirnsberger, G.; Huang, H. C.; Cordero, S. R.; McGehee, M. D.; Scott, B.; Deng, T.; Whitesides, G. M.; Chmelka, B. F.; Buratto, S. K.; Stucky, G. D. Science 2000, 287, 465.

82. Lee, L. H.; Chen, W. C. Chem. Mater. 2001, 13, 1137.

83. Bartl, M. H.; Boettcher, S. W.; Hu, E. L.; Stucky, G. D. J. Am. Chem. Soc. 2004, 126, 10826.

84. Karaman, M.; Kooi, S. E.; Gleason, K. K. Chem. Mater. 2008, 20, 2262.

85. Rao, Y. Q.; Chen, S. Macromolecules 2008, 41, 4838.

86. Young, H. D.; Freedman, R. A. University Physics with Modern Physics, 12th Edition. Pearson 2008.

87. Bass, M. Handbook of Optics, 2nd edition, Vol. 2. McGraw-Hill 1994.

88. Bass, M.; DeCusatis, C.; Enoch, J.; Lakshminarayanan, V.; Li, G.; MacDonald, C.; Mahajan, V.; van Stryland, E. Handbook of Optics, 3rd edition, Vol. 4. McGraw-Hill 2009.

89. Hecht, E.; Optics, 4th Edition, Pearson 2003.

90. Sopra N&K database, http://www.sopra-sa.com/index.php. Retrieved January 5, 2012.

91. http://www.filmetrics.com/. Retrieved March 1, 2012.

92. http://www2.dupont.com/Teflon_Industrial/en_US/products/product_by_name/teflon_af/properties.htm l. Retrieved January 5, 2012.

93. http://www.agcce.eu.com/CYTOP/TechInfo.asp. Retrieved January 5, 2012.

94. Kasarova, S. N.; Sultanova, N. G.; Ivanov, C. D.; Nikolov, I. D. Optical Materials 2007, 29, 1481.

95. Speight, J. G.; Lange, N. R. McGraw-Hill. ed. Lange's handbook of chemistry,16th Edition, 2005, pp. 2807.

96. Gorman, B. P.; Orozco-Teran, R. A; Roepsch, .J. A.; Dong, H.; Reidy, R. F. Appl. Phys. Lett. 2001, 79, 4010.

97. Chen, J. Y.; Pan, F. M.; Cho, A.T.; Chao, K. J.; Tsai, T. G.; Wu, B. W.; Yang, C. M.; Chang, L. J. Electrochem. Soc. 2003, 150, F123.

98. Dong, H.; Gorman, B. P.; Zhang, Z.; Orozco-Teran, R. A; Roepsch, .J. A.; Mueller, D. W.; Kim, M. J.; Reidy, R. F. J. Non-Cryst. Solids 2004, 350, 345.

99. Cha, B. J.; Kim, S.; Char, K.; Lee, J. -K.; Yoon, D. Y.; Rhee, H. -W. Chem. Mater. 2006, 18, 378.

100.Luo, J. -T.; Wen, H. -C.; Chang, Y. -M.; Wu, W. -F.; Chou, C. -P. J. Colloid Interface Sci. 2007, 305, 275.

101.Faustini, M.; Nicole, L.; Boissière, C.; Innocenzi, P.; Sanchez, C.; Grosso, D. Chem. Mater. 2010, 22, 4406.

102.Padovani, A. M.; Rhodes, L.; Riester, L.; Lohman, G.; Tsuie, B.; Conner, J.; Allen, S. A. B.; Kohl, P. A. Electrochem. Solid State Lett. 2001, 4, F25.

103.Martinu, L.; Poitras, D. J. Vac. Sci. Technol. A 2000, 18, 2619.

104.Mosaddeq-ur-Rahman, M.; Yu, G.; Soda, T.; Jimbo, T.; Ebisu, H. Umeno, M. J. Appl. Phys. 2000, 88, 4634.

105.Hanley, T. L.; Luca, V.; Pickering, I.; Howe, R. F. J. Phys. Chem. B 2002, 106, 1153.

106.Ozer, N.; Demiryont, H.; Simmons, J. H. Appl. Opt. 1991, 30, 3661.

107.Shimooka, H.; Kuwabara, M. J. Am. Ceram. Soc. 1995, 78, 2849.

108.Lee, S. W.; Ichinose, I.; Kunitake, T. Langmuir 1998, 14, 2857.

109.He, J. H.; Ichinose, I.; Fujikawa, S.; Kunitake, T.; Nakao, A. Chem. Mater. 2002, 14, 3493.

110.Rantala, J. T.; Kärkkäinen, A. H. O. Opt. Express 2003, 11, 1406.

111.Song, X. M.; Wu, J. M.; Tang, M. Z.; Qi, B.; Yan, M. J. Phys. Chem. C 2008, 112, 19484.

112.Wang, R.; Hashimoto, K.; Fujishima, A.; Chikuni, M.; Kojima, E.; Kitamura, A.; Shimohigoshi, M.; Watanabe, T. Nature 1997, 388, 431.

113. Cassie, A. B. D.; Baxter S. Trans. Faraday Soc. 1944, 40, 546.

CHAPTER 2

Microstructures of Silica Liquid Precursors and

Porous Solid Materials

2.1. Introduction

Porous silicon dioxide (silica) has attracted considerable attention for diverse applications owing to its

fundamental characters, such as chemical and thermal stability, optical transparency, and mechanical

strength.[1-3] Since nano-sized pores generally contribute to the enhancement of distinctive properties of silica

materials, porous silica is expected to be utilized for a wide range of functional materials, e.g., low dielectric

materials,[4-6] low refractive materials,[2,7,8] and thermal insulators.[9-11] Various approaches have been suggested as

a pore generation technique.[12-14] However, poor mechanical properties and performance degradation caused by

penetration and adsorption of external organic substances are still inherent problems of these porous materials.[5,]

[15, 16] Recent studies on porous materials have shown that a small pore size and its uniformity contribute to the strength.[5, 17-19] Additionally, small pores appear to prevent the deposition of chemical species in the pores.[20] From these standpoints, microporous silica having micropores (diameter $d < 2$ nm[21]) is highly desired as a candidate for evolutionary materials that can overcome all these difficulties.

When targeting the precise control of the pore size and its uniformity aimed at the silica materials that possess exclusively micropores, the geometry control of the polymer-like, low-fractal dimension structures in the precursor solution with an optimized hydrolysis/condensation reaction represents a challenge. Compared with many existing approaches introducing organic templates to create micropores,[22-28] this approach has some advantages to obtain porous solid materials, e.g., there is no template firing process at high temperature to create pores. It is established that use of a base catalyst in sol–gel process produces highly branched silica polymers, resulting in densely structured particles that easily create a void among them.[29] This often leads to mesopore (2 nm $< d < 50$ nm) or macropore ($d > 50$ nm) formation[21] in the silica solids due to the fact that the void size, i.e., pore diameter, is governed by the particle geometry and size.[29-31] On the other hand, weakly branched silica polymers characterized by a low-fractal dimension have shown to be synthesized using an acid catalyst.[29,32-35] Micropores ($d < 2$ nm) are usually produced via an acid-catalyzed system, while the pore volume is not necessarily large.

Degree of branching in the precursor, which is expressed in a fractal dimension d_f, has been investigated using small angle X-ray scattering (SAXS).[36] Brinker et al. obtained weakly branched silica polymers with d_f ~2 by a two step hydrolysis procedure[29,37] of tetraethyl orthosilicate using a hydrochloric acid catalyst. Microporous structure containing small pores < 1 nm was obtained in the dried material of these silica precursor polymers. Similarly, Nair et al. used a nitric acid catalyst, and suggested that the linear structure of silica precursor polymers should be appropriate for micropores formation.[33]

Small angle X-ray scattering (SAXS) was used to investigate microstructures of the silica sols prepared using the non-ionic hydroxyacetone (HA) catalyst. The structural evolution driven by the sol–gel reaction in the

precursor solutions were pursued by time-resolved SAXS measurements for several days. The structures of the

heat-treated sol and the product silica powders derived from dried sols were also investigated by SAXS and N_2

adsorption-desorption measurements. Effects of hydrocarbon chain length of the monohydric alcohols in the

solvent as well as those of the HA catalyst on the microporous architecture of the silica solid materials have

been elucidated.

2.2. Experimental Section

2.2.1. Sample preparation

Materials. Tetramethyl orthosilicate, (TMOS; $Si(OCH_3)_4$ > 98%) and hydroxyacetone (CH_3COCH_2OH

> 80%) were purchased from Tokyo Chemical Industry, Japan. Methanol (> 99.8%), ethanol (> 99.5 %) and

1-propanol (> 99.5%) were purchased from Wako Pure Chemical Industries, Japan. These reagents were used

as received.

Synthesis. Precursor solutions were synthesized by the catalytic sol-gel process using hydroxyacetone

catalyst. Monohydric alcohols, e.g., methanol, ethanol, or 1-propanol were used as solvent. TMOS, alcohol, and

distilled water were mixed in a tightly closed bottle. A non-ionic catalyst, hydroxyacetone, was added to each

solution. A solution without the catalyst was also prepared using methanol as a control. A thoroughly mixed

solution was stirred continuously and constantly at 25 °C for several days. The molar ratio of $Si(OCH_3)_4$ to H_2O

was 1 to 5, and hydroxyacetone was added at an equal molar ratio to TMOS except the catalyst–free solution,

resulting in the concentration of TMOS of 0.525 mol L^{-1}.

Porous silica powders were fabricated from the aged precursor solutions. The solutions, which were stirred

at 25 °C for a day, were placed in a thermostatic chamber at 40 °C, and then kept a still standing for three days.

The aged solutions were evaporated and dried under vacuum to produce whitish powders. The dried silica

powders were immersed in water at 80 °C for 2 hours to hydrolyze methoxy groups and to remove organic

compounds, and then dried at 40°C for 6 hours.

2.2.2. Characterization

Small-angle x-ray scattering (SAXS). SAXS measurements were carried out on precursor solutions, product powders, and their model systems. A SAXSess camera (Anton Paar, Austria) attached to a sealed tube anode X-ray generator (GE Inspection Technologies, Germany) was operated at 40 kV and 50 mA. A Göbel mirror and a block collimator provide a focused monochromatic X-ray beam of Cu Kα radiation (λ = 0.1542 nm) with a well-defined shape. A thermostated sample holder unit (TCS 120, Anton Paar) was used to control the sample temperature at 20 °C. The two-dimensional (2D) scattering patterns recorded by an imaging-plate (IP) detector (a Cyclone, Perkin-Elmer) were integrated into to one-dimensional (1D) scattered intensities, $I(q)$, as a function of the magnitude of the scattering vector $q = (4\pi/\lambda)\sin(\theta/2)$ using SAXSQuant software (Anton Paar), where θ is the total scattering angle. All the measured intensities were semi-automatically calibrated for transmission by normalizing a zero-q attenuated primary intensity to unity. All $I(q)$ data were corrected for the background scattering from the capillary and the solvents, and the absolute scale calibration was made using water as a secondary standard.[38] A model-independent collimation correction procedure was made via an indirect Fourier transformation (IFT)[39,40] routine and/or based on a Lake algorithm. All the fitting and fractal analyses were made after the desmearing procedure.

^{29}Si NMR. Chemical characterization of silica precursors was conducted by ^{29}Si NMR spectroscopy. All ^{29}Si spectra were obtained on an ADVANCE 400 MHz FT-NMR spectrometer (Bruker) at 20 °C as a function of the reaction times at 0 – 48 hours. All the measurements were conducted with a pulse width of 18 μs and a pulse delay of 10 s at 79.49 MHz. 2 mL of the precursor solution was put in a 10 mm NMR glass tube, and chromium(III) acetylacetonate used as a relaxation agent was well dissolved before individual measurements. All ^{29}Si chemical sifts were externally referenced to the silicon peak of hexamethyldisiloxane (δ = 6.68 ppm) in a 5 mm inner tube. Spectrum peaks manifest various silicon sites in distinct chemical environments. The notation Q_i^j is commonly used to explain the degree of hydrolysis and condensation for a four functional unit (e.g., tetramethyl orthosilicate), where the subscript i and superscript j denote the number of silanols and

siloxane bonds on the silicon atom, respectively. Accordingly, the number of alkoxy groups on the silicon is

4−i−j.

Nitrogen adsorption porosimetry. Nitrogen gas adsorption−desorption isotherm were performed at -196 °C

on an ASAP2010 volumetric adsorption analyzer (Micromeritics), after the heated powders were outgassed

under vacuum at 200 °C in the degassing port. Specific pore volume and surface area of the micropores were

evaluated from the adsorption isotherm data using the t-plot method[28,41] in the thickness range of 0.35 − 0.5 nm,

an empirical method based on the comparison of the obtained nitrogen adsorption isotherm for a porous sample

with that of a non-porous reference material. A plot of the adsorption volume versus the statistical thickness of

adsorbed layer on a reference surface was used in the t-plot method. Specific surface area was also calculated

from the data in the relative pressure range from 0.05 to 0.3 using Brunauer−Emmett−Teller (BET) method,[42]

and total pore volumes were determined from the volume of the adsorbed nitrogen gas at a relative pressure of

0.95.[21] The pore size distributions in the pore diameter in the range of 2 − 10 nm were evaluated by the

Barrett−Joyner−Halenda (BJH) method,[43] whereas those of < 2 nm were measured by the Saito−Foley (SF)

modified Horváth−Kawazoe (HK) model from the adsorption isotherms in the low relative pressure region.[44,45]

Transmission electron microscope (TEM) observation. TEM images of the powder samples were obtained

using a JEM-2010 transmission electron microscope (JEOL) with an acceleration voltage of 200 kV. Fine

ground powders were dispersed in methanol by ultrasonication. One drop of the suspensions was put on a 150

mesh carbon-coated copper grid, and then they were dried at 60 °C in air.

Table 2.1. Summary of the Preparation Process for Each of the Silica Precursor Sols and Powders [a]

Sample code	Solvent	Catalyst	Chemical Hydrolysis	State
LCSm	Methanol	Yes	—	Liquid
LCSe	Ethanol	Yes	—	Liquid
LCSp	1-Propanol	Yes	—	Liquid
LSm	Methanol	No	—	Liquid
CSm[b]	Methanol	Yes	No	Powder
CSe[c]	Ethanol	Yes	No	Powder
HCSm	1-Propanol	Yes	Yes	Powder[d]
HCSe	Methanol	Yes	Yes	Powder[d]
HCSp	Methanol	Yes	Yes	Powder[d]
HSm	Methanol	No	Yes	Powder[d]

[a] The powder samples were prepared by drying the liquid samples. Before the chemical hydrolysis of [b] HCSm or [c] HCSe. [d] The powders were hydrolyzed by immersing them in water at 80 °C and then dried at 40 °C.

2.3. Results and discussion

2.3.1. Structure characterization of the precursor solutions as obtained by SAXS

It is postulated that the porous structure of the sol–gel derived solid materials reflects the conformation of the aggregates in the liquid precursors.[29,33,37] The time evolution of static structures in the silica precursor solutions has been evaluated by means of SAXS.[46] Figure 2.1 shows SAXS experiments on the silica precursor solutions prepared using different monohydric alcohols with and without the HA catalyst, in which collimation–corrected SAXS intensities, $I(q)$, for LCSm, LCSe, LCSp, and LSm are given in a double-logarithmic plot as a function of the reaction time, t.

The pronounced increase of $I(q)$ with time for all the systems with reaction time provides evidence for the growth of the silica aggregates in the precursor solutions. Figure 2.2 shows the extrapolated forward intensities to zero scattering vector, $I(q{\rightarrow}0)$, of all the precursor solutions together with the radius of gyration, R_g, of LCSm and LCSe (R_g of LCSp and LSm are not accessible because Guinier regime $qR_g < 1$ for these samples was beyond the resolution of this SAXS experiments). Importantly, it is found that independent of hydrocarbon chain lengths of the solvent alcohols and of the presence or absence of the HA catalyst, all the precursor solutions showed induction times for an increase of $I(q{\rightarrow}0)$. The SAXS intensity should remain nearly constant until the size of silica aggregates and their number density are large enough to scatter X-rays to be detected, so that the observed induction times are likely to involve the induction time for nucleation, the actual nucleation period, and the period for the aggregate growth up to a certain size that can clearly be detected by SAXS experiments.

The onset of the intensity rise for the methanol– and ethanol–based systems with the HA catalysts, i.e., LCSm and LCSe, was found to be ca. 36 h. The polymerization in these systems proceeded slowly at $t > 36$ h, yielding the relatively small molecular weights even after 3 days. In contrast, when 1-propanol was substituted for methanol or ethanol (LCSp), the earlier onset was observed (ca. 24 h). The aggregates exhibited far faster growth than those observed in LCSm and LCSe in $t > 24$ h, and finally reached several tens of times greater relative intensities than those for LCSm and LCSe. The absence of the HA catalyst (LSm) also led to faster growth and high molecular weights of the aggregates, similar to the behavior of the 1-propanol–based LCSp. It suggests that for the induction periods, hydrolyzed species may have been created by the hydrolysis reaction of TMOS that serves as a polymerization nucleus of the following condensation reaction, but polycondensation did not proceed actively.
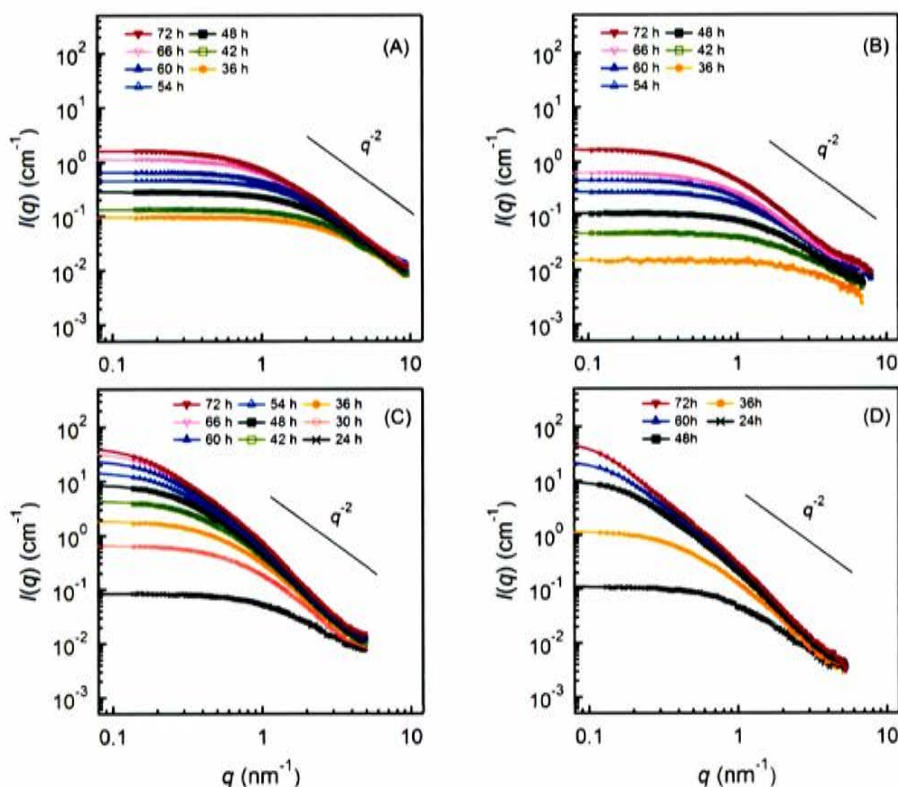
Figure 2.1. Variations of collimation–corrected SAXS intensities, $I(q)$, for the liquid silica precursor solutions, LCSm (A), LCSe (B), LCSp (C), and LSm (D) on absolute scale as a function of the reaction time, t, in a double-logarithmic plot. The solid lines given in all panels represent the q^{-2} slope to highlight a feature of $I(q)$ in the high-q regime.

2.3.2. Scattering functions of the methanol- and ethanol-based precursor solutions

For further quantitative description of the silica aggregate structure in the precursor solutions, the shape of the scattering curves was scrutinized. It was found that when methanol or ethanol was used with the HA catalyst in the precursor solutions, namely for LCSm and LCSe, $I(q)$ can formally be fitted by the Ornstein-Zernike (OZ) equation[47]

$$I(q) = \frac{I(0)}{1 + \xi^2 q^2} \qquad (1)$$

where ξ is the correlation length and $I(0)$ the asymptotic zero-q intensity. In Fig. 2.3, SAXS

intensities, $I(q)$, and Kratky plots, $q^2I(q)$ versus q, of LCSm and LCSe are displayed. Note that the shape of the

OZ function is not the same as, but resembles that of the Debye structure function, $P_{ideal}(q)$, of an ideal or

Gaussian polymer chain in solution[48-50]

$$I(q) = I(0)P_{ideal}(u) = 2I(0)\frac{\exp(-u) + u - 1}{u^2} \qquad (2)$$

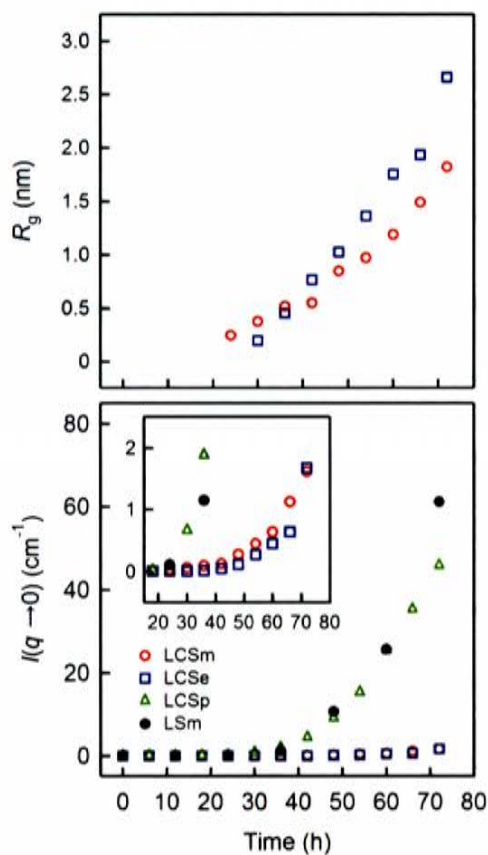where $u = R_g^2 q^2$ with R_g being the radius of gyration.

Figure 2.2. The extrapolated forward intensities to zero scattering vector, $I(q\rightarrow0)$, of LCSm (red), LCSe (blue), LCSp (green), and LSm (black) plotted against the reaction time. The radius of gyration, R_g, for LCSm and LCSe determined with Guinier plot are also plotted in the upper panel. The inset shows an enlarged view of the low intensity regime for LCSm, LCSe, and LCSp, where $I(q\rightarrow0) < 2$ cm^{-1}.

At low–q, $I(q)$ exhibited Guinier behavior reflecting the overall geometry of the aggregates, as described

by a Guinier equation

$$I(q) = I(0)\exp\left[-\frac{R_g^2 q^2}{3}\right] \qquad (3)$$

In the intermediate to high–q regime, power-law behavior was observed, indicating the emergence of the fractal

structures. Self-similarity is an important basic property of fractal objects like polymer chains in solution, which

means that independent of the chosen length scale, a polymer chain exhibits the identical internal structure.[51]

The number of monomers, $n(r)$, contained in a sphere of radius r is represented by the following power law

with an exponent ν

$$n(r) \propto r^\nu \qquad (4)$$

The fractal dimension, d_f, is just defined as the abovementioned exponent ν, where $\nu = 2$ corresponds to an

ideal coil polymer without excluded volume, while $\nu = 5/3$ to an expanded chain with excluded volume in good

solvent. d_f directly shows up in the asymptotic exponent in $I(q)$ as

$$I(q) \propto q^{-d_f} \qquad (5)$$

The q^{-2} slope in $I(q)$ observed for LCSm and LCSe at $q > 2$ nm^{-1} gives $d_f \sim 2$, which is identical with d_f of

an ideal polymer chain. A Kratky plot, $q^2 I(q)$ versus q, is an instructive way to highlight a fractal nature with d_f

~ 2, which is manifested in the high–q plateau ($q^2 I(q) \propto q^0$). The finding demonstrates that low–fractal

dimension, polymer–like aggregates were synthesized by using the HA catalyst with short-chain alcohols,

methanol and ethanol. The local stiffness of a polymer chain often leads to rod-like properties on a short length

scale, which is revealed in the highest-q regime of SAXS curve. The position of cross-over, q^*, from coil-like

[$I(q) \propto q^{-2}$] to rod-like scattering [$I(q) \propto q^{-1}$], can clearly and only vaguely be seen for LCSe and LCSm,

respectively, which corresponds to persistence length, l_{ps}. $\sim \pi/q^*$; see Figs. 2.3(D) and 2.3(C).

The correlation length, ξ, explicitly involved in the OZ expression (Eq.(1)) can be interpreted as the

mesh–size of the transient polymer network,[50] representing the length scale of the spatial correlation of density

fluctuations caused by a polymer chain.[51] Figure 2.4 shows variation of ξ in the methanol–based and ethanol–based precursor solutions with the HA catalyst as a function of the reaction time as obtained by SAXS. It was observed that ξ was an increasing function of time, LCSm showing greater values than LCSe. Importantly, even after 3 days, the growth of ξ was rather limited; LCSm gave $\xi \sim 1.3$ nm at $t = 72$ h, while LCSe did $\xi \sim 1.9$ nm. As discussed in the following sections, such geometry found in the liquid precursors is closely linked with the pore size of the resulting solid silica materials produced from LCSm and LCSe.
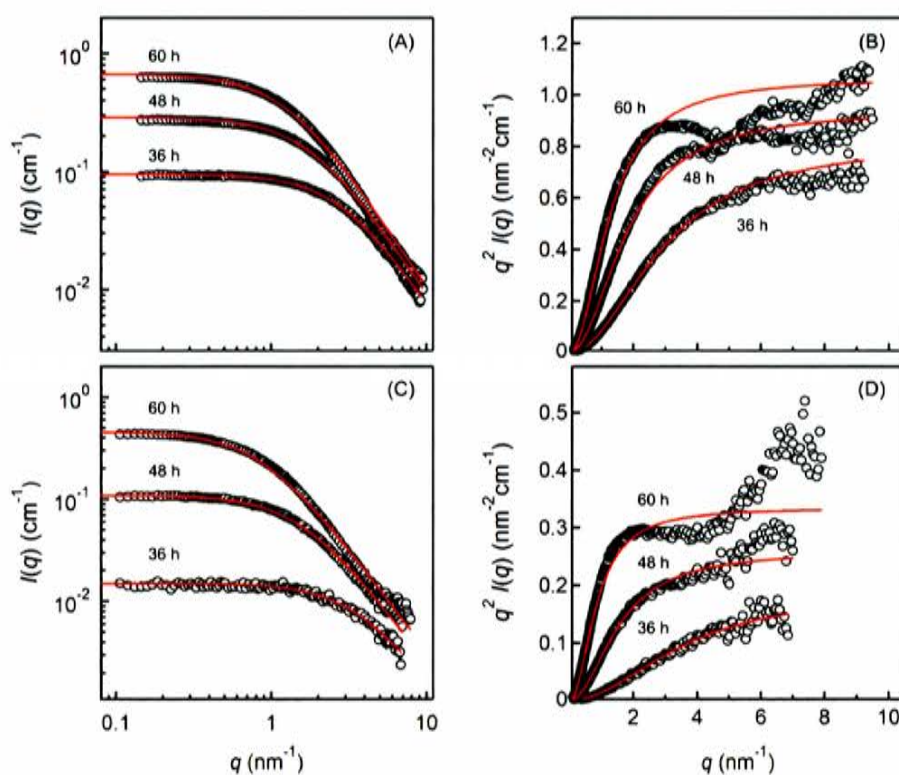

Figure 2.3. Collimation–corrected SAXS intensities, $I(q)$, and Kratky plots, $q^2 I(q)$ versus q, of the methanol– and ethanol–based precursor solutions with the HA catalyst, forming low–fractal dimension polymer–like aggregates with $d_f \sim 2$; LCSm (A, B) and LCSe (C, D), as a function of the reaction time at 36, 48, and 60 hours. Red solid lines represent the optimum fit curves based on Ornstein–Zernike (OZ) equation.
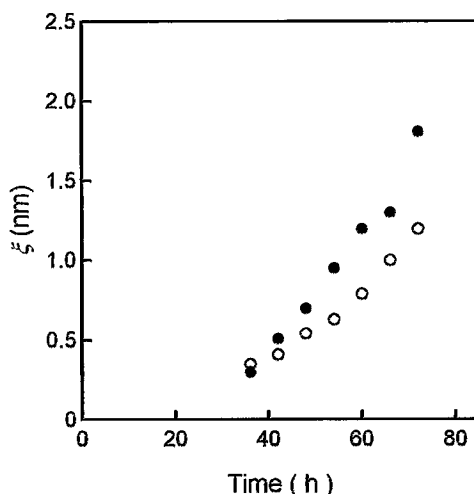
Figure 2.4. Variation of the correlation length (mesh–size), ξ, of LCSm (open circle) and LCSe (filled circle) with the reaction time.

Generally, the asymptotic zero–q intensity, $I(q\rightarrow 0)$, gives a measure of molecular weight of a polymer chain in a dilute solution. This relation is no longer exact for a semidilute solution because osmotic compressibility also contributes to $I(q\rightarrow 0)$.[49-51] Nevertheless, the apparent (relative) molecular weight, M_w^{app}, of the polymer-like aggregates in the precursor solutions may be semi-quantitatively evaluated, relying on the relative forward intensity, $I(q\rightarrow 0, t)/I(q\rightarrow 0, 0)$. Figure 2.5 shows $I(q\rightarrow 0, t)/I(q\rightarrow 0, 0)$ plotted against R_g evaluated based on Eq.(3) using a Guinier plot [ln$I(q)$ vs q^2]. With increasing R_g, $I(q\rightarrow 0, t)/I(q\rightarrow 0, 0)$ increased, showing downwards convex behavior, in which interplay of mass and the extent of spatial distribution of a polymer–like aggregate is manifested; solid lines are the optimum fit curves under the assumption of $M_w^{app} \propto R_g^v$. These exponents were evaluated as $v = 1.98$ and 2.17 for LCSm and LCSe, respectively. The exponent of ca. 2 again confirms the growth of the weakly–branched coil polymer–like aggregates.

All the data presented in Figs. 2.3–2.5 unambiguously demonstrate that Gaussian polymer-like aggregates having microscopic correlation length (or mesh–size) < 2 nm and low fractal dimensions ~ 2, can selectively be synthesized in the precursor solutions based on a short chain alcohol (methanol or ethanol) and the HA catalysts.
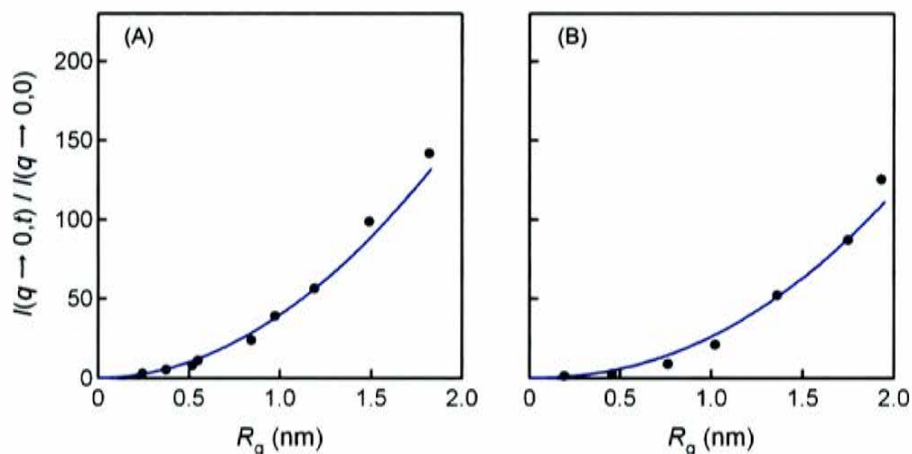
Figure 2.5. The relative forward intensity, $I(q \rightarrow 0, t)/I(q \rightarrow 0, 0)$, versus the radius of gyration, R_g, for LCSm (A) and LCSe (B). $I(q \rightarrow 0, t)/I(q \rightarrow 0, 0)$ may be used as a measure of the weight–averaged apparent molecular weight, M_w^{app}, of the polymer–like aggregates. Solid lines are the optimum fit curves drawn under the assumption of $M_w^{app} \propto R_g^{\nu}$, yielding $\nu = 1.98$ and 2.17 for LCSm and LCSe, respectively.

2.3.3. Scattering behavior of the 1-propanol and without catalyst solutions

The precursor solutions based on 1-propanol (LCSp) and without the HA catalyst (LSm) were also investigated. As discussed later, these precursor solutions resulted in the mesopore formation. Figure 2.6 shows SAXS intensities, $I(q)$, and Kratky plots, $q^2 I(q)$ versus q, of LCSp and LSm. Figure 2.6 indicates that in contrast to the observation that the weakly branched polymer-like aggregates in LCSm and LCSe exhibited very similar behavior to an ideal polymer chains, substitution of 1-propanol or the absence of the HA catalyst led to considerably different scattering behavior. $I(q)$ for LCSp and LSm cannot be described by the OZ function, representing a local maximum in the Kratky plot. It is naturally understood that branching of polymer chains imposes a somewhat particle-like nature to the polymer chains. Toporowski and Roovers predicted that star-branched polymers give such a local maximum in a Kratky plot.[52] Similar phenomenon was observed for dendrimers[53] and nanoparticles comprising tightly crosslinked liner chain precursors[54]. If a Kratky plot is applied to hardsphere, it gives a low-q local maximum and the rapid decrease at high-q as $q^2 I(q) \propto q^{-2}$. However, unlike the expected behavior for a colloidal particle having homogeneous density, a high-q plateau after a local maximum is still present for LSCp and LSm. It suggests that such notable features of in LCSp and LSm are due

to the co-existing particle-like and Gaussian chain-like natures of the branched polymer-like aggregates in these systems.

The shape of the scattering function for a polymer is governed by the structure function, $S_{poly}(q)$, which is given by Fourier transformation of the monomer-monomer pair-correlation function, $g(r)$

$$I(q) \propto S_{poly}(q) = 4\pi \langle c_m \rangle \int_0^\infty [g(r) - 1] r^2 \frac{\sin qr}{qr} dr \qquad (6)$$

where $\langle c_m \rangle$ is averaged monomer concentration. For a dilute solution, $g(r)$ describes the correlations within a single chain, whereas for a semidilute solution, $g(r)$ inevitably involves those between different chains. Using Indirect Fourier transformation (IFT) technique,[39,40] $g(r)$ was derived. Figure 2.7 shows the monomer-monomer pair correlation functions of the silica precursors, LCSm, LCSe, LCSp, and LSm, in the expression of $D(r) = \langle c_m \rangle [g(r) - 1] r^2$. This expression provides intuitive information about the extent of spatial distribution of the polymer-like silica aggregates. As shown in the insets of Fig. 2.7, $D(r)$ of LSCm (TMOS/methanol/water/HA) and LCSe (TMOS/ethanoal/water/HA) are well explained by that of an ideal polymer. However, obviously, $D(r)$ of LSCp (TMOS/1-porpanol/water/HA) and LSm (TMOS/water/methanol) cannot be described by $D(r)$ of an ideal liner polymer.

According to the definitions and formulations, $D(r)$ for the branched polymer-like aggregates, as detected in LSCp and LSm, may be understood as a counterpart of the pair-distance distribution function, $p(r)$, of a colloidal dispersion, which is given by the convolution square of the electron density fluctuations, $\Delta \rho(r)$,

$$p(r) \equiv \Delta \tilde{\rho}^2(r) r^2 = \left\langle \int_{-\infty}^\infty \Delta \rho(r_1) \Delta \rho(r_1 - r) dr_1 \right\rangle r^2 \qquad (7)$$

For a dilute colloidal dispersion, the intensity $I(q)$ is given by

$$I(q) \sim P(q) = 4\pi \int_0^\infty p(r) \frac{\sin qr}{qr} dr \qquad (8)$$

where $P(q)$ is form factor of a colloidal particle.[55,56] Indeed, $D(r)$ of LSCp and LSm looks more like $p(r)$ of to some extent elongated colloidal dispersions, which underlines the different structural aspects of LSCp and LSm from those of LSCm and LCSe.
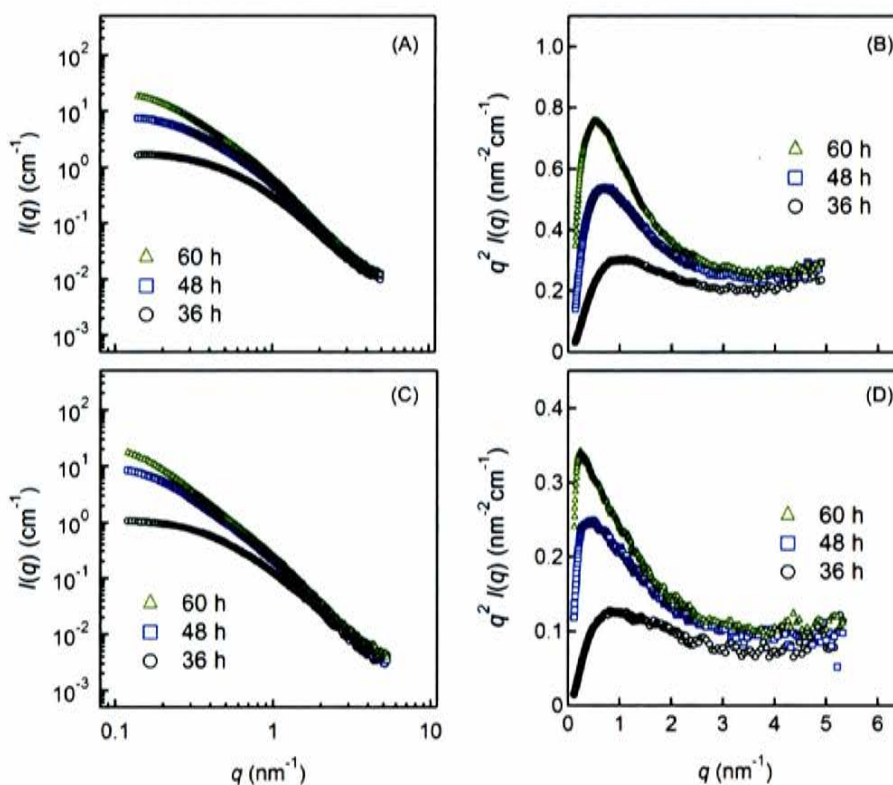
Figure 2.6. Typical SAXS intensities, $I(q)$, and Kratky plots, $q^2I(q)$ versus q, of the 1-propanol–based precursor solutions with the HA catalyst, LCSp (A, B), and the methanol–based precursor solutions without the HA catalyst, LSm (C, D), forming branched polymer–like or particle–like aggregates as a function of the reaction time at 36, 48, and 60 hours.
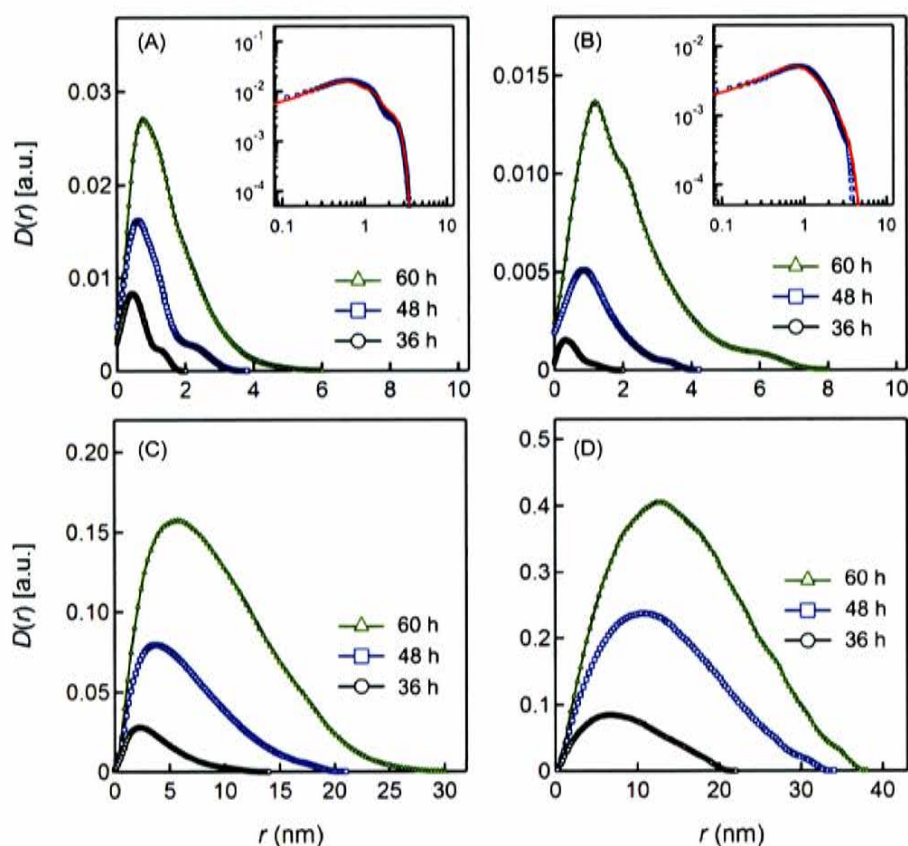
Figure 2.7. The monomer-monomer pair correlation functions in the expression of $D(r) = \langle c_m \rangle [g(r) - 1] r^2$ for

LCSm (A), LCSe (B), LCSp (C), and LSm (D) after 36, 48, and 60 hours. In the insets of (A) and (B), shown is

the comparison of the experimentally obtained $D(r)$ with that for the OZ function, $D(r) = \langle c_m \rangle [\exp(-r/\xi)/r] r^2$.

2.3.4.   Fractal structure of the solid silica powders

The microstructure of the liquid silica precursors should be a key factor that affects the structure of the

dried silica powder products. How the liquid precursor structures is 'imprinted' on the solid silica materials is of

an especial interest. Figure 2.8 shows SAXS intensities, $I(q)$, and Kratky plots, $q^2 I(q)$, of the silica powders

derived from the LCSm and LCSe precursor solutions, together with those of heat–treated sols. Different from

the typical scattering pattern of the liquid precursors, the powder samples exhibited multi–asymptotic behavior

of $I(q)$, which is probably caused by polymer–polymer agglomeration via the heat treatment and drying process.

Importantly, the SAXS data revealed that a series of the methanol–based treated samples, e.g., the heat–treated

LCSm sol, the silica powder produced by drying the heat–treated sol at 40 °C (CSm), the hydrolyzed silica powder (HCSm), and the heat–treated HCSm powder at 200 °C, commonly exhibited the plateau in their Kratky plot in $q > \sim 2$ nm^{-1}. This means the constant monomer density was achieved on a small length scale corresponding to $q > \sim 2$ nm^{-1}, while large length–scale structures were modified via the heat and hydrolysis treatments. The finding is highly indicative of the preserved fractal nature in the internal (local) structures of the hydrolyzed and heat–treated silica powders, i.e., $d_f = \sim 2$ and $\xi < 2$ nm, found in the liquid precursor.

As for the silica powders fabricated from LCSe, the q–position, where $q^2 I(q)$ reaches a plateau shifted to higher–q side with a series of the treatments, which appears to suggest an increasing mesh–size. The HCSe and the heat–treated HCSe powder sample showed a negative slope in their Kratky plots ($d_f > 2$), indicating that additional crosslinking reactions via the hydrolysis and heat treatments caused the emergence of higher fractal–dimension structures. With respect to this observation, it is said that the porous structures derived from LCSe with larger geometry than those from LCSm are relatively fragile against the chemical reactions.
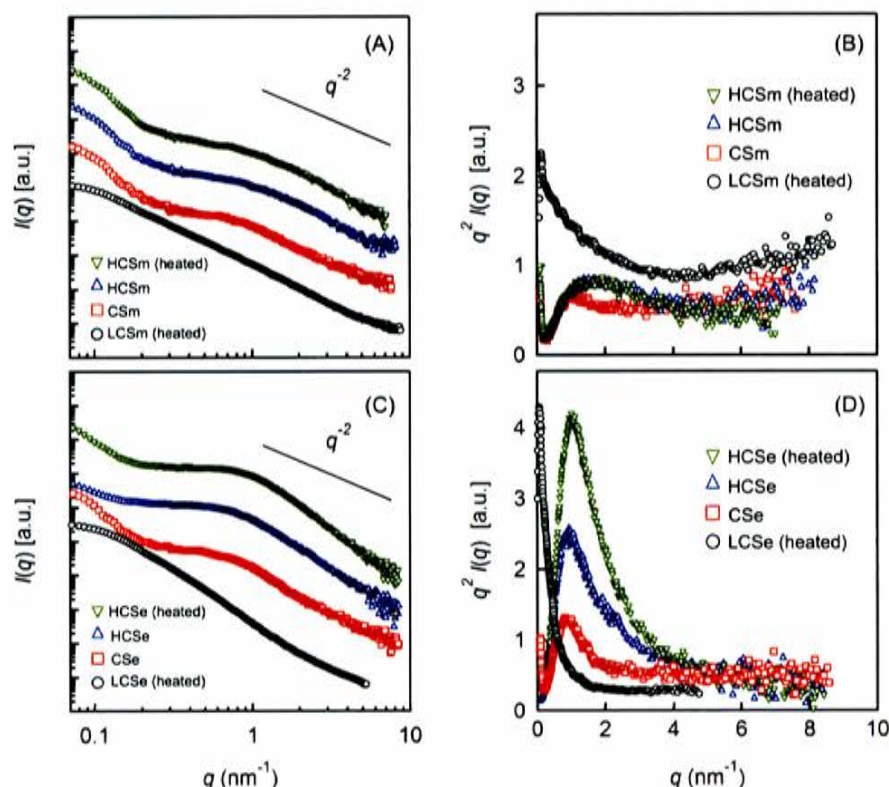
Figure 2.8. SAXS intensities, $I(q)$, and a kratky plot, $q^2 I(q)$, of the heat-treated sol and the silica powder samples synthesized from the methanol–based (A, B) and the ethanol–based (C, D) precursor solutions. $I(q)$ and $q^2 I(q)$ for heat–treated sol from LCSm (black), CSm (red), HCSm (blue), and HCSm heated at 200 °C (green) are shown in the panels (A) and (B), respectively, and those for heat–treated sol from LCSe (black), CSe (red), HCSe (blue), and HCSe after the same heat treatment (green) in the panels (C) and (D).

2.3.5. ^{29}Si NMR investigation of weakly branched silica polymers

The degree of hydrolysis of a silicon alkoxide monomer is considered as one of the influencing factors for the generation of weakly–branched Gaussian chain–like polymers. In order to confirm the state variations of Si sites by the hydrolysis and condensation reactions, ^{29}Si NMR experiment was conducted on the methanol–based precursor solutions with the HA catalysts (LCSm) in an early stage of the sol–gel process (Fig. 2.9). ^{29}Si NMR spectra were recorded at $1 \leq t/h \leq 48$, where t is the reaction time. A Q_0^1 peak intensity at -75.6 ppm increased with the reaction time in $t < 9$ h, while a Q_0^0 peak intensity at -77.9 ppm decreased. Q_0^2 and Q_0^3 peaks appeared respectively at -74.0 and -72.8 ppm at $t \sim 6$ h. The Q_0^2 peak exhibited the maximum area at $t \sim 12$ h, which was smaller than that of Q_0^3. The maximum area of the Q_0^3 peak was attained at $t \sim 15$ h. The Q_0^3

peak is the larger than any other Q_0 peak after the 24-hour reaction. No Q_0^4 peak was observed, which was expected to appear at about -73.1 ppm.[29,57]

The total intensity of the Q_0^0, Q_0^1, Q_0^2, and Q_0^3 peaks was reduced with reaction time. This implies an increase in the number of condensed sites (e.g., Q_1) produced by the condensation reaction of hydrolyzed silicon monomers, while the peaks attributed to Q_1 sites were hidden in a background because of their blurred signals. The consumption of Si monomers was almost completed in $t < 48$ h, in which the condensation reaction between partially hydrolyzed silicon sites proceeded. The data demonstrate that although a sufficient amount of water was added to the solution ([TMOS]:[H$_2$O]=5), a fully hydrolyzed site Q_0^4 was not generated. This notable feature well supports the SAXS results; the condensation of partially hydrolyzed silicon sites efficiently suppressed the branch formation, leading to the weakly branched polymer–like structure. In contrast, an ionic catalyst, e.g., hydrochloride[57-59], generally leads a rapid hydrolysis reaction, producing completely hydrolyzed silicon site Q_0^4.[29] Such fully hydrolyzed silicon atoms often enhance the branch formation, yielding particle–like highly–branched aggregates.[29]
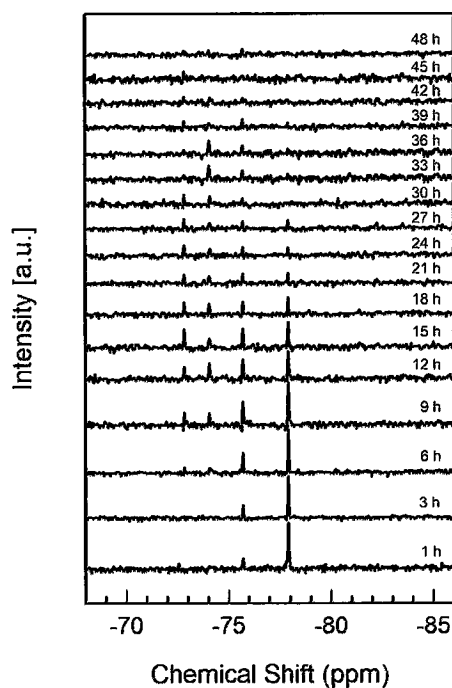
Figure 2.9. Time evolution of the hydrolysis reaction in the methanol–based precursor solution under the presence of the HA catalyst as obtained by ^{29}Si NMR spectroscopy. A time series (from bottom to top) of the ^{29}Si NMR spectra for LCSm as a function of the reaction time, t.

2.3.6. Pore characteristic of produced silica powders

In order to determine the pore characters of the silica powder samples, the N_2 adsorption–desorption measurements was conducted on CSm, HCSm, CSe, and HCSe. The hydrolyzed powders, HCSp and HSm, derived from the LCSp and LSm precursor solutions, respectively, were also evaluated. A N_2 adsorption-desorption isotherm obtained for HCSm, CSm, and CSe showed a typical type I isotherm (Fig. 2.10). According to IUPAC, this is classified into monolayer adsorption of N_2,[21] which represents a porous material based on micropores in diameter < 2 nm. The N_2 adsorption–desorption isotherm of HCSe showed a type I isotherm with minor hysteresis loops, whereas those of HCSp and HSm showed typically type IV isotherms. The miner hysteresis loop of HCSe indicates the presence of pores having slightly larger pore diameter than that of the micropore. The hysteresis loop of HCSp fell into a H2 type associated with an ink bottle shape of pores.[21]

In contrast, HSm, derived from the methanol–based precursor solution without HA catalyst (LSm) showed a

H1 type hysteresis loop, which implies an aggregate as an assembly of particles. The result is consistent with

the SAXS data which have shown the formation of branched polymer–like or somewhat particle–like silica

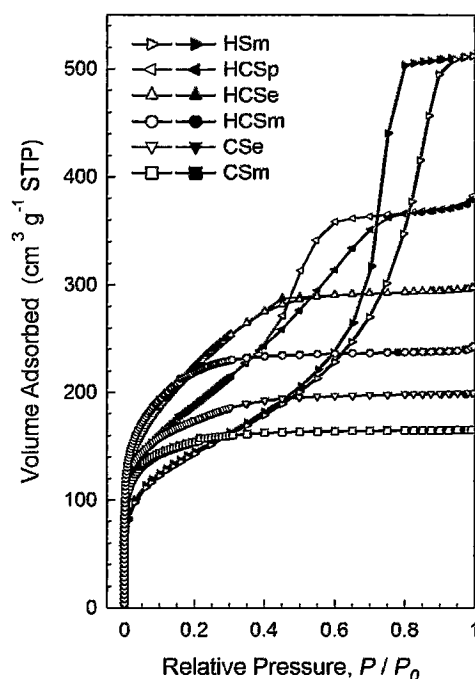aggregates in the LCSp and LSm precursor solutions.

Figure 2.10. Nitrogen adsorption–desorption isotherms of the hydrolyzed silica powders prepared from the HA catalyst–involved precursor solutions with different monohydric alcohols; HCSm (black circle), HCSe (blue circle), and HCSp (green circle), and that from the methanol–based precursor without the HA catalyst; HSm (black triangle). The data for the powders without the hydrolysis treatment, CSm (black square) and CSe (blue square), are also compared in the plot. All samples were heat-treated at 200 °C for 6 h to degas. The adsorption and desorption isotherms are represented by open and filled symbols, respectively.

Figure 2.11 shows the BJH pore size distributions for a series of hydrolyzed silica powders calculated from

the N_2 adsorption data. CSm and HCSm exhibited no obvious peak in the range from 2 to 10 nm. The

distributions marked in the vicinity of $d \sim 2$ nm appear to reflect the amount of micropores. The total pore

volumes of CSm and HCSm were estimated to be 0.26 and 0.37 cm^3 g^{-1}, respectively (Table 2.2). One plausible

reason for this phenomenon is that chemical substances remaining in the solid matrix were eliminated by the

chemical hydrolysis. A broad shoulder can be seen in the pore size distribution of CSe in the range of $2 \le d$/nm

$\le$ 4. After the hydrolysis (HCSe), a small peak at 3.3 nm emerged in the broad distribution. The total pore

volume of 0.31 and 0.46 cm^3 g^{-1} were obtained for CSe and HCSe, respectively (Table 2.2). In the

ethanol–based powders, aside from the targeted elimination of the remains of chemicals, the hydrolysis caused

an increase of large–sized pores ($d \sim$3.3 nm). On the one hand, The pore size distributions of HCSp and HSm,

which were produced from the branched polymer–like or particle–like silica aggregates, showed distinct peaks

at 3.9 and 7.1 nm, respectively, highly indicative of the mesopore formation.

The t-plot analysis, commonly used to determine the micropore volume of microporous materials, was

applied to CSm, HCSm, CSe, and HCSe to confirm the presence of micropores. The t-plots of CSm and HCSm

are given in Fig. 2.12(A). Extrapolation lines for CSm and HCSm determined in the thickness range between

0.35 nm and 0.5 nm had a positive intercept on the y-axis, indicating the presence of micropores. In addition,

the values of their y-intercept were close to each other. This means that the micropore structure was preserved

after the chemical hydrolysis, owing to the robust micropore architecture. In view of the SAXS results shown in

Figs. 2.8(A) and 2.8(B), these powders are characterized by $d_f \sim$2 in their local structures. All these observation

led to conclude that the weakly-branched polymer-like structure in the liquid precursor offers a micropore

framework of the resulting solid silica, whose pore size is regulated by the mesh–size (ξ) of the transient

polymer network produced in the precursor solutions. These samples did not generate secondary pores, which

are usually formed in the aggregate of grown polymers during the drying process.[29] It suggests that mutual

interpenetration of the weakly–branched silica aggregates generated in the liquid precursor, known as an

important nature of Gaussian polymer chains, efficiently avoided the secondary pore creation via the drying
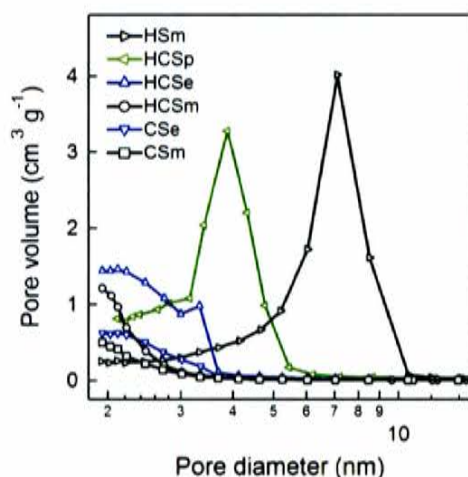
process.

Figure 2.11. BJH pore size distributions of the hydrolyzed silica powders, HCSm, HCSe, HCSp and HSm. For comparison, the data for the powders without the hydrolysis treatment, CSm and CSe, are also displayed.
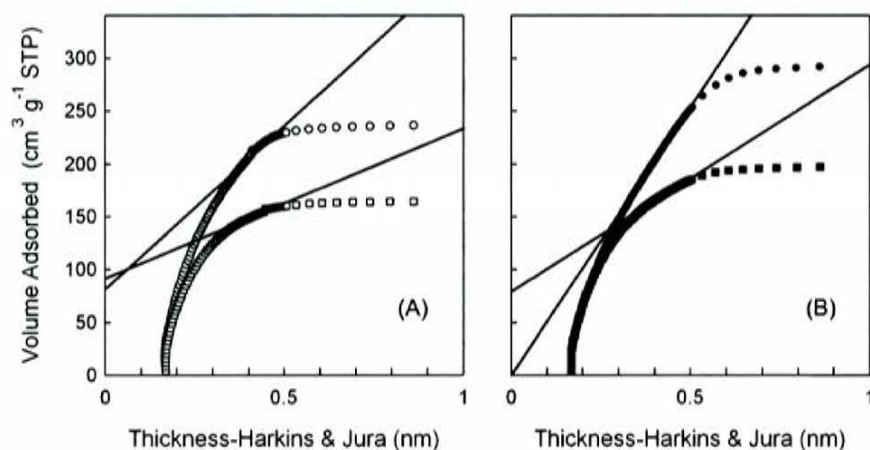

Figure 2.12. Effects of chemical hydrolysis on the micropore volume of the solid silica materials. t-plot curves of the silica powder samples; (A) the methanol–based systems, HCSm (open circle) and CSm (open square), and (B) the ethanol–based systems, HCSe (filled circle) and CSe (filled square). Tangent lines were drawn in the thickness range between 0.35 nm and 0.5 nm.

To scrutinize the pore size distribution in the micropore region of $d < 2$, the SF modified HK modell[45] was applied to CSm and HCSm. This approach is based on a semiempirical calculation of the pore size distribution from the nitrogen adsorption isotherm in microporous materials with slit-like pores, and is applicable to active

carbon. Its application was extended to the cylindrical pore geometry of microporous materials, such as zeolite

and silica,[46] and have been used in many studies on microporous silica[60,61]

It was found that CSm and HCSm exhibited narrow peaks at 0.87 nm and 0.84 nm, respectively (Fig. 2.12). After the hydrolysis treatment, the micropore diameters only slightly decreased. The residual methoxy groups in the polymeric precursors may have been hydrolyzed and converted to silanol groups. The porous silica powders derived from the ethanol system, CSe, had a certainly larger average pore diameter than those derived from the methanol systems, CSm and HCSm (Table 2.2). The finding again demonstrates that the micropore size of silica solid materials was linked with the mesh–size (ξ) of the polymeric silica precursors (Fig. 2.4).

It is postulated that the larger pore size of the silica powder from the ethanol system (CSe) enhanced incorporation of water molecules in the hydrolysis process than that from the methanol system (CSm), which expanded the pore size (HCSe). As shown in Fig. 2.11, CSe and HCSe exhibited wider pore–size distribution compared with CSm; secondary pores may seem to have been included in some degree. For the 1-propanol system (HCSp) or the catalyst–free system (HSm), the majority was mesopores caused by the cluster aggregation. Secondary pore structures are generally fragile against hydrolysis and poly–condensation reactions in hydrothermal treatment.

The morphologies of CSm and HCSm were observed by TEM to obtain insights into the influence of the hydrolysis treatment on the porous structures (Fig. 2.14). The comparison of these images confirmed almost the same morphologies in CSm and HCSm. The pore diameters of both CSm and HCSm were estimated to be ca. 0.5 nm.

Table 2.2.   Structural Properties of the Porous Silica Samples [a]

Sample code	d (nm)	S_{micro} (m^2 g^{-1})	S_{total} (m^2 g^{-1})	V_{micro} (m^3 g^{-1})	V_{total} (m^3 g^{-1})
CSm	< 2.0	295	515	0.141	0.26
CSe	2.1	257	588	0.11	0.31
HCSm	< 2.0	260	737	0.125	0.37
HCSe	2.8	6	780	0.004	0.46
HCSp	3.5	31	660	0.016	0.58
HSm	6.1	68	517	0.024	0.79

[a]Notation: d, average pore diameter (BET); S_{micro}, micropore surface area; S_{total}, total surface area (BET); V_{micro}, micropore volume; V_{total}, total pore volume.
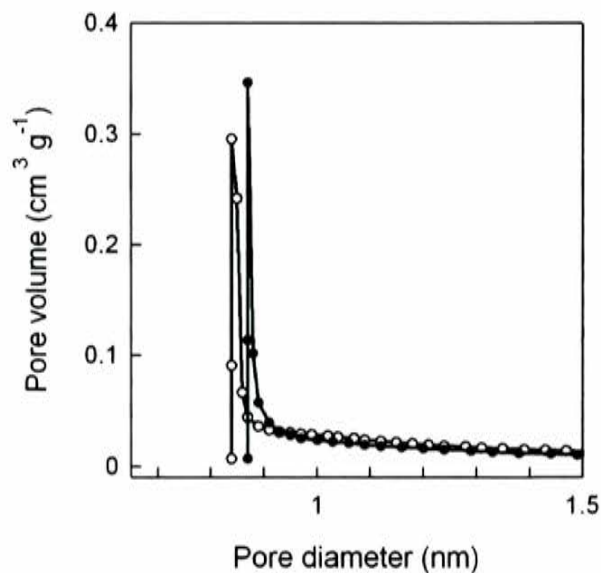

Figure 2.13.   SF-modified HK pore size distributions for the microporous silica, HCSm (open circle) and CSm (filled circle).
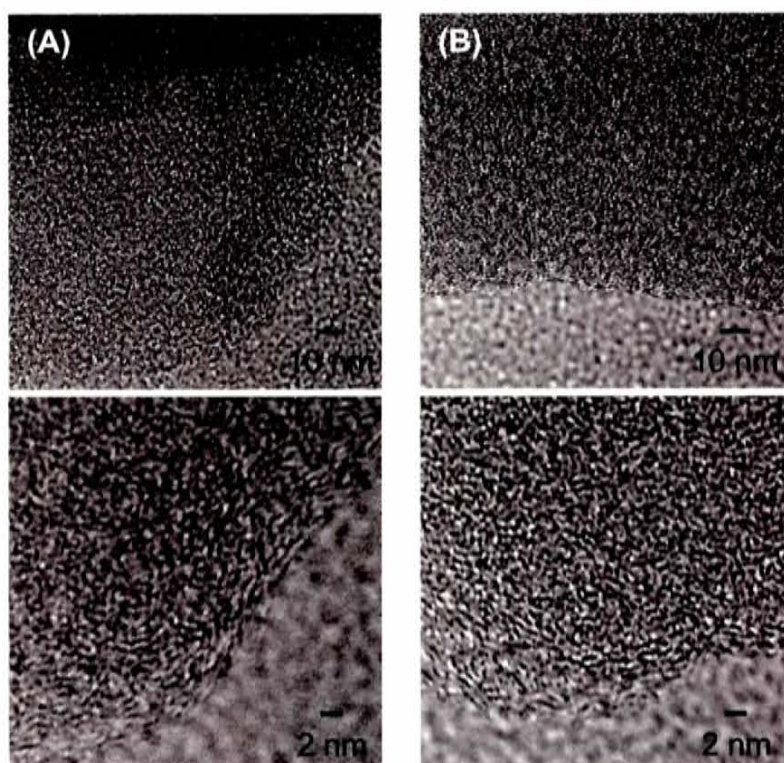
Figure 2.14. Typical TEM images of the dried silica powders, CSm (A) and the heated HCSm (B).

2.4. Conclusion

Microporous silica solids have successfully been synthesized from TMOS via the catalytic sol–gel process using the non–ionic HA catalyst. In the presence of HA, the pore size can essentially be controlled in terms of the chain length of the monohydric alcohols used in the precursor solutions, as $d < 1$ nm was attained with LCSm (TMOS/methanol/water/HA). SAXS experiments have revealed that in the methanol– and ethanol–based systems, the polymer–like silica aggregates characterized by low fractal dimensions, $d_f \sim 2$, identical to an ideal polymer chain, and the microscopic mesh–size of the transient polymer network ($\xi < 2$ nm) were generated via the condensation of partially hydrolyzed silicon alkoxides, which offered a micropore framework of the silica solids. The agglomerated sol by the heat treatment and the solid silica powders derived from LSCm also exhibited fractal scattering behavior on a similar length scale to that in LCSm. The finding is indicative of the preserved fractal nature in their internal structures, i.e., $d_f = \sim 2$ and $\xi < 2$ nm. The average pore

diameter of the silica powders derived from the ethanol system (LCSe) increased via the chemical hydrolysis treatment from 2.1 nm to 2.8 nm, accompanied by an increase in the fractal dimension ($d_f > 2$). The phenomena highlight the advantage of the robust porous architecture of the methanol–based system against the chemical hydrolysis treatment owing to the ultra–fine liquid ($\xi \sim 1$ nm) and solid ($d < 1$ nm) structures. Substitution of 1-propanol or the absence of the HA catalyst led to higher dimension branched polymers or particle–like structures in the liquid precursors, which resulted in the formation of mesopores with a diameter (> 2 nm) due to apertures between the particle-like aggregates.

References

1. Falcaro, P.; Grosso, D.; Amenitsch, H.; Innocenzi, P. J. Phys. Chem. B 2004, 108, 10942.

2. Vincent, A.; Babu, S.; Brinley, E.; Karakoti, A.; Deshpande, S.; Seal, S. J. Phys. Chem. C 2007, 111, 8291.

3. Hoshikawa, Y.; Yabe, H.; Nomura, A.; Yamaki, T.; Shimojima, A.; Okubo, T. Chem. Mater. 2010, 22, 12.

4. Jain, A.; Rogojevic, S.; Ponoth, S., Agarwal, N.; Matthew, I.; Gill, W. M.; Persans, P.; Tomozawa, M.; Plawsky, J. L.; Simonyi, E. Thin Solid Films 2001, 398, 513.

5. Hatton, B. D.; Landskron, K.; Hunks, W. J.; Bennett, M. R.; Shukaris, D.; Perovic, D. D.; Ozin, G. A. Materials Today 2006, 9, 22.

6. Wang, W. D.; Grozea, D.; Kim, A.; Perovic, D. D.; Ozin, G. A. Adv. Mater. 2010, 22, 99.

7. Thomas, I. M. Appl. Opt. 1992, 31, 6145.

8. Faustini, M.; Nicole, L.; Boissiere, C.; Innocenzi, P.; Sanchez, C.; Grosso, D.; Chem. Mater. 2010, 22, 4406.

9. Hrubesh, L. W.; Pekala, R. W. J. Mater. Res. 1994, 9, 731.

10. Yoldas, B. E.; Annen, M. J.; Bostaph, J. Chem. Mater. 2000, 12, 2475.

11. Li, L.; Yalcin, B.; Nguyen, B. N.; Meador, M. A. B.; Cakmak, M. ACS Appl. Mater. Interfaces 2009, 1, 2491.

12. Beck, J. S.; Vartuli, J. C.; Roth, W. J.; Leonowicz, M. E.; Kresge, C. T.; Schmitt, K. D.; Chu, C. T. W.; Olson, D. H.; Sheppard, E. W.; Mccullen, S. B.; Higgins, J. B.; Schlenker, J. L. J. Am. Chem. Soc. 1992, 114, 10834.

13. Zhao, D. Y.; Feng, J. L.; Huo, Q. S.; Melosh, N.; Fredrickson, G. H.; Chmelka, B. F.; Stucky, G. D. Science 1998, 279, 548.

14. Lu, Y. F.; Ganguli, R.; Drewien, C. A.; Anderson, M. T.; Brinker, C. J.; Gong, Y. X.; Soyez, H.; Dunn, B.; Huang, M. H.; Zink, J. I. Nature 1997, 389, 364.

15. Gorman, B. P.; Orozco-Teran, R. A; Roepsch, J. A.; Dong, H.; Reidy, R. F. Appl. Phys. Lett. 2001, 79, 4010.

16. Leventis, N.; Sotiriou-Leventis, C.; Zhang, G. H.; Rawashdeh, A. -M. M.; Nano Lett. 2002, 2, 957-960.

17. Xia, Z.; Riester, L.; Sheldon, B. W.; Curtin, W. A.; Liang, J.; Yin, A.; Xu, J. M. Rev. Adv. Mater. Sci. 2004, 6, 131.

18. Miyoshi, H.; Hata, N.; Kikkawa, T. Jpn. J. Appl. Phys. 2005, 44, 1166.

19. Gaire, C.; Ou, Y.; Arao, H.; Egami, M.; Nakashima, A.; Picu, R. C.; Wang, G. -C.; Lu, T. -M. J. Porous Mater. 2010, 17, 11.

20. Cha, B. J.; Kim, S.; Char, K.; Lee, J. -K.; Yoon, D. Y.; Rhee, H. -W. Chem. Mater. 2006, 18, 378.

21. Sing, K. S. W.; Everett, D. H.; Haul, R. A. W.; Moscou, L.; Pierotti, R. A.; Rouquérol, J.; Siemieniewska, T. Pure Appl. Chem. 1985, 57, 603.

22. Chu, L.; Tejedor-Tejedor, M. I.; Anderson, M. A. Microporous Mater. 1997, 8, 207.

23. Meixner, D. L.; Gilicinski, A. G.; Dyer, P. N. Langmuir 1998, 14, 3202.

24. Colomer, M. T.; Anderson, M. A. J. Non-Cryst. Solids 2001, 290, 93.

25. Kremer, S. P. B.; Kirschhock, C. E. A.; Tielen, M.; Collignon, F.; Grobet, P. J.; Jacobs, P. A.; Martens, J. A. Adv. Funct. Mater. 2002, 12, 286.

26. Groen, J. C.; Peffer, L. A. A.; Pérez-Ramírez, J. Microporous Mesoporous Mater. 2003, 60, 1.

27. Endo, A.; Miyata, T.; Akiya, T.; Nakaiwa, M.; Inagi, Y.; Nagamine, S. J. Mater. Sci. 2004, 39, 1117.

28. Di, Y.; Meng, X.; Wang, L.; Li, S.; Xiao, F. -S. Langmuir 2006, 22, 3068.

29. Brinker, C. J.; Scherer, G. W. In Sol-Gel Science, The Physics and Chemistry of Sol-Gel Processing; Academic Press: New York, 1990.

30. Tilgner, I. C.; Fischer, P.; Bohnen, F. M.; Rehage, H.; Maier, W. F. Micropor. Mater. 1995, 5, 77.

31. Lee, D. W.; Yu C. Y.; Lee, K. H. J. Phys. Chem. C 2008, 112, 5136.

32. Brinker, C. J.; Sehgal, R.; Hietala, S. L.; Deshpande, R.; Smith, D. M.; Loy, D.; Ashley, C. S. J. Membr. Sci. 1994, 94, 85.

33. Nair, B. N.; Elferink, W. J.; Keizer, K.; Verweij, H. J. Colloid Interface Sci. 1996, 178, 565.

34. Elferink, J. W.; Nair, B. N.; de Vos, R. M.; Keizer, K.; Verweij, H. J. Colloid Interface Sci. 1996, 180, 127.

35. Nair, B. N.; Elferink, J. W.; Keizer, K.; Verweij, H. J. Sol-Gel Sci. Technol. 1997, 8, 471.

36. D. W. Schaefer, Science 1989, 24, 1023.

37. Raman, N. K.; Anderson, M. T.; Brinker, C. J. Chem. Mater. 1996, 8, 1682.

38. Orthaber, D.; Bergmann, A.; Glatter, O. J. Appl. Cryst. 2000, 33, 218.

39. Glatter, O. J. Appl. Crystallogr. 1977, 10, 415.

40. Glatter, O. Acta Phys. Austriaca 1977, 47, 83.

41. Boury, B.; Corriu, R. J. P.; Strat, V. L. Chem. Mater. 1999, 11, 2796.

42. Brunaure, S.; Emmett, P. H.; Teller, E. J. Am. Chem. Soc. 1938, 60, 309.

43. Barrett, E. P.; Joyner, L. G.; Halenda, P. P. J. Am. Chem. Soc. 1951, 73, 373.

44. Horváth, G.; Kawazoe, K. J. Chem. Eng. Jpn. 1983, 16, 470.

45. Saito, A.; Foley, H. C. AIChE J. 1991, 37, 429.

46. Glatter, O.; Kratky, O.; Small-Angle X-Ray Scattering, Academic, London, 1982.

47. Ornstein, L. S.; Zernike, F. Proc. Acad. Sci. Amsterdam 1914, 17, 793.

48. Debye, P. J. Phys .Colloid Chem. 1947, 51, 18.

49. Pedersen, J.S.; Schurtenberger P. Macromolecules 1996, 29, 7602.

50. Pedersen, J.S.; Schurtenberger P. J. Polym. Sci., Part B: Polym. Phys. 2004, 42, 3081.

51. Strobl, G. R. The Physics of Polymers: Concepts for Understanding Their Structures and Behavior, 3rd ed., Springer, Berlin, 2007.

52. Toporowski P. M.; Roovers, J. E. L. Macromolecules 1978, 11 365.

53. Tande, B. M.; Wagner, N. J.; Mackay, M. E.; Hawker, C. J.; Jeong, M. Macromolecules 2001, 34, 8580.

54. Mackay, M. E.; Dao T. T.; Tuteja, A.; Ho D. L.; Horn V. H.; Kim, H-C.; Hawker, C. J. Nature materials 2003, 2, 762.

55. Fukasawa, T.; Sato, T. Phys. Chem. Chem. Phys. 2011, 13, 3187.

56. Sato, T.; Komatsu, T.; Nakagawa, A.; Tsuchida, E. Phys.Rev.Lett. 2007, 98, 208101.

57. Pouxviel, J. C.; Boilot, J. P. J. Non-Cryst. Solids 1987, 94, 374.

58. Sanchez, J.; Mccormick, A. J. Phys. Chem. 1992, 96, 8973.

59. Mazur, M.; Mlynarik, V.; Valko, M.; Pelican, P. Appl. Magn. Reson. 1999, 16, 547.

60. Boury, B.; Corriu, R. J. P.; Strat, V. L. Chem. Mater. 1999, 11, 2796.

61. Groen, J. C.; Peffer, L. A. A.; Pérez-Ramírez, J. Microporous Mesoporous Mater. 2003, 60, 1.

CHAPTER   3

Refractive Indices and Young's Modulus of

Microporous Silica Thin Films

3.1.   Introduction

Low refractive index (low-n) thin films have been employed as antireflective (AR) coatings for optical

applications including display devices, lenses and solar cells.[1-10] Magnesium fluoride is a low-n ($n = 1.38$)

material that is widely used in commercial applications. Films with lower indices (e.g., $n < 1.3$) are desired for

obtaining high transmittance. Such films may be attained by incorporation of nanosized pores filled with air

having $n = 1.0$. However, preparation of magnesium fluoride with nanosized pores is not trivial.

A promising candidate is highly porous silica, which can be in the form of particles[2,4,8], xerogel[12,13] or aerogel[11,14]. Silica has a low-n (n = 1.46), good durability and environmental resistance[7,19] and can be used for optical applications, microelectronics[15-18] and thermal applications[14]. However, increasing the content of nanosized pores is generally expected to greatly deteriorate the mechanical strength of the film[11]. This problem has stimulated many studies[16,17,20-22] regarding reinforcement of porous silica materials. For example, Reidy et al. reported that fluorination of silica improved the mechanical strength of porous silica. The resultant film had an average pore size of about 20 nm, elastic modulus of 14 GPa, and n = 1.24.[20] Luo et al. reinforced porous silica with colloidal silica nano particles[22], yielding a film with a low-n of 1.28, Young's modulus of 16.6 GPa, and hardness of 0.92 GPa. Although high-density spherical silica nano particles should have high hardness, their introduction into the film matrix may roughen the surface and cause terrible increment of light scattering. Further improvement of these films in terms of their Young's modulus and transparency is quite necessary. Investigations focusing on pore structures, pore uniformity and film formation process will be helpful for obtaining stronger and more transparent films.

Porous silica is typically mesoporous[8,11,16,17] with pores 2–50 nm in diameter[23]. As shown in recent investigations, formation of micropores < 2 nm in diameter[23] would be favorable in order to increase the mechanical strength.[24,25,26] Furthermore, micropores would probably eliminate penetration and adsorption of chemical species[21] which give rise to light scattering and absorption. As for microporous silica film is well known as packed silica nanoparticles[27-31] and monolithic microporous silica[32-41]. Silica is promising high optical transparency, but nanoparticles tend to form inhomogeneous aggregation during packing process, which causes nonuniform density distribution and light scattering. In addition, pore volume fraction of dead space in packed silica nanoparticles is limited because of its formation principle. On the other hand, monolithic microporous silica consists of solid skeleton and void structure, which is usually prepared by template technique using organic-functionalized silicon alkoxides[32,33,35,41] or additive organic precursors[37-40,42] to create the pores. However, heat treatment above 400 °C to remove these organics and form micropores inevitably results in

collapse of pores itself. This contracts the film, which increases the film density and n. Moreover, residual organic functional groups or additives also increase n. Alternative processes of the monolithic microporous silica fabrication are still worth investigation.

In the Chapter 2, a catalytic sol-gel process using tetramethyl orthosilicate (TMOS) and the non-ionic catalyst hydroxyacetone was demonstrated. In this chapter, this method is applied to fabricate microporous silica thin film with low-n and high Young's modulus. The homogeneous reaction with the non-ionic catalyst facilitates production of highly porous monolithic microporous silica with uniform pores < 1 nm in diameter. Because this process requires no sacrificial templates, residual alkoxy groups and the catalyst are easily removed during hydrolysis. Additionally, the process temperature can be as low as 80 °C, which results in less thermal stress. This also prevents the pore structures from collapsing, which aids in production of uniform pores with large volumes.

3.2. Experimental Section

3.2.1. Sample preparation

To produce the film coating solution, TMOS ($Si(OCH_3)_4$, Tokyo Chemical Industry, > 98 %), ethanol (Wako, > 99.5 %), distilled water and hydroxyacetone (CH_3COCH_2OH, Tokyo Chemical Industry, > 80 %) were mixed thoroughly at 25 °C for 2 days, and then kept at 40 °C for 3 days. The molar ratio of $Si(OCH_3)_4$:H_2O:C_2H_5OH:CH_3COCH_2OH was 1:5:27.5:1. Si(100) substrates were coated with the silica sol by spin coating at 2000 rpm for 60 s at 25 °C, and dried at 25 °C for a day. The dried silica films were then either heated at 200 °C for 2 h (non-hydrolyzed film, MS_{200}), or immersed in water at 80 °C for 2 h to chemically hydrolyze the methoxy groups and remove organic compounds. After chemical hydrolysis, the films were dried and heated at 80–300 °C for 2 h (HMS_{80-300}) to promote the condensation reaction of silanol groups and eliminate pore water. Table 3.1 summarizes the preparation conditions for each sample.

3.2.2. Characterization

The n and film thickness were measured with a spectroscopic ellipsometer (Horiba Jobin Yvon, UVISEL M200) at 80 °C, which minimized water adsorption. The mass fraction of water in the film prepared with hydrolysis but no heating was estimated to be approximately 15 % by thermogravimetric analysis. A flake of the film was observed using a transmission electron microscope (TEM, JEOL, JEM-2010) with an acceleration voltage of 200 kV. The surface morphology and the cross-section of a typical film were observed using a field-emission scanning electron microscope (FE-SEM, Hitachi, S-5000) and an atomic force microscope (AFM, Seiko Instruments, SPA400). The pore volume and surface area of the dried silica coating solution was evaluated by nitrogen gas adsorption-desorption measurement (Micromeritics, ASAP2010). Micropore volume and surface area were calculated from adsorption isotherm data using the t-plot method (0.35 nm $< t <$ 0.5 nm) [39,43]. Total pore volumes were determined from the volume of adsorbed nitrogen gas at a relative pressure of 0.95 [23]. The pore size distributions were determined by the Saito-Foley (SF) modified Horváth-Kawazoe (HK) model from adsorption isotherms in the low relative pressure region. The HK model[44] describes a semiempirical calculation of the pore size distribution from the nitrogen adsorption isotherm in microporous materials with slit-like pores, and is applicable to active carbon. The SF modified HK model[45] extends application to the cylindrical pore geometry of microporous materials such as zeolite and silica, which have been used in many studies of microporous silica[41,43,46]. A Fourier transform infrared spectrophotometer (FT-IR, Perkin-Elmer 1650) was used to record spectra of the dried silica sol mixed with KBr from 4000–450 cm^{-1}.

The mechanical properties of the films were measured at room temperature by nanoindentation (Agilent Technologies NanoIndenter G200, Berkovich diamond indenter) based on ISO-14577[47]. Sixteen points on each sample were assayed using the continuous stiffness measurement (CSM), and the average and standard deviation were calculated. The first 10 % of the film thickness was used as the indentation depth range to determine Young's modulus and hardness, and the values were compared with corresponding results from other samples. The Poisson ratio of silica films is 0.25 as calculated using Young's modulus.

Table 3.1. Summary of the Preparation Process for Each of the Silica Films and Powders.

Sample code	Chemical Hydrolysis[a]	Heat Treatment Temperature[b] ($^{\circ}C$)
HMS_{80}	Yes	80
HMS_{150}	Yes	150
HMS_{200}	Yes	200
HMS_{250}	Yes	250
HMS_{300}	Yes	300
MS_{200}	No	200

[a]The film and powder samples were chemically hydrolyzed by immersing them in water at 80 $^{\circ}C$ before [b]heat treatment.

3.3. Results and Discussion

Figure 3.1(A) shows a typical FE-SEM cross-sectional image of the silica film HMS_{250}. The film thickness was estimated at approximately 125 nm. In the AFM image (Fig. 3.1(B)) and cross-sectional AFM profile (Fig. 3.1(C)) the film appeared very smooth with small ridges approximately 3 nm in height. The morphology of the micropores was undetectable by FE-SEM and AFM, due to the size (< 2 nm diameter) of the pores. Pores of approximately 0.5 nm in diameter with a narrow size distribution were observed in the TEM image of a typical flake of silica film (Fig. 3.1(D)).

N_2 gas adsorption-desorption isotherms of the silica powders HMS_{150}, HMS_{200}, HMS_{300} and MS_{200} (Fig. 3.2) were used to classify them as IUPAC type I with monolayer adsorption of N_2,[23] which probably contains micropores with diameters < 2 nm. The isotherm of the silica powder HMS_{250} had significant overlap with that of HMS_{300}, and consequently HMS_{250} is not depicted in Fig. 3.2. In the t-plot (Fig. 3.3(A)) calculated from nitrogen adsorption isotherm data for HMS_{200} the curve did not pass through the origin and had a positive

y-intercept, which indicates HMS_{200} is microporous. The specific surface area of a micropore in HMS_{200} was

calculated to be 470 $m^2 g^{-1}$, and the pore volume was calculated to be 0.21 $cm^3 g^{-1}$. The pore size distribution in

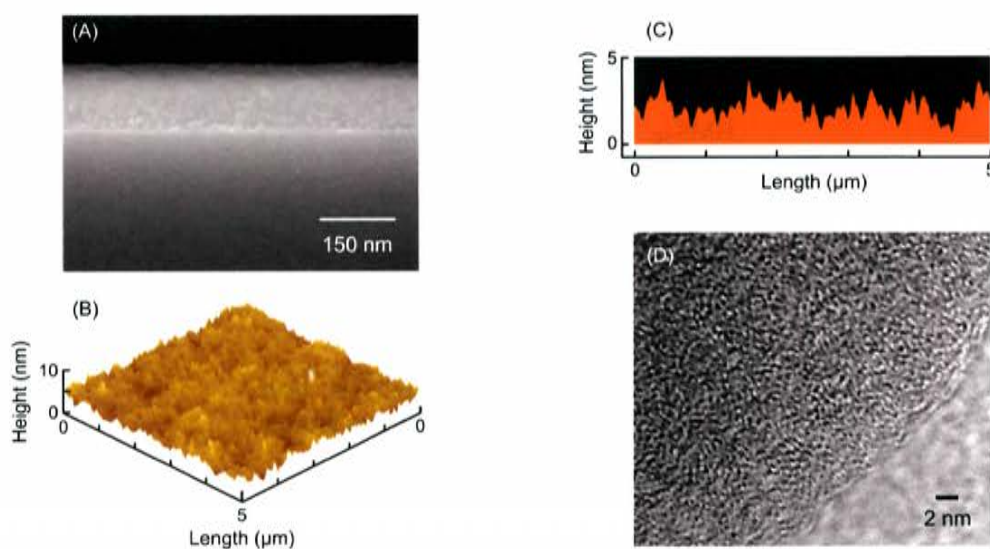HMS_{200} (Fig. 3.3(B)) is the narrowest of all reported microporous silica.[32,34-36,39]

Figure 3.1. Typical images of the silica film HMS_{250}: (A) cross sectional SEM image, (B) AFM image, (C) cross sectional AFM profile measured along the indicated plane, and (D) TEM image.
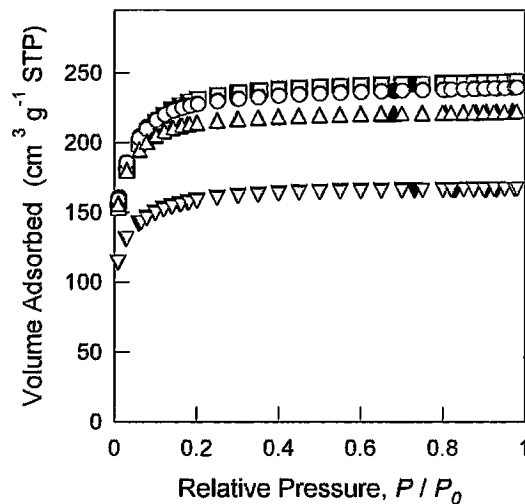
Figure 3.2. Nitrogen adsorption-desorption isotherms of the chemically hydrolyzed silica powders heat-treated at different temperatures (HMS_{150} (circle), HMS_{200} (square) and HMS_{300} (triangle)) and the non-hydrolyzed silica heat-treated at 200 °C (MS_{200} (inverted triangle)). Adsorption isotherms are represented by open symbols and desorption isotherms by solid symbols.

The total pore volume for the hydrolyzed silica powder HMS_{150} was 0.37 cm^3 g^{-1} (Table 3.2). Little change in the pore volume was observed when the hydrolyzed silica powders were heated at 200 °C (0.38 cm^3 g^{-1}), 250 °C (0.34 cm^3 g^{-1}) and 300 °C (0.34 cm^3 g^{-1}). The pore volume for the non-hydrolyzed silica powder MS_{200} (0.26 cm^3 g^{-1}) was smaller than that for the hydrolyzed silica HMS_{200} (0.38 cm^3 g^{-1}). The pore volume fraction is related to the refractive index according to the Lorentz-Lorenz equation[6,8,12]

$$(1 - V_p) \times \left(\frac{n_i^2 - 1}{n_i^2 + 2} \right) = \left(\frac{n_f^2 - 1}{n_f^2 + 2} \right) \quad (3.1)$$

where V_p is a volume fraction of pores and n_i and n_f are a refractive index of a framework materials composing a film and a porous film, respectively. This explains that the increasing of the pore volume decreases the refractive index. In order to enhance the specific pore volume value, the synthesis procedure in which ethanol was used as the solvent instead of methanol was developed,[43] achieving the increase of maximum pore volume from 0.33 cm^3 g^{-1} to 0.38 cm^3 g^{-1} without expanding pore diameter.

It is believed that the homogeneous hydrolysis reaction in the presence of hydroxyacetone catalyst facilitates formation of micropores. The framework of micropores might have already been fabricated in silica

precursors in the coating solution. The dried silica coating solution includes a lot of micropores, and therefore, all of the silica powders considered in this work had large pore volume. High temperature heating should cause densification with the condensation reaction, and consequently the total pore volumes of the silica powders heated at ≥ 250 °C were smaller than that of HMS_{150} and HMS_{200}.

Film thickness and n for each silica film are summarized in Table 2. Within the wavelength range 250–800 nm, the n were lower for the hydrolyzed films than the non-hydrolyzed film (Fig. 3.4). Figure 3.5(A) compares the FT-IR absorption spectra from 3200–2700 cm^{-1} for HMS_{200} and MS_{200}. Peaks at 2980 and 2860 cm^{-1} for the C-H stretching mode of CH_3 and CH_2, respectively[17], were observed in the spectra of MS_{200} but not HMS_{200}. This suggests that organics, such as methoxy groups and hydroxyacetone, remained in the non-hydrolyzed silica but were removed during the process of chemical hydrolysis. The absence of these organics definitely facilitates reduction of n and increases the pore volume of the hydrolyzed films.
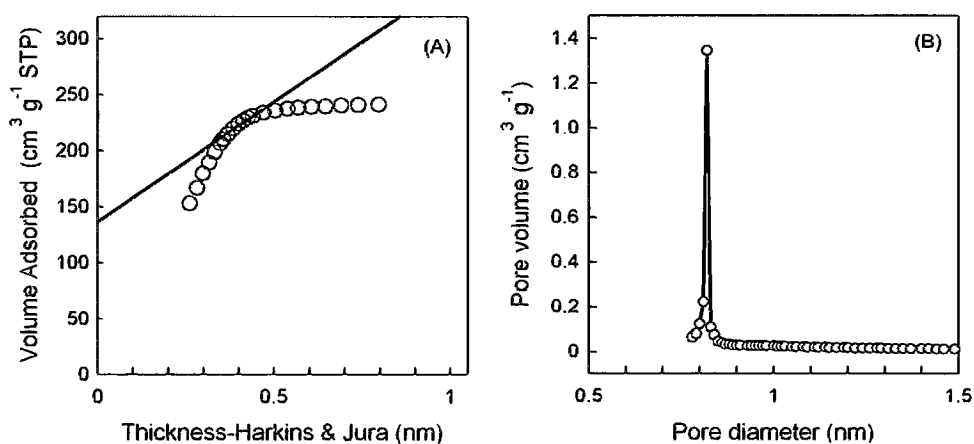

Figure 3.3. t-Plot curve (A) and pore size distribution (B) of the hydrolyzed silica powder HMS_{200}.

The n of the hydrolyzed film decreased as the temperature for heat treatment was increased to 250 °C. The dependence of the n on wavelength changed with the temperature the film was heated at. When the hydrolyzed silica film was heated at 250 or 300 °C, the n was independent of the wavelength. The FT-IR absorption spectra from 1800–500 cm^{-1} of the hydrolyzed silica films HMS_{80}, HMS_{150}, HMS_{200} and HMS_{250} are compared in Fig.

5(B). The absorption band near 950 cm^{-1} can be attributed to stretching vibrations of the Si-OH bonds[8,12], and is

observed in the spectra of HMS$_{80}$, HMS$_{150}$ and HMS$_{200}$. The peak height for the asymmetric stretching

vibration of Si-O-Si (TO$_3$ mode) at about 1080 cm^{-1} [8,12,17] increased with increasing heating temperature. In

contrast, the Si-OH peak height decreased with increasing heating temperature, and was not apparent in the

spectrum of HMS$_{250}$. These results suggest that the terminal silanol groups were almost completely converted

to Si-O-Si bonds with thermal dehydroxylation and condensation[48] at 250 °C.

Although the total pore volume decreased when the heating temperature was $\geq$250 °C, the n of HMS$_{250}$

was lower than that of HMS$_{200}$ (Table 3.2). This is due to a reduction in the absorption of water for the high

temperature film. Typically, hydrophilic silanol groups aid adsorption of water, and high polarization of water

and silanol groups must increase the n of the film[7,16,24]. When the film is heated at $\geq$250 °C the number of

terminal Si-OH is decreased (Fig. 3.5(B)), which should reduce the adsorption of water and decrease n to <1.3.

As discussed earlier, the pore volume of the hydrolyzed silica powder HMS$_{250}$ was 0.34 cm^3 g^{-1}. A pore

volume fraction of 42.8 % was calculated using the density of dense silica (2.20 g cm^{-3}). This was used to

calculate n=1.23 by substituting n=1.46 for dense silica into the Lorentz-Lorenz equation (Eq. 3.1). The

experimental n of 1.27, which was determined by ellipsometric measurement (Table 3.2), is larger than the

calculated n, which should be due to residues such as water in the experimental film.

Table 3.2. Structural Properties and Refractive Indices of the Microporous Silica Samples [a]

Sample code	S_{micro} [b]	V_{micro} [b]	V_{total} [b]	n_{633} [c]	t [c]
	$(m^2\,g^{-1})$	$(m^3\,g^{-1})$	$(m^3\,g^{-1})$		(nm)
HMS$_{80}$	N/A	N/A	N/A	1.340	132
HMS$_{150}$	575	0.26	0.37	1.319	135
HMS$_{200}$	470	0.21	0.38	1.278	130
HMS$_{250}$	482	0.22	0.34	1.270	128
HMS$_{300}$	532	0.24	0.34	1.265	130
MS$_{200}$	350	0.16	0.26	1.358	162

[a]Notation: S_{micro}, micropore surface area; V_{micro}, micropore volume; V_{total}, total pore volume; n_{633}, refractive index at 633 nm; t, film thickness. [b]Powder samples were evaluated. [c]Film samples were estimated by ellipsometric measurement.
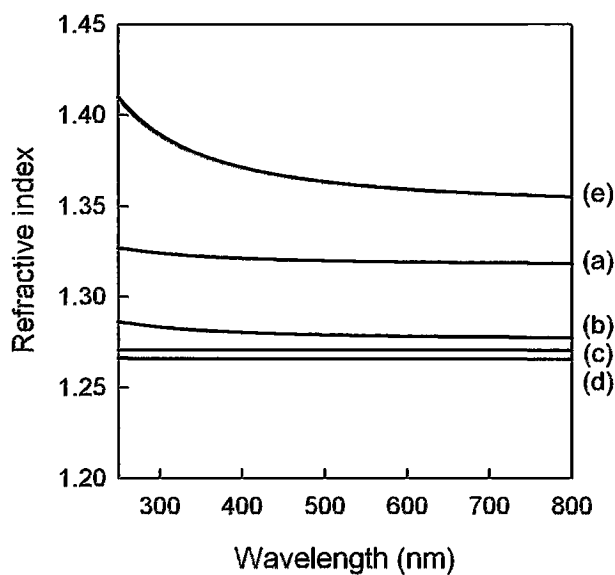

Figure 3.4. Refractive index as a function of wavelength for HMS$_{150}$ (a), HMS$_{200}$ (b), HMS$_{250}$ (c) HMS$_{300}$ (d), and MS$_{200}$ (e).
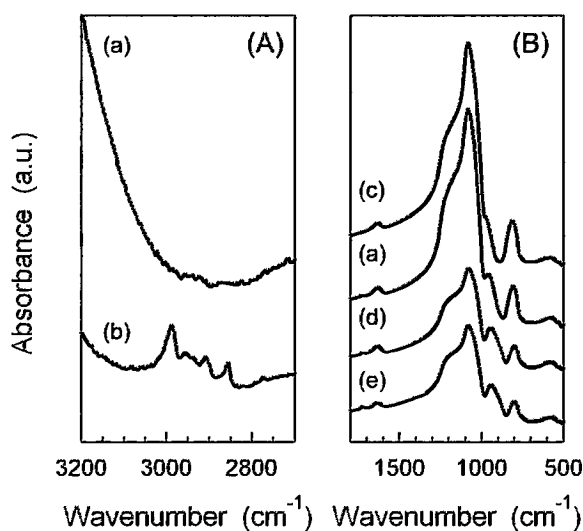
Figure 3.5. FT-IR spectra of the hydrolyzed silica film HMS_{200} (a), the non-hydrolyzed silica film MS_{200} (b), and the hydrolyzed silica films HMS_{250} (c), HMS_{150} (d) and HMS_{80} (e).

Mechanical strengths were determined for the hydrolyzed silica film HMS_{300}. In consideration of the substrate effect, two different thicknesses of 125 nm and 240 nm were adopted. Young's modulus was 19.4 ± 0.91 GPa and the hardness was 0.45 ± 0.03 GPa at an indentation depth of 12.5 nm for the 125 nm thick film, while the corresponding values were 19.5 ± 0.91 GPa and 0.74 ± 0.04 GPa at an indentation depth of 24 nm for the 240 nm thick film (Fig. 3.6).

Young's modulus of this film is the highest of all reported porous silica thin films with equivalent porosity or n.[16,17,20-22,26,31,49] In this work, tetrafunctional silicon alkoxide was used as a reagent for the microporous silica film. This reagent produced more cross-linking bonds between pore structures than trifunctional alkoxides and reagents containing alkyl groups, such as triethoxyfluorosilane[16,20] and silsesquioxane[21,26,42]. Moreover, unreacted methoxy groups and silanol groups were not present in the hydrolyzed silica powder heated at >250 °C, and instead these formed Si-O-Si bonds (Figs. 3.5(A) and 3.5(B)). These results indicate the chemical hydrolysis and thermal condensation increased the bonding between the micropores and made the film stronger. At the same porosity, the density in number of walls per unit volume in a microporous material is higher than in a mesoporous material. Consequently, because stress acting on a material might disperse into the walls, it is

expected that this stress is reduced in a microporous material compared with a mesoporous material. As a result, the pore structure in a microporous material should not collapse as easily as in a mesoporous material. A recent theoretical study has revealed that uniformity of pore diameter increases elastic modulus of silica thin film.[50] Therefore, the uniform pores of the hydrolyzed silica film result in a homogeneous wall density distribution, which provides high resistance to elastic variation.
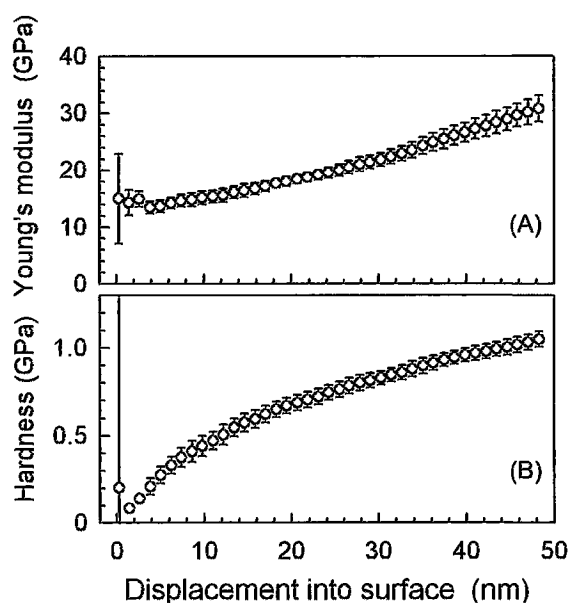

Figure 3.6. Young's modulus (A) and hardness (B) values of HMS_{300} as a function of the indentation depth from surface. The thickness of the silica film used in this study was 240 nm.

3.4. Conclusion

Low-n ($n<1.3$) was achieved with the introduction of large volume micropores in silica films. Film preparation utilized the sol-gel process with the catalyst hydroxyacetone. A low-n ($n=1.27$) was facilitated by removal of organic functional groups and the catalyst during the process of hydrolysis, and of adsorbed water and OH groups by heating (250–300 °C). The films have very small pores, which could protect against absorption or penetration of pollutants and other materials. Furthermore, due to their high Young's modulus (>15 GPa) these films are robust.

References

1. Yoldas, B. E. Appl. Opt. 1980, 19, 1425.

2. Thomas, I. M. Appl. Opt. 1992, 31, 6145.

3. Ibn-Elhaj, M.; Schadt, M. Nature 2001, 410, 796.

4. Prevo, B. G.; Hwang, Y.; Velev, O. D. Chem. Mater. 2005, 17, 3642.

5. Xi, J. -Q.; Kim, J. K.; Schubert, E. F. Nano Lett. 2005, 5, 1385.

6. Cho, J.; Hong, J.; Char, K.; Caruso, F. J. Am. Chem. Soc. 2006, 128, 9935.

7. Konjhodzic, D.; Schroter, S.; Mariow, F. Phys. Stat. Sol. A 2007, 204, 3676.

8. Vincent, A.; Babu, S.; Brinley, E.; Karakoti, A.; Deshpande, S.; Seal, S. J. Phys. Chem. C 2007, 111, 8291.

9. Chhajed, S.; Schubert, M. F.; Kim, J. K.; Schubert, E. F. Appl. Phys. Lett. 2008, 93, 251108.

10. Hoshikawa, Y.; Yabe, H.; Nomura, A.; Yamaki, T.; Shimojima, A.; Okubo, T. Chem. Mater. 2010, 22, 12.

11. Leventis, N.; Sotiriou-Leventis, C.; Zhang, G. H.; Rawashdeh, A. -M. M.; Nano Lett. 2002, 2, 957.

12. Falcaro, P.; Grosso, D.; Amenitsch, H.; Innocenzi, P. J. Phys. Chem. B 2004, 108, 10942.

13. Zhou, Y.; Schattka, J. H.; Antonietti, M. Nano Lett. 2004, 4, 477.

14. Hrubesh, L. W.; Pekala, R. W. J. Mater. Res. 1994, 9, 731.

15. Jain, A.; Rogojevic, S.; Ponoth, S., Agarwal, N.; Matthew, I.; Gill, W. M.; Persans, P.; Tomozawa, M.; Plawsky, J. L.; Simonyi, E. Thin Solid Films 2001, 398, 513.

16. Gorman, B. P.; Orozco-Teran, R. A; Roepsch, .J. A.; Dong, H.; Reidy, R. F. Appl. Phys. Lett. 2001, 79, 4010.

17. Chen, J. Y.; Pan, F. M.; Cho, A.T.; Chao, K. J.; Tsai, T. G.; Wu, B. W.; Yang, C. M.; Chang, L. J. Electrochem. Soc. 2003, 150, F123.

18. Ro, H. W.; Peng, H.; Niihara, K.; Lee, H. J.; Lin, E. K.; Karim, A.; Gidley, D. W.; Jinnai, H.; Yoon, D. Y.; Soles, C. L. Adv. Mater. 2008, 20, 1934.

19. Biswas, P. K.; Devi, P. S.; Chakraborty, P. K.; Chatterjee, A.; Ganguli, D.; Kamath, M. P.; Joshi, A. S. J. Mater. Sci. Lett. 2003, 22, 181.

20. Dong, H.; Gorman, B. P.; Zhang, Z.; Orozco-Teran, R. A; Roepsch, .J. A.; Mueller, D. W.; Kim, M. J.; Reidy, R. F. J. Non-Cryst. Solids 2004, 350, 345.

21. Cha, B. J.; Kim, S.; Char, K.; Lee, J. -K.; Yoon, D. Y.; Rhee, H. -W. Chem. Mater. 2006, 18, 378.

22. Luo, J. -T.; Wen, H. -C.; Chang, Y. -M.; Wu, W. -F.; Chou, C. -P. J. Colloid Interface Sci. 2007, 305, 275.

23. Sing, K. S. W.; Everett, D. H.; Haul, R. A. W.; Moscou, L.; Pierotti, R. A.; Rouquérol, J.; Siemieniewska, T. Pure Appl. Chem. 1985, 57, 603.

24. Hatton, B. D.; Landskron, K.; Hunks, W. J.; Bennett, M. R.; Shukaris, D.; Perovic, D. D.; Ozin, G. A. Materials Today 2006, 9, 22.

25. Xia, Z.; Riester, L.; Sheldon, B. W.; Curtin, W. A.; Liang, J.; Yin, A.; Xu, J. M. Rev. Adv. Mater. Sci. 2004, 6, 131.

26. Gaire, C.; Ou, Y.; Arao, H.; Egami, M.; Nakashima, A.; Picu, R. C.; Wang, G. -C.; Lu, T. -M. J. Porous Mater. 2010, 17, 11.

27. Chu, L.; Tejedor-Tejedor, M. I.; Anderson, M. A. Microporous Mater. 1997, 8, 207.

28. Meixner, D. L.; Gilicinski, A. G.; Dyer, P. N. Langmuir 1998, 14, 3202.

29. Colomer, M. T.; Anderson, M. A. J. Non-Cryst. Solids 2001, 290, 93.

30. Kremer, S. P. B.; Kirschhock, C. E. A.; Tielen, M.; Collignon, F.; Grobet, P. J.; Jacobs, P. A.; Martens, J. A. Adv. Funct. Mater. 2002, 12, 286.

31. Groen, J. C.; Peffer, L. A. A.; Pérez-Ramírez, J. Microporous Mesoporous Mater. 2003, 60, 1.

32. Brinker, C. J.; Ward, T. L.; Sehgal, R.; Raman, N. K.; Hietala, S. L.; Smith, D. M.; Hua, D. W.; Headley, T. J. J. Membrane Sci. 1993, 77, 165.

33. Raman, N. K.; Brinker, C. J. J. Membrane Sci. 1995, 105, 273.

34. Nair, B. N.; Elferink, J. W.; Keizer, K.; Verweij, H. J. Sol-Gel Sci. Technol. 1997, 8, 471.

35. Lu, Y.; Cao, G.; Kale, R. P.; Prabakar, S.; López, G. P.; Brinker, C. J. Chem. Mater. 1999, 11, 1223.

36. Lu, Y.; Fan, H.; Doke, N.; Loy, D. A.; Assink, R. A.; LaVan, D. A.; Brinker, C. J. J. Am. Chem. Soc. 2000, 122, 5258.

37. Kruk, M.; Asefa, T.; Jaroniec, M.; Ozin, G. A. J. Am. Chem. Soc. 2002, 124, 6383.

38. Endo, A.; Miyata, T.; Akiya, T.; Nakaiwa, M.; Inagi, Y.; Nagamine, S. J. Mater. Sci. 2004, 39, 1117.

39. Di, Y.; Meng, X.; Wang, L.; Li, S.; Xiao, F. -S. Langmuir 2006, 22, 3068.

40. Wang, R.; Han, S.; Hou, W.; Sun, L.; Zhao, J.; Wang, Y. J. Phys. Chem. C 2007, 111, 10955.

41. Wei, Q.; Wang, F.; Nie, Z. -R.; Song, C. -L.; Wang, Y. -L.; Li, Q. -Y. J. Phys. Chem. B 2008, 112, 9354.

42. Lee, K. H.; Yim, J. -H.; Baklanov, M. R. Microporous Mesoporous Mater. 2006, 94, 113.

43. Boury, B.; Corriu, R. J. P.; Strat, V. L. Chem. Mater. 1999, 11, 2796.

44. Horváth, G.; Kawazoe, K. J. Chem. Eng. Jpn. 1983, 16, 470.

45. Saito, A.; Foley, H. C. AIChE J. 1991, 37, 429.

46. Hawkins, K. M.; Wang, S. S. -S.; Ford, D. M.; Shantz, D. F. J. Am. Chem. Soc. 2004, 126, 9113.

47. ISO 14577-1:2002, Metallic materials—Instrumented indentation test for hardness and materials parameters—Part 1: Test method; International Organization for Standardization: Geneva, Switzerland, 2002.

48. Brinker, C. J.; Scherer, G. W. In Sol-Gel Science, The Physics and Chemistry of Sol-Gel Processing; Academic Press: California, 1990.

49. Takada, S.; Hata, N.; Seino, Y.; Fujii, N.; Kikkawa, T. J. Appl. Phys. 2006, 100, 123512.

50. Miyoshi, H.; Hata, N.; Kikkawa, T. Jpn. J. Appl. Phys. 2005, 44, 1166.

CHAPTER   4

Superhydrophilicity of Microporous Silica Thin Films

4.1. Introduction

Anti–fogging treatments can keep glass and plastic surfaces, such as car windows, bathroom mirrors,

camera lenses, eyeglasses, greenhouses and so forth, from getting fogged. Fogging on the surface is caused

when water vapor condenses and then forms water droplets due to the surface tension of water. Water

molecules are more attracted to each other than air molecules, forming a spherical shape. The anti–fog coating

material offers a hydrophobic or a superhydrophilic surface (contact angles of water droplets are less than 10°);

whereas the hydrophobic coating repels water to form droplets which roll on the surface, the water spreads out

on the superhydrophilic coating without becoming drops of water.

A titania coating shows a remarkable antifogging effect. Both superhydrophilicity and superoleophilicity are induced on a titania surface by ultraviolet (UV) irradiation.[1] The titania coating first needs to be irradiated by UV light for inducing those effect and does not work for long time in the dark. Hydrophilic coating solutions have been synthesized by adding glycidoxypropyl- trimethoxysilane (GPS) to the colloidal silica suspensions adjusted to different pHs, with which a polyethylene terephthalate (PET) substrate is coated.[2] The superhydrophilicity of the coating is developed by the preparation of a coating solution under strongly acidic conditions (pH 1–2). Although this needs no light exposure, the glycidoxypropyl group remains after the complete hydrolysis of the alkoxy group has occurred. Those organic residues would degrade a surface function for long-term operation.

Recently, Bico et al. quantitatively discussed the wetting of a solid textured by a designed roughness.[3] For a hydrophilic solid substrate, the liquid–solid contact is favored and the hydrophilicity is enhanced by the surface roughness. The liquid is in contact with a rough surface which consists of the solid and pores. Considering both air and liquid with which the pore is filled, the contact angle is described by the following equation,

$$\cos \theta^* = \phi_s \cos \theta_s + (1 - \phi_s) r_a \cos \theta_a + (1 - \phi_s)(1 - r_a) \cos \theta_l \quad (4.1)$$

where θ^* is the apparent contact angle of the liquid on the rough surface, θ_s is the contact angle of the liquid on the smooth surface of the solid, ϕ_s is the fraction of the base of the liquid drop in contact with the solid, θ_a is the contact angle of the liquid on the air with which the pore is filled ($\theta_a = \pi$), r_a is the fraction of the open cross–section of the pore filled with air, and θ_l is the contact angle of the liquid on the liquid with which the pore is filled ($\theta_l = 0$). The above formula (4.1) can be transformed into

$$\cos \theta^* = (1 - \phi_s)(1 - 2r_a) + \phi_s \cos \theta_s. \quad (4.2)$$

For the porous material, the fraction of the base of the liquid drop in contact with the solid is small. The apparent contact angle of the liquid on the porous material surface decreases with a decrease in the fraction of

the top of the pore filled with the air. During the measurement of the contact angle of water, the water is dropped onto the surface in order to fill the pore. r_a in Eq. 4.2 is then almost zero as

$$\cos\theta^* = 1 - \phi_s(1 - \cos\theta_s). \quad (4.3)$$

Practically, it is hard for the large part of pores to fill with and retain water because the exposed water at surface is easily dried under the ordinary conditions of temperature and humidity. The volume fraction of the pore filled with water under general conditions is important to enhance the hydrophilicity. The multifunctional nanoporous thin films, which exhibit both the hydrophilic wetting characteristic and a low refractive index, have been reported by Cebesi and co-workers.[4] The superhydrophilicity is developed in porous material involving the pores filled with water, whereas the porous material with a low refractive index involves the pores filled with air.

The adsorption types of water depend on the pore sizes; i.e., the monolayer adsorption of water on the surface of micropores and multilayer adsorption of water on the surface of mesopores. If almost the entire surface of the porous material consists of the inner surface of micropores, only the monolayer adsorption of water occurs and the adsorption strength simply depends on the hydrogen bond strength between a water molecule and an oxygen atom at the inner surface of the micropores.

4.2. Experimental Section

4.2.1. Thin film preparation

The solution used for the microporus silica coating is synthesized from a mixture of tetramethyl orthosilicate (Si(OCH₃)₄, Kanto >98%), water, hydroxyacetone (CH₃COCH₂OH, Kanto >80%) as the catalyst, and methanol (Wako >99.5%) as the solvent. The molar ratio of $Si(OCH_3)_4$: H_2O : CH_3COCH_2OH is 1 : 1 : 5. Water is deionized by an AQUARIUS GS-200 System (Advantec), while the other reagents are used without further purification. The mixture is stirred at 25 °C for 24 hours and then aged at 40 °C for four days. 2-ethoxyethanol (Wako > 98%) is added to the solution, and methanol is removed by evaporation in order to

smooth the surface of the coating film. The coating solution is dropped onto a PET (SANPLATEC), nonluminescent quartz plate (Tosoh) or mirror polished silicon wafer (Komatsu Electronics > 99.9999 %) and spun at 1000 rpm for 60 s at 25 °C. The coating on the substrate is dried at 25 °C or 80 °C for two hours, immersed in water at 80 °C for two hours and then dried at 25 °C.

4.2.2. Characterization

The pore structure of the coating is determined by the nitrogen gas adsorption/desorption technique (Micromeritics ASAP2020) for the bulk gel prepared from identical silicate precursors. The thickness of the coatings is measured using a surface profilometer (ULVAC Dektak 6M). The pencil hardness on a silicon wafer is measured by a Japanese Industrial Standard method (JIS–K–5400). The optical transmission spectra of the coating on a quartz glass are obtained using an UV–visible spectrometer (Shimadzu UV–2100) in the wavelength range of 300–800 nm. The surface morphology of the coating on a silicon wafer was observed using an atomic force microscope (AFM, Seiko Instruments SPA400). The surface wettability of the coating on a silicon wafer was evaluated from the contact angle measurement at room temperature using a contact angle meter (Kyowa Interface Science DropMaster 300). The averaged contact angle was calculated from five measured values at different points of the coating. The Fourier transform infrared (FT–IR) spectra of the coating were measured with an FT–IR spectrometer (Shimadzu IRPrestige–21), which was attached to an attenuated total reflection (ATR) unit equipped with a monolithic diamond prism crystal, in the range of 700–4000 cm^{-1}.

4.3. Results and Discussion

The superhydrophilicity was developed by coating a PET substrate with microporous silica and immersing the microporous silica coating in water at 80 °C as compared to hydrophobicity of a bare PET substrate. Figure 4.1 shows that a water droplet spread out on the superhydrophilic silica–coated PET, while a semispherical droplet of water remained on the hydrophobic bare PET.
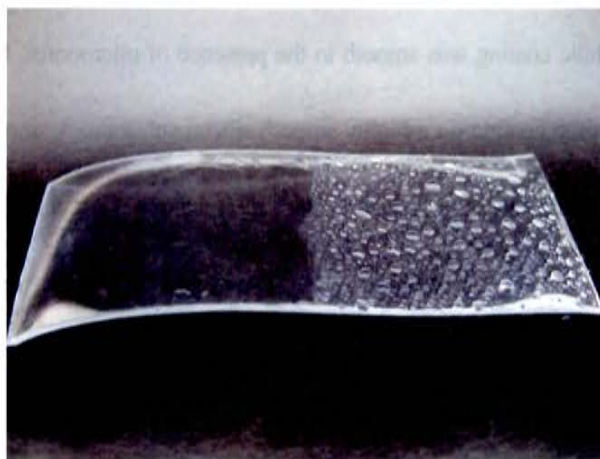
Figure 4.1. A superhydrophilic coating on a PET substrate on the left half and a hydrophobic bare PET substrate on the right half. After coating half of the substrate with microporous silica, the coatings are immersed in water at 80 °C for two hours that causes hydrolysis of the remaining alkoxy groups. Water is sprayed after drying the half–coated substrate at 25 °C for one day.

The superhydrophilic coating of silica was highly transparent as shown in the inset of Fig. 4.2. Transparent quartz was used as a substrate instead of the PET since the surface of the PET substrate is rough. Figure 4.2 shows the optical transmission spectra of the coating on a transparent substrate of quartz in the wavelength range of 300–800 nm. The transmittance of the silica coating reached approximately 100% of incidence in the visible region.
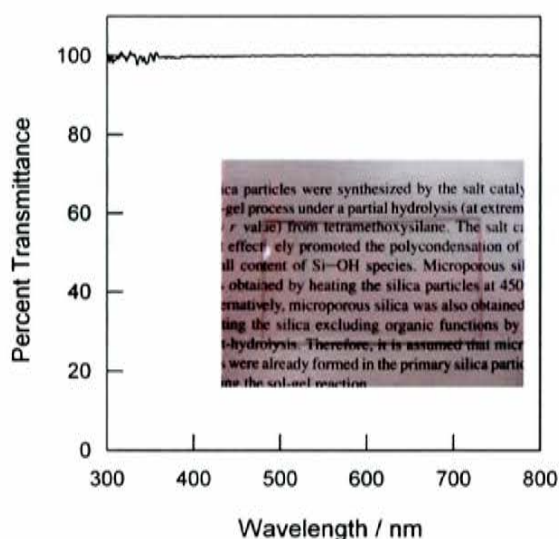

Figure 4.2. Optical transmission spectra of a superhydrophilic coating on a quartz substrate. The inset is a photograph of the superhydrophilic coatings on a quartz substrate.

The superhydrophilic coating was smooth in the presence of micropores. Figure 4.3 (a) shows an AFM topographical image of the coating on a highly smooth silicon substrate. A smooth silicon substrate was used instead of the PET substrate since the surface of the PET substrate is rough. A typical cross–sectional profile (Fig. 4.3 (b)) indicates a vertical interval within 3 nm. The roughness was only three percent of the thickness of the coating (100 nm). The roughness due to a micropore in the coating is visually imperceptible.
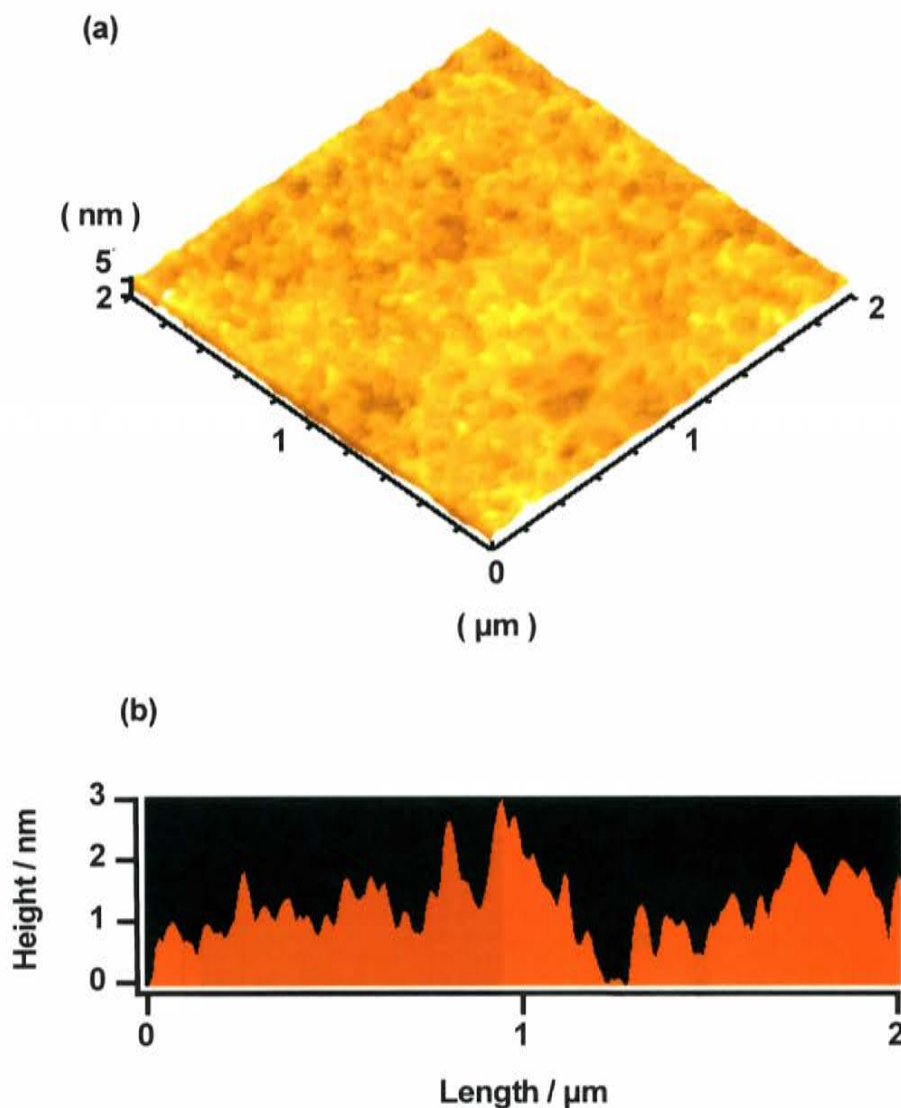
Figure 4.3. (a) An AFM topographical image of a superhydrophilic coating on a silicon substrate. (b) A typical cross–sectional profile. The thickness of the coatings is estimated to be 100 ± 2 nm.

The specific surface areas of dried bulk gel, which was prepared from coating sol, are shown in Table 4.1. Immersing silica in water at 80 °C increased the specific surface area of the silica (700 $m^2\ g^{-1}$) compared to that of the as-prepared one (410 $m^2\ g^{-1}$). The increase in the specific surface area was caused by the pore distribution change. Figure 4.4 shows the nitrogen adsorption–desorption isotherms for the as-prepared silica and two kinds of silica immersed in water. The isotherm is I type for all of the silica, which indicates that the high specific surface area of the silica is due to the microporous structure.[5] The pore size for the as-prepared silica has a narrow distribution and a mode diameter of the pore is less than 0.8 nm. Immersing a microporous silica in water at 80 °C expanded the mode diameter of the pore to 0.8 nm.
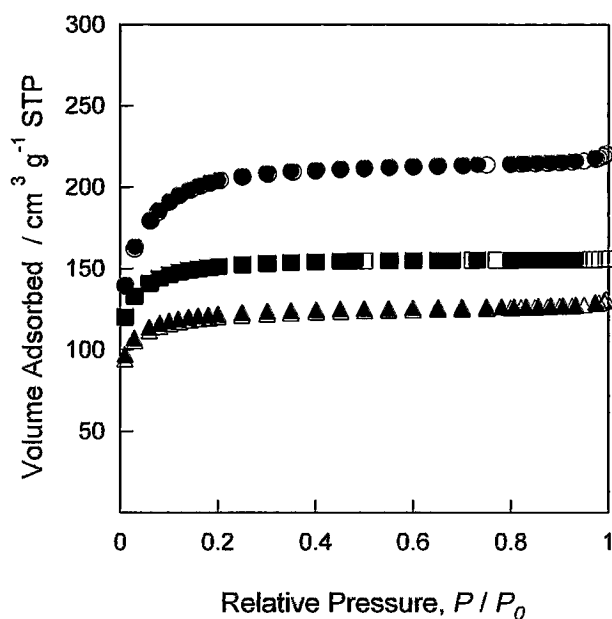

Figure. 4.4. Nitrogen adsorption (open) / desorption (solid) isotherms of the silica powders; (a) immersed in water at 80 °C for two hours, (b) immersed in water at 25 °C for two hours, and (c) as-prepared.

Hydrolysis of the remaining alkoxy groups proceeded by immersing the silica coating in water at 80 °C.

Figures 4.5 and 4.6 show the infrared spectra of the as–prepared coating and two kinds of coatings immersed in

water at 25 °C and 80 °C. Immersing the silica coating in water increased the absorptions at a broad band

centered near 3400 cm^{-1}, a small band at 1630 cm^{-1} and a sharp band at 950 cm^{-1} (Fig. 4.5). The broad band

centered near 3400 cm^{-1} is assigned to the hydrogen bonded SiO–H stretching vibrations (3200–3650 cm^{-1}),

hydrogen bonded water (3300–3500 cm^{-1}) and hydrogen bonded OH vibrations of alcohols (3300–3600 cm^{-1})

which are possibly of methanol, 2–ethoxyethanol and hydroxyacetone in the case of this study.[5-7] The small

band at 1630 cm^{-1} is assigned to the scissor bending vibration of the adsorbed molecular water, while the band

at 950 cm^{-1} is assigned to the Si–OH stretching of the terminal silanol groups.[6-8] An isolated SiO–H stretching

vibrations, which occurs at 3650–3800 cm^{-1},[6] is not detected in these spectra. This result indicates that most of

the silanol groups in these silica coatings are hydrogen bonded to water. The characteristic band of

hydroxyacetone, which is observed at 1715 cm^{-1}, was not detected in all of the spectra. On the other hand,

immersing the silica coating in water decreased the absorption bands at 2950 and 2850 cm^{-1} (Fig. 4.6). These

bands are assigned to the C–H stretching of the alkoxy groups.[9,10] The alkoxy groups remained in the

as–prepared coating. The reaction system for the preparation of the microporous silica involved only a molecule

of water per tetramethyl orthosilicate molecule to leave the alkoxy groups after hydrolysis and condensation.

The hydroxyl group increased whereas the alkoxy group decreased. Hydrolysis of the remaining alkoxy groups

to hydroxyl groups proceeded by immersing the silica coating in water. Absorption bands, which consist of a

shoulder at 1220 cm^{-1} and distinct peak at 1080 cm^{-1}, are slightly increased by immersing the silica coating in

water. These bands are assigned to the longitudinal optical (LO) mode and the transverse optical (TO) mode of

the asymmetric Si–O stretching vibration, respectively,[6,7] whereas the band at 800 cm^{-1}, the intensity of which

almost did not change when immersing in the water, is assigned to the symmetric Si–O–Si stretching or

vibrational modes of the ring structure.[11,12] The change in the Si–O bonds is not recognizable due to the small

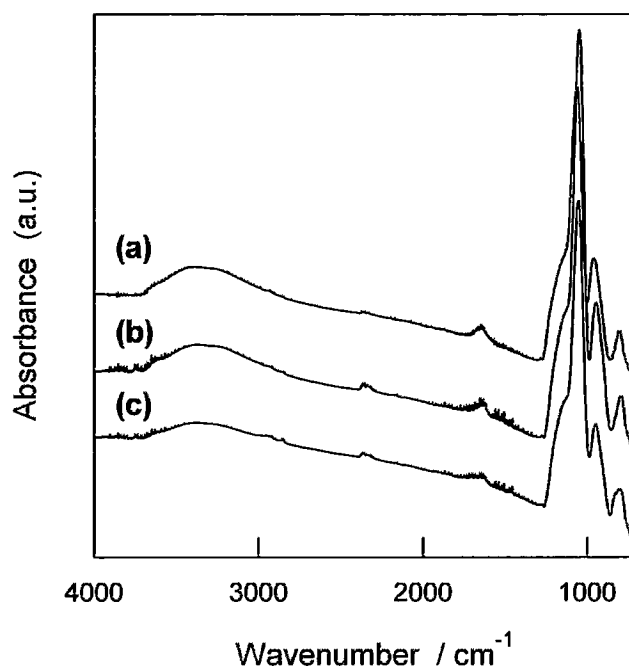rate of change in the initial quantity.

Figure 4.5. FT–IR spectra at 700–4000 nm of the silica coatings on a silicon substrate (a) immersed in water at 80 °C for two hours, (b) immersed in water at 25 °C for two hours, and (c) as–prepared.
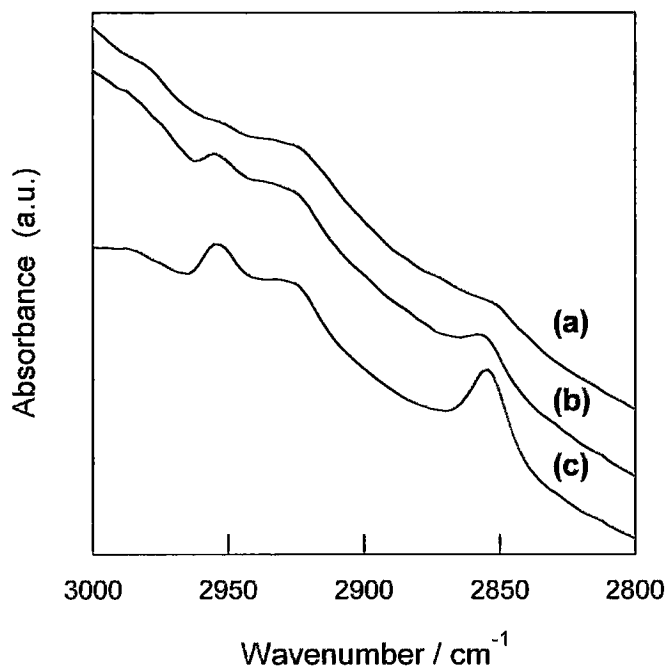

Figure 4.6. FT–IR spectra at 2800–3000 nm of the silica coatings on a silicon substrate (a) immersed in water at 80 °C for two hours, (b) immersed in water at 25 °C for two hours, and (c) as–prepared.

Immersing microporous silica in water at 80 °C facilitated the adsorption of water on the micropores of the silica. Based on the thermogravimetry, for the silica immersed in water at 80 °C, the mass decrease developed in two stages (Fig. 4.7 (a)): rapid elimination of the adsorbed water below 120 °C and gradual elimination of hydroxyl groups through dehydrating condensation over a wide range of temperatures. The amount of adsorbed water on the silica immersed in water at 80 °C is almost four times greater than that on the as-prepared silica. The hydrolysis of the remaining methoxy groups to hydroxy groups facilitated the adsorption of water on the micropores of the silica. The behavior of the mass decrease of the silica immersed in water at 25 °C was similar to that at 80 °C (Fig. 4.7 (b)). The amount of water adsorbed on the silica immersed in water at 25 °C is lower than that at 80 °C, which depended on a decrease in the surface area or the pore volume. Methoxy groups slightly remained after immersing the silica in water at 25 °C, while they were completely removed during the immersion at 80 °C. The elimination process of the as-prepared silica was more complicated (Fig. 4.7 (c)). Organic functional groups, such as methoxy groups, and high boiling point organic compounds, such as hydroxyacetone and 2-ethoxyethanol, remained in the as-prepared silica. The mass decreases were observed to occur in two steps: the decrease at 120–200 °C was attributed to the combustion of hydroxyacetone and 2-ethoxyethanol and the decrease at 200–300 °C was attributed to the combustion of the methoxy groups.

Immersing a silica coating in water increased the hardness of the coating. The pencil hardness of the coating immersed in water was 2H, while that of the as-prepared coating was 2B (Table 4.1). By immersing the silica coating in water, a silica network will develop by hydrolysis of the remaining alkoxy groups and subsequent condensation of the generated hydroxy groups. The hardnesses of the coatings were quite different between the as-prepared silica coating and the coating immersed in water, although the thicknesses of all the coatings were about 100 nm.

The superhydrophilicity was developed by immersion in water at 80 °C. The water contact angles, which were observed with a silica coating on a silicon substrate, are shown in Table 4.1. A drop of water immediately spreads over the coating immersed in water at 80 °C (Fig. 4.8 (a)), on which contact angle was 3°. The contact

angle on the coating immersed in water at 25 °C was 10° (Fig. 4.8 (b)), while the contact angle on the

as–prepared coating was 29° (Fig. 4.8 (c)). The hydrophilicity depended on the extent of the hydrolysis of the

methoxy groups. In contrast, the contact angle on a bare silicon substrate was 70° (Fig. 4.8 (d)).

Table 4.1. Immersion Effects on the Silica Coating

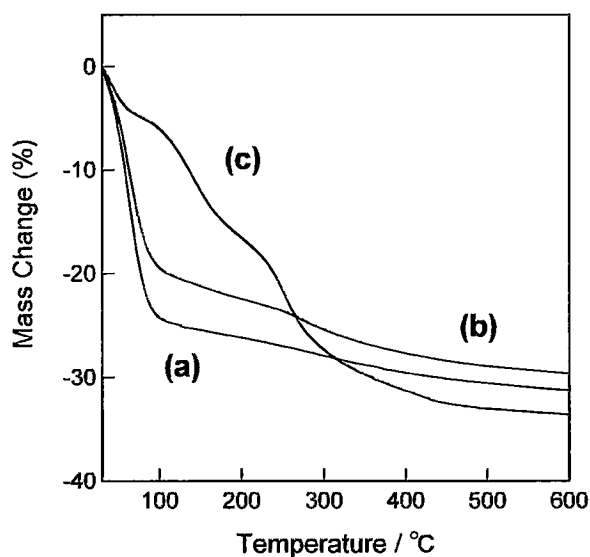| Immersing temperature (°C)	Film thickness (nm)	Specific surface area (m^2g^{-1})	Pencil hardness	Contact angle (°)
80	100	700	2H	3.4
25	100	510	2H	11.6
as–prepared[a]	105	410	2B	29.5

[a] The sample without immersing process.

Figure 4.7. Themo–gravimetry of the silicas (a) immersed in water at 80 °C for two hours, (b) immersed in water at 25 °C for two hours, and (c) as–prepared.

The superhydrophilic silica coating was prepared below 80 °C and thereby applied to the coating on a

polymer substrate such as PET (Fig. 4.1). The micropores of the silica coatings are filled with water due to the

adsorption of water. The presence of the infrared absorption band attributed to the hydrogen bonded O–H

vibrations and the mass decrease attributed to water elimination suggested water adsorption on the surface OH groups. The water drop is in contact with a rough surface which consists of the solid and the adsorbed water with which the micropore is filled.

The contact angle of water on the coating immersed in water at 25 °C, which has the remaining methoxy group, was 10°. The presence of the infrared absorption band attributed to the C–H vibrations suggested residual methoxy groups. The remaining methoxy group would decrease the adsorption of water. The TG data suggested that the amount of water adsorbed on the silica immersed in water at 25 °C is lower than that at 80 °C.
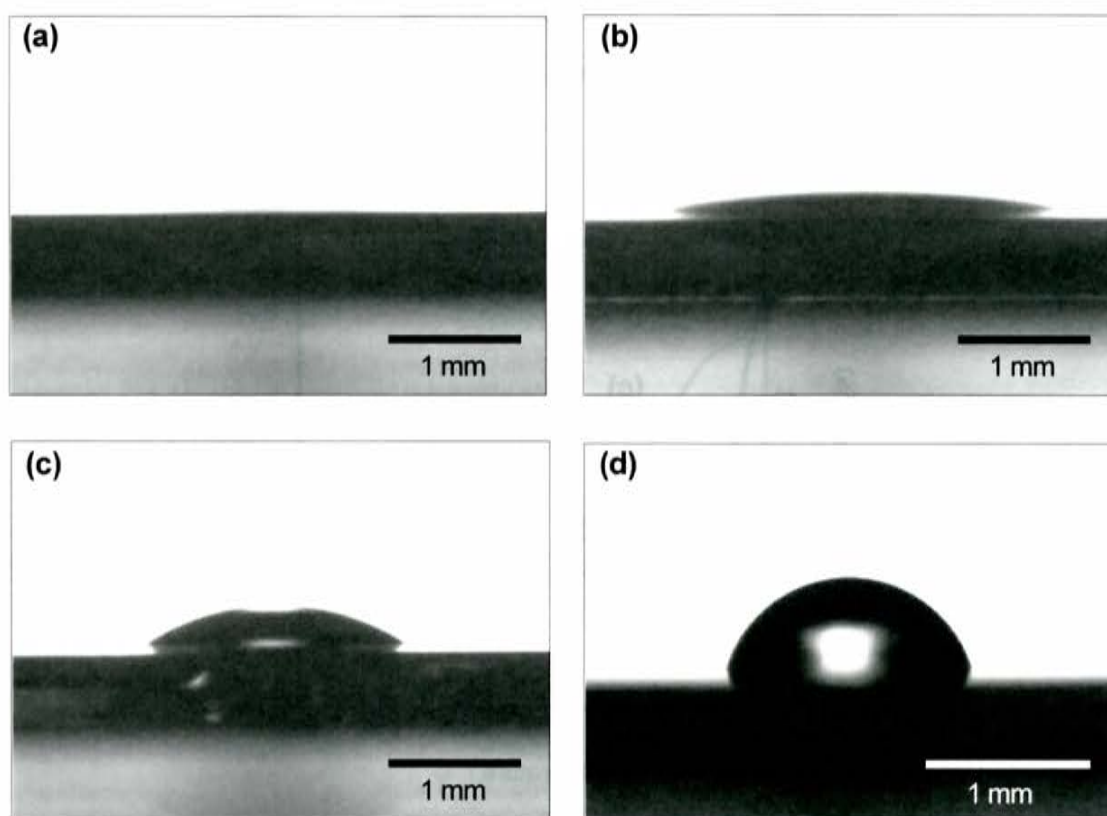

Figure 4.8. Water drops onto the silica coatings on a silicon substrate (a) immersed in water at 80 °C for two hours, (b) immersed in water at 25 °C for two hours, and (c) as–prepared. (d) Semispherical drop of water on a bare silicon substrate.

Hydroxyacetone as a non–ionic catalyst allows the preparation of the microporous silica precursor from tetramethyorthosilicate under neutral condition. As before, the microporous silica precursor has been hardly obtained and then the porosity is controlled by slowing the rate of evaporation as compared to the rate of condensation. In fact, the microporous bulk gel is readily obtained by the slow drying.[5,13] On the other hand, this work controlled the porosity by accelerating the rate of the catalytic hydrolysis with hydroxyacetone.

The pore size distribution was narrow and most of the pores are smaller than 1.5 nm in diameter. The pore size was so small that an apparently smooth surface was obtained.

Immersing the silica coating in water is an important process for removing not only the methoxy group, but also hydroxyacetone as a non–ionic catalyst. Accessibility to the back of the coating depended on the immersion temperature. The hardness of the coating immersed in water at 25 °C is the same as that at 80 °C. Therefore, hydrolysis of the methoxy groups and the subsequent condensation of the hydroxyl groups would have already occurred at the surface layer of the coating. An increase in hardness of the silica coating immersed in water was also reported by Matsuda et al.[14]

4.4. Conclusions

A transparent smooth superhydrophilic microporous silica coating on a PET substrate was developed by the hydrolysis of the remaining methoxy groups to hydroxy groups and the adsorption of water on the inner surface of the micropores at 80 °C. After the drying of the adsorbed water, the superhydrophilicity can be restored by the adsorption of water at a normal humidity and room temperature. Immersing the coating in water is an important process for removing not only the methoxy group but also the hydroxyacetone that act as hydrophobic species while remaining in the coating.

References

1. Wang, R. Hashimoto, K. Fujishima, A. Chikuni, M. Kojima, E. Kitamura, A. Shimohigoshi, M.; Watanabe, T. Nature 1997, 388, 431.

2. Song, K. -C.; Park, J. -K.; Kang, H. -U.; Kim, S. -H. J. Sol–Gel Sci. Technol. 2003, 27, 53.

3. Bico, J.; Thiele, U.; Quéré, D. Colloids Surf. A 2002, 206, 41.

4. Cebesi, F. Ç.; Wu, Z.; Zhai, L.; Cohen, R. E.; Rubner, M. F. Langmuir 2006, 22, 2856.

5. Brinker, C. J.; Scherer, G. W. In Sol-Gel Science, The Physics and Chemistry of Sol–Gel Processing; Academic Press: New York, 1990, pp. 818.

6. Innocenzi, P. J. Non-Cryst Solids 2003, 316, 309.

7. Zecchina, A.; Bordiga, S.; Spoto, G.; Marchese, L.; Petrini, G.; Leofanti, G.; Padovan, M. J. Phys. Chem. 1992, 96, 4991.

8. Almeida, R. M.; Pantano, C. G. J. Appl. Phys. 1990, 68, 4225.

9. Ou, D. L.; Seddon, A. B. J. Non-Cryst. Solids 1997, 210, 187.

10. Méndez–Vivar, J.; Mendoza–Bandala, A. J. Non-Cryst. Solids 2000, 261, 127.

11. Brinker, C. J.; Scherer, G. W. In Sol-Gel Science, The Physics and Chemistry of Sol–Gel Processing; Academic Press: New York, 1990, pp. 541.

12. Nocuń, M.; Handke, M. J. Mol. Struct. 2001, 596, 139.

13. Frye, G. C.; Ricco, A. J.; Martin, S. J.; Brinker, C. J. Better Ceramics Through Chemistry III, Ed. by Brinker, C. J.; Clark, D. E.; Ulrich, D. R. Mat. Res. Soc., Pittsburgh, Pa., 1988, pp. 349.

14. Matsuda, A.; Matoda, T.; Kogure, T.; Tadanaga, K.; Minami, T.; Tatsumisago, M. J. Sol–Gel Sci. Technol. 2003, 27, 61.

CHAPTER 5

Synthesis of Low-Fractal Dimension

Titanium Oxide Polymers

5.1. Introduction

As demonstrated in the previous chapters, precursor polymers of inorganic materials are synthesized by

the sol–gel technique through the hydrolysis and polycondensation reactions of metal alkoxides, and inorganic

materials are fabricated via drying and heating processes of the precursor sols comprising inorganic oxide

polymers. A metal oxide thin film can be obtained by dip or spin coating of sols produced from a

reaction–controlled sol–gel process.[1-4]

Similar to silica materials, titanium oxide thin films have often been produced by wet processes, e.g., dip or spin coating of liquid precursors.[5-10] In particular, when targeting the use as a functional optical coating, dispersions of titanium oxide fine particles (nanoparticle) that can suppress light scattering are often used to attain high transparency of the thin films. Titanium oxides are primarily high refractive index materials, and thereby expected to be used as high refractive index coating.[8-11] Due to inevitable aperture formation between the particles, however, the refractive index of the titanium oxide coating is often lower than expected from high values of crystalline titanium oxides. As for silicon dioxide (silica), low–fractal dimension polymer–like liquid precursors, instead of particle–like (high–fractal dimension) ones, were successfully synthesized aimed at densifying a solid matrix of thin films.[5] In contrast, because of eccentric reactivity of titanium alkoxides, it has generally been difficult for titanium oxides to achieve such low–fractal dimension polymeric structure; a sol–gel reaction of titanium alkoxides easily produces particle–like aggregates, leading to immediate precipitation of titanium oxide particles.[5] According to Murakami et al., such inherent difficulty comes essentially from the 'slow' polycondensation reaction of titanium oxides in a sol–gel reaction system.[12]

A number of techniques aimed at producing low–fractal dimension titanium oxide polymeric precursors were attempted based on a sol–gel technique. One possible way is to use organic ligands like acetylacetone to restrict the production of hydrolyzed sites by stabilizing titanium alkoxides.[13,14] The coordinated organic ligands are not easily removed from the grown polymers; calcination may influence optical properties of the solid films because upon thermal decomposition of organic ligands, the low–fractal dimension titanium oxide network is to be destroyed, which is in some cases accompanied by partial crystallization. Alternative approach was to use strongly acidic solution codition,[15,16] which allowed to generate weakly–branched titanium oxide polymers (d_f < 2). However, due to a slow polycondensation reaction, this method took a very long time (> 1 month) before the low–fractal dimension polymers were grown, and thus would not be very practical.

To realize the efficient fabrication of the low–fractal dimension titanium oxide polymers, one needs to introduce a renovated reaction–controlled sol–gel process that can enhance the polycondensation rate of

titanium alkoxides to condense partially hydrolyzed reactive species rapidly, while suppressing the number of hydrolyzed sites. In this chapter, the time–evolution of titanium oxide polymers in the precursor solution derived via the catalytic sol–gel process with the hydrazine monohydrochloride catalyst was investigated by mean of time-resolved small angle X-ray scattering (Tr–SAXS). The present catalytic sol–gel process enables rapid production (within several hours) of a transparent sol or gel with no organic ligand.[17,18] SAXS is certainly a suitable technique to confirm the generation of the only weakly–branched polymeric objects because one can easily distinguish such low–fractal dimension characteristics form those of high fractal dimension or globular particle–like objects ($d_f \approx 3$) owing to their markedly different scattering behavior. Furthermore, a set of the structural parameters describing the geometry of the polymer chains, e.g., the radius of gyration reflecting the extent of the spatial distribution of the polymer chains, the fractal dimension corresponding to the internal self–similarity, the correlation length often referred to as the mesh size of the transient polymer network, and the persistent length related to the internal flexibility of the polymer chains, can be evaluated from the measured scattering intensity. As shown in the following section, data unambiguously demonstrate successful rapid synthesis of the weakly–branched titanium oxide polymers.

5.2. Experimental Section

5.2.1. Preparation of titanium oxide precursor solutions

Titanium tetra-n-butoxide (TTBO, Ti(OC$_4$H$_9$)$_4$ > 97 %, Kanto Chemical, Japan) was dissolved in 2-propanol (IPA, C$_3$H$_7$OH > 99.5 %, Wako Pure Chemical Industries, Japan) under a nitrogen gas atmosphere. A solution of hydrazine monohydrochloride (H$_2$N-NH$_2$ H Cl > 98 %, Tokyo Chemical Industry, Japan) in distilled water was dissolved in IPA. These solutions were slowly mixed at 0 °C to avoid generation and sequential precipitation of TiO$_2$ particles. The molar ratio in the titanium oxide precursor solution, TTBO : IPA : [H$_2$N-NH$_3$]$^+$ Cl$^-$: H$_2$O was adjusted to 1 : 20.95 : 0.04 : 2.5, resulting in the concentration of TTBO of 0.5 mol L^{-1}.

5.2.2. Small angle X-ray scattering (SAXS) experiments

Small Angle X-ray Scattering (SAXS) experiments were carried out on the precursor solutions, in which a SAXSess camera (Anton Paar GmbH, Graz, Austria) attached to a sealed tube anode X-ray generator (GE Inspection Technologies, Germany) was operated at 40 kV and 50 mA. A Göbel mirror and a block collimator provided a focused monochromatic X-ray beam of Cu Kα radiation (λ = 0.1542 nm). Two-dimensional scattering patterns recorded on an imaging-plate (IP) detector (a Cyclone, Perkin-Elmer) were integrated into to one–dimensional scattering intensities, $I(q)$, as a function of the magnitude of the scattering vector q = $(4\pi/\lambda)\sin(\theta/2)$, where θ is the total scattering angle. All $I(q)$ data were corrected for the background scattering from a capillary and solvents, and the absolute intensity calibration was made using water as a secondary standard.[19] A model-independent collimation correction (desmearing) procedure was made via an indirect Fourier transformation (IFT) routine.[20,21] All fitting and fractal analyses were performed on the collimation corrected SAXS intensities.

5.2.3. Viscometry

Viscosity of the precursor solutions was measured by a ViscoMate VM-1A viscometer (CBC, Tokyo, Japan) at 20 °C. Specific viscosity, η_{sp}, was determined as a function of reaction time referring to η_{sp} = (η – $\eta_s)/\eta_s$, where η and η_s are the viscosities of the precursor solution and the solvent, respectively.

5.3. Results and Discussion

The titanium oxide precursor solutions prepared via the hydrazine monohydrochloride–assisted catalytic sol–gel process were transparent without any precipitating particulate formation, whereas whitish precipitates were immediately formed in a solution without the catalyst, as shown in Fig.5.1.

The time evolution of the static structures of the titanium oxide precursor solutions was evaluated by means of time–resolved SAXS (Tr–SAXS).[22] Figure 5.2 shows the collimation–corrected SAXS intensities,

$I(q)$, of the titanium oxide precursor solutions on absolute scale, in which all $I(q)$ curves are given in a double-logarithmic plot as a function of the reaction time in 15 min $< t < 4.5$ h.

A pronounced increase of $I(q)$ with the reaction time provides the evidence for the growth of the titanium oxide polymers in the precursor solutions. $I(q)$ in the low-q regime exhibited Guinier behavior reflecting the overall geometry of the polymers, as described by a Guinier equation.

$$I(q) = I(0) \exp\left[-\frac{R_g^{\,2} q^2}{3} \right] \qquad (5.1)$$

where R_g is the radius of gyration. R_g was evaluated by applying the Guinier plot, i.e., ln $I(q)$ versus q^2, in the Guinier regime $qR_g < 1$. Figure 5.3 (A) shows the extrapolated forward intensities to zero scattering vector, $I(q \to 0)$, and the radius of gyration, R_g, of the precursor solutions. The change in the specific viscosity of the precursor solution with reaction time is shown in Fig. 5.3 (B). It is generally expected that in a polymerization experiment, a SAXS intensity should remain nearly constant until the size of aggregates and their number density are large enough to scatter X-rays to be detected. Accordingly, when an induction time for the intensity rise is observed, this appears to involve the induction time for nucleation, the actual nucleation period, and the period for the aggregate growth up to a certain size that can be detected by SAXS experiments. Indeed, the SAXS study on the silica polymer growth in sol–gel derived solution (shown in Chapter 2) clearly indicated the existence of an induction period before the onset of the intensity rise. However, an almost immediate increase of the forward intensity was observed for the present titanium oxide precursor system after the preparation of the solution. This means that an induction period for the titanium oxide polymer growth, even if it exists, was too short to be detected within the time resolution of this Tr–SAXS experiments. $I(q \to 0)$ reached approximately 1.2 cm^{-1} within 15 minutes, which was about 30 times greater intensity than the solvent scattering (ca. 0.04 cm^{-1}). High specific viscosity, $\eta_{sp} \approx 1.9$, in spite of short reaction time of 15 minutes also suggests the short induction period for the polymer growth (Fig. 5.3 (B)).
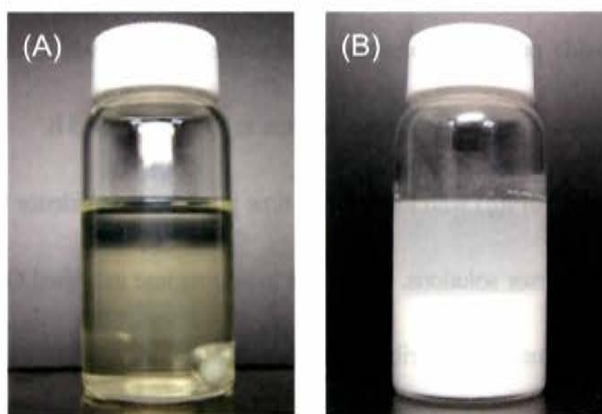
Figure 5.1. The liquid titanium oxide precursors derived from TTBO (A) with and (B) without the hydrazine monohydrochloride catalyst. The molar ratio of water, IPA, and TTBO was identical in (A) and (B). Note that a white object visible at the bottom of the solution (A) is a magnetic stirring bar. The solution in itself is transparent and contains no precipitation at all.
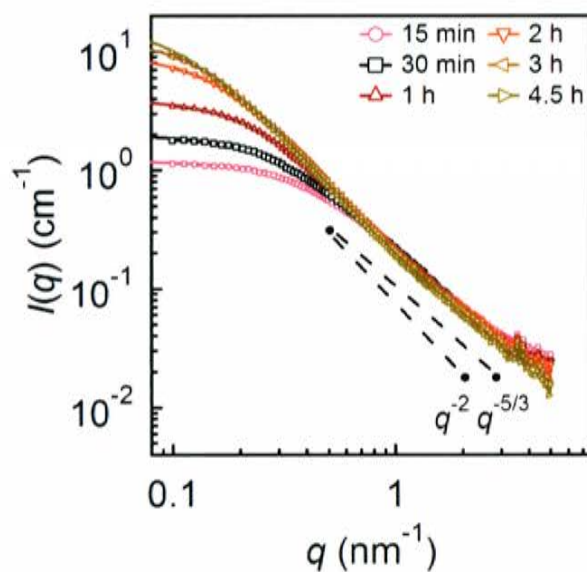

Figure 5.2. Variations of the SAXS intensities, $I(q)$, for the liquid titanium oxide precursors on absolute scale as a function of the reaction time, t, in a double-logarithmic plot. The dashed lines represents the $q^{-5/3}$ and q^{-2} slope to highlight the feature of $I(q)$ in the intermediate–q regime, showing fractal behavior.
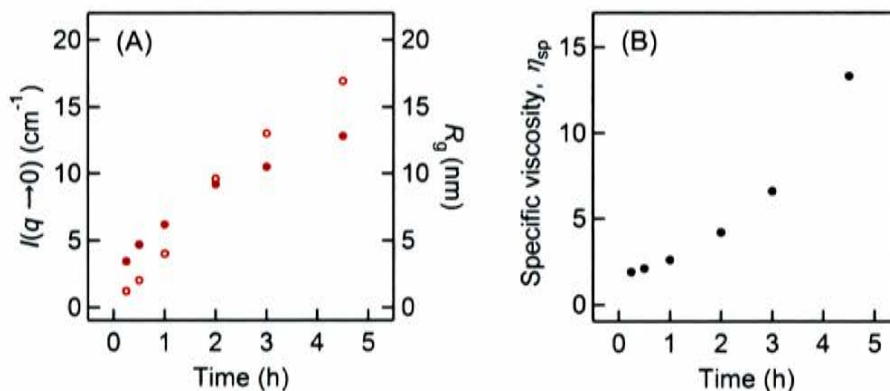
Figure 5.3. The structural evolution of the titanium oxide polymeric precursors as obtained by SAXS and viscometry. (A) The extrapolated forward intensities to zero scattering vector, $I(q{\rightarrow}0)$, (open circles) and the radius of gyration, R_g, (filled circles) as a function of the reaction time. (B) Changes in specific viscosity of the precursor solution with the reaction time.

For further quantitative description of the polymeric structure of the titanium oxide aggregates formed in the precursor solutions, the shape of the scattering curves were attempted to evaluate. SAXS can efficiently distinguish a linear polymer and a globular particle thanks to their markedly different scattering behavior.[7] The scattering function for a polymer is governed by the structure function, $S_{poly}(q)$, which is given by Fourier transformation of the monomer-monomer pair-correlation function, $g(r)$[23]

$$I(q) \propto S_{poly}(q) = 4\pi\langle c_m\rangle \int_0^\infty [g(r)-1]r^2 \frac{\sin qr}{qr} dr \quad (5.2)$$

where c_m is the averaged monomer concentration. On the one hand, as for a dilute colloidal dispersion, the scattering intensity $I(q)$ is given by Fourier transformation of the pair-distance distribution function, $p(r)$, as[22]

$$I(q) = 4\pi \int_0^\infty p(r)\frac{\sin qr}{qr} dr \quad (5.3)$$

where $p(r)$ corresponds to the convolution square of the electron density fluctuations, $\Delta\rho(r)$, in a colloidal particle

$$p(r) \equiv \Delta\tilde{\rho}^2(r)r^2 = \left\langle \int_{-\infty}^\infty \Delta\rho(r_1)\Delta\rho(r_1-r)dr_1 \right\rangle r^2 \quad (5.4)$$

Figure 5.4 compares typical scattering behavior of a polymer and a colloidal particle showing simulated scattering functions for a polymer in solution having the internal fractal dimension $d_f = 2$, the correlation length $\xi = 5.0$ nm, and persistent length $l_{ps} \approx 1.5$ nm and for polydisperse hardspheres having an averaged radius of 3.6 nm with a 0.4 nm standard deviation. A Kratky plot, $q^2 I(q)$ versus q, is an instructive expression to visualize a fractal nature of a coil polymer ($d_f \approx 2$), which appears as a plateau in the intermediate q–range (Fig. 5.3(A)). As highlighted by arrows, a crossover from the coil-like [$I(q) \propto q^{-2}$] to rod-like [$I(q) \propto q^{-1}$] scattering can also be monitored if the measurement covers sufficiently high-q region.[23] If a Kratky plot is applied to a colloidal particle, it gives a low-q local maximum and a rapid decrease at high-q (Fig. 5.3(B)).
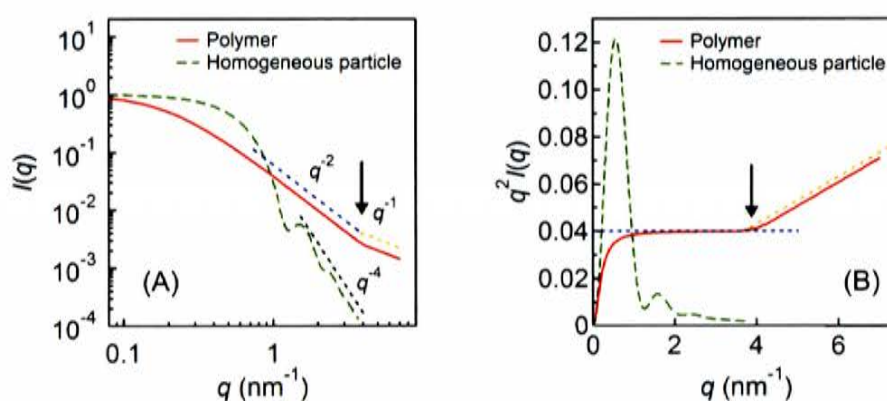

Figure 5.4. Comparison of the scattering behavior of a polymer (red) and a colloidal particle (green). (A) The simulated scattering intensities, $I(q)$, of a polymer solution (the fractal dimension $d_f = 2$, the correlation length $\xi = 5.0$ nm, and persistent length $l_{ps} \approx 1.5$ nm) and a dilute colloidal dispersion (polydisperse hardspheres having homogeneous scattering length density distribution with an averaged radius of 3.6 nm and a 0.4 nm standard deviation), and (B) their Kratky plots, $q^2 I(q)$ versus q. $d_f = 2$ of a linear polymer is highlighted by a plateau in the Kratky plot. Arrows indicate the crossover from the coil-like [$I(q) \propto q^{-2}$] to the rod-like [$I(q) \propto q^{-1}$] scattering.

The power–law behavior was observed for the titanium oxide precursor solutions in the intermediate–q range ($0.7 \leq q/\text{nm}^{-1} \leq 3$), indicating the emergence of internal self-similarity, i.e., fractal nature.[23] The fractal dimension, d_f, directly shows up as the slope of $I(q)$, as given by the following formula

$$I(q) \propto q^{-d_f} \qquad (5.5)$$

The observed $q^{-5/3}$ slope of $I(q)$ in $0.7 \leq q/\text{nm}^{-1} \leq 3$ gives $d_f \approx 5/3$, which is identical with d_f of an expanded

chain with excluded volume, instead of $d_f \approx 2$ for a Gaussian polymer. In the previous studies, the steeper slope

of $I(q)$ was observed for titanium oxide precursors produced by a conventional sol–gel technique because of

their highly-branched structures, yielding $d_f \approx 3$.[5,15]

Neglecting notable high–q deviation, the experimental $I(q)$ can be approximated by the Ornstein-Zernike

(OZ) expression[24]

$$I(q) = \frac{I(0)}{1 + \xi^2 q^2} \qquad (5.6)$$

where ξ is the correlation length and $I(0)$ is the asymptotic zero–q intensity. ξ can be interpreted as the

mesh-size of the transient polymer network,[25] representing the length scale of the spatial correlation of density

fluctuations caused by a polymer chain.[23] The Fisher-Burford (FB) equation[26] with the fractal dimension $d_f \approx$

5/3

$$I(q) = \frac{I(0)}{\left[1 + \left(2R_{g,FB}^2 q^2 / 3d_f\right)\right]^{d_f/2}} \qquad (5.7)$$

gives a better description of the experimental $I(q)$ than the OZ equation in the fractal regime exhibiting $I(q) \propto$

$q^{-5/3}$, where $R_{g,FB}$ is the (apparent) radius of gyration. Note that the FB equation does not involve the correlation

length, ξ, explicitly, and $R_{g,FB}$ is not consistent with the actual radius of gyration determined with the Guinier

plot due to the systematic deviation of the FB curve from the data points in the Guinier regime ($qR_g < 1$).

Therefore, it is believed that despite notable high–q deviation of the experimental $I(q)$ from the OZ function, a

fitting analysis based on the OZ equation was sufficient to evaluate ξ.

Instead of a conventional Kratky plot, $q^2 I(q)$ versus q, a modified Kratky plot, $q^{5/3} I(q)$ versus q (Fig.

5.5(B)) was used to highlight the expanded chain–like nature of the titanium oxide polymeric aggregates. The

high–q plateau ($q^{5/3} I(q) \propto q^0$) in $q >$ ca. 0.7 nm^{-1} intuitively shows $d_f \approx 5/3$. The crossover from the expanded

coil-like [$I(q) \propto q^{-5/3}$] to the rod-like one [$I(q) \propto q^{-1}$] can clearly be seen in $q > 3$ nm^{-1} (Fig. 5.5 (C)). At relatively longer reaction times > 2 h, a low-q local maximum in $q < 1$ nm^{-1} emerged in the modified Kratky plot. Branching of polymer chains may impose a particle-like nature on the polymer chains. Indeed, star-branched polymers,[27] dendrimers,[28] nanoparticles comprising tightly crosslinked liner chain precursors,[29] and sol−gel derived high−fractal dimension silica aggregates show a local maximum in their Kratky plot, as globular particles do (in Chapter 2). This appears to indicate the partial branching of the polymeric structure, preserving internal fractal dimension of $d_f \approx 5/3$, which resembles the finding of Mackay et al.[29] despite fairly different systems.
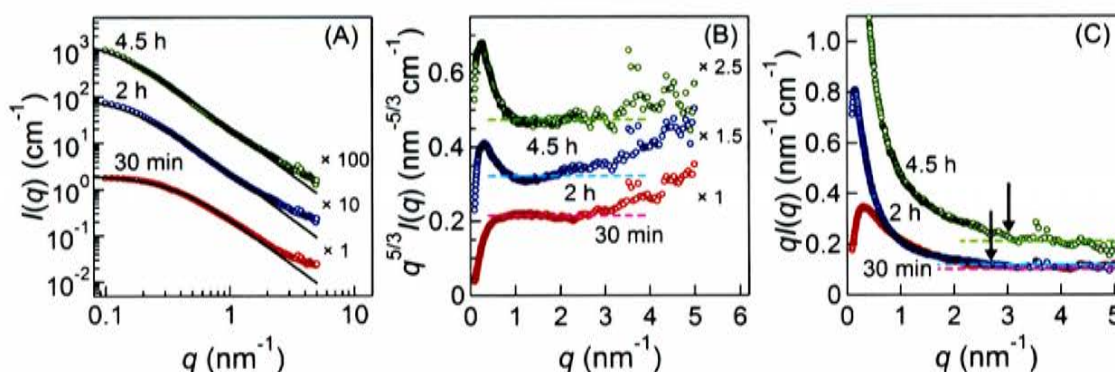

Figure 5.5. (A) SAXS intensities, $I(q)$, on absolute scale, (B) a modified Kratky plot, $q^{5/3}I(q)$ versus q, and (C) $qI(q)$ versus q, for the titanium oxide precursor solutions. Solid lines shown in a panel (A) represent the optimum fit curves based on the Ornstein−Zernike (OZ) equation. The plateaus indicated by dashed lines in panels (B) and (C) highlight the expanded chain−like ($I(q) \propto q^{-5/3}$) and the rod−like ($I(q) \propto q^{-1}$) scattering behavior in the individual q-regimes, respectively. All the data confirm the formation of the expanded chain−like polymeric aggregates having $d_f \approx 5/3$.

Figure 5.6 shows variation of ξ as a function of the reaction time as obtained by SAXS. It was observed that ξ was an increasing function of time, drawing an upwards convex curve. The data show that the mesh-size of transient polymer network of the titanium oxide liquid precursor was able to be treated as a tunable parameter controlled by the reaction time, while preserving a low fractal dimensionality ($d_f \approx 5/3$). This may also affect

the partial electron density of the optical solid materials produced from the present liquid precursor in future application.

The asymptotic zero–q intensity, $I(q\to0)$, gives a measure of molecular mass of a polymer chain in a dilute solution. In a semidilute solution as the titanium oxide precursor solution, this is no longer exact because the interference scattering between different chains also contributes to the forward scattering.[17,18,30] $I(q\to0)$ is used as a semi–quantitative measure of the apparent mass, M_w^{app}, of the titanium oxide polymers. Figure 5.7 shows $I(q\to0, t)$ plotted against R_g, which reveals the interplay of the apparent mass and the extent of spatial distribution of the polymer-like aggregates. Two solid lines shown in Fig. 5.7 represent the optimum fit curves under the assumption of $M_w^{app} \propto R_g^{\nu}$. There seem to exist two regimes of the polymer growth, i.e., the short time regime ($\nu \approx 5/3$) in $t < 1$ h, where $R_g < 5$ nm, and the long time one ($\nu \approx 2$) in $t > 1$ h, where $R_g > 5$ nm. It is believed that this finding is related to the emergence of the low-q maximum in the (modified) Guinier plot (Fig. 5.5(C)), implying the generation of branching at long reaction time ($t > 1$ h). Nevertheless, the exponents ν found to be in the range of $5/3 \le \nu \le 2$ again confirm the growth of the weakly–branched titanium oxide polymers.
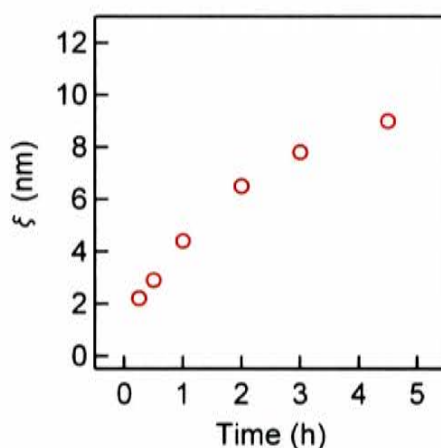

Figure 5.6. Variation of the correlation length, ξ, with the reaction time. ξ can be understood as the mesh-size of the transient polymer network.
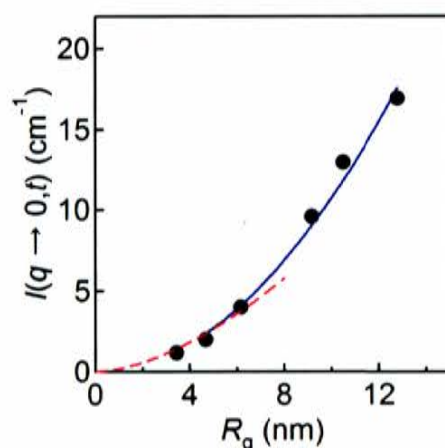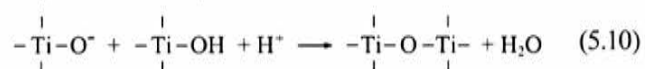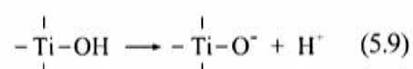
Figure 5.7. The extrapolated forward intensities to zero scattering vector, $I(q \to 0)$, plotted against R_g, revealing the interplay of the apparent mass and the spatial distribution of the titanium oxide polymers. The optimum fit curves given in the red broken line and blue solid line suggest the presence of two schemes of the polymer growth; $[I(q \to 0) \propto R_g^{5/3}]$ at short times of $t < 1$ h (red) and $[I(q \to 0) \propto R_g^2]$ in a long time regime of $t > 1$ h (blue).

In the light of the Tr–SAXS result which has unambiguously demonstrated the rapid production of the low–fractal dimension polymeric structure of the titanium oxides, the following reaction mechanisms and the role of the hydrazine monohydrochloride catalysts are figured out. In the sol–gel process, a metal oxide polymer is produced by hydrolysis and subsequent polycondensation reactions of metal alkoxides.[5] A partially hydrolyzed titanium alkoxide ($\equiv$Ti-OH) is generated by the hydrolysis of a titanium alkoxide

$$- \text{Ti-OR} + \text{H}_2\text{O} \longrightarrow - \text{Ti-OH} + \text{ROH} \quad (5.8)$$
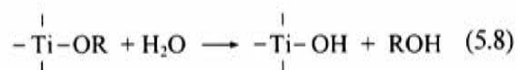
where OR denotes an alkoxy group and ROH is the corresponding alcohol. A dehydrative polycondensation reaction of two partially hydrolyzed titanium alkoxide species is given by the following two reaction formulas

$$- \text{Ti-OH} \longrightarrow - \text{Ti-O}^- + \text{H}^+ \quad (5.9)$$

$$- \text{Ti-O}^- + - \text{Ti-OH} + \text{H}^+ \longrightarrow - \text{Ti-O-Ti-} + \text{H}_2\text{O} \quad (5.10)$$

Eq.(5.9) expresses deprotonation while Eq.(5.10) refers to dehydroxylation, which are generally accelerated by a base catalyst and an acid catalyst, respectively. Therefore, in order to accelerate the overall polycondensation, both a base catalyst and a acid catalyst are expected to be simultaneously required.[12]

Hydrazine monohydrochloride, $[H_2N-NH_3]^+$ Cl^-, used in this study dissociates in solution and attains an equilibrium state of a hydrazinium ion and hydrazine

$$[H_2N-NH_3]^+ \rightleftharpoons H_2N-NH_2 + H^+ \qquad (5.11)$$
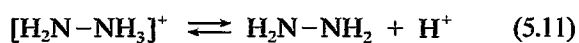
That is to say, a hydrazinium ion, $[H_2N-NH_3]^+$, releases a proton acting as an acid and is decomposed into a hydrazine, H_2N-NH_2, while a hydrazine accepts a proton serving as a base and forms a hydrazinium ion.[17] If such an equilibrium state exists in the reacting system of the titanium oxides, a hydrazine promotes the deprotonation given in Eq.(5.9) as a base catalyst and a hydrazinium ion does the dehydroxylation formulated by Eq.(5.10) as an acid catalysts. Thereby, the overall dehydrative polycondensation reaction of the partially hydrolyzed titanium alkoxides is to be efficiently accelerated by hydrazine monohydrochloride, which elaborately serves as an acid-base pair catalyst.[17,18]

5.4. Conclusions

The Tr–SAXS study has demonstrated the successful rapid synthesis of the low-dimensional polymeric titanium oxide precursors with the help of the catalytic sol–gel process using the hydrazine monohydrochloride catalyst. It was confirmed that the generated titanium oxide polymers possess the expanded chain-like fractal architecture ($d_f \approx 5/3$) with local rod–like structure. This synthetic technique is shown to be advantageous over the previously attempted sol–gel processes aimed at producing a low–fractal dimensional titanium oxide polymer; without any organic ligand to enhance the stability of titanium alkoxides, this achieves drastically faster growth (within hours) of the low–fractal dimension titanium oxide polymers than the existing approach that used a strongly acidic solution condition (ca. 1 month).

The catalytic sol–gel technique is able to treat the mesh-size of the transient polymer network of the titanium oxide liquid precursor as a tunable parameter controlled by the reaction time, while preserving a low fractal dimension ($d_f \approx 5/3$). This may also offer a route to controlling the partial electron density of the optical solid materials fabricated from the present liquid precursor in future material application. The next chapter will

show formation of dense titania solids with high refractive indices from the low fractal dimension titanium

oxide polymers.

References

1. Caro, J.; Noack, M.; Kölsch, P. Schäfer, R. Micropore Mesopore Mater. 2000, 38, 3.

2. Hu, L. L.; Yoko, T.; Kozuka, H.; Sakka, S. Thin Solid Films 1992, 219, 18.

3. Stathatos, E.; Lianos, P.; Tsakiroglou, C. Langmuir 2004, 20, 9103.

4. Sheng, Y.; Liang, L.; Xu, Y.; Wu, D.; Sun, Y. Opt. Mater. 2008, 30, 1310.

5. Brinker, C. J.; Scherer, G. W. In S*ol−gel Science, The Physics and Chemistry of Sol−gel Processing*, Academic Press: New York, 1990.

6. Bange, K.; Ottermann, C. R.; Anderson, O.; Jeschkowski, U.; Laube, M.; Feile, R. Thin Solid Films 1991, 197, 279.

7. Orignac, X.; Barbier, D.; Du, X. M.; Almeida, R. M. Appl. Phys. Lett. 1996, 69, 895.

8. Mosaddeq-ur-Rahman, M.; Yu, G.; Soda, T.; Jimbo, T.; Ebisu, H. Umeno, M. J. Appl. Phys. 2000, 88, 4634.

9. Wang, Z. C.; Helmersson, U.; Kall, P. O. Thin Solid Films 2002, 405, 50.

10. Hou, Y. Q.; Zhuang, D. M.; Zhang, G.; Zhao, M.; Wu, M. S. Appl. Surf. Sci. 2003, 218, 97.

11. Martinu, L.; Poitras, D. J. Vac. Sci. Technol. A 2000, 18, 2619.

12. Murakami, Y.; Matsumoto, T.; Takasu, Y. J. Phys. Chem. B 1999, 103, 1836.

13. Blanchard, J.; Ribot, F.; Sanchez, C.; Bellot, P. V.; Trokiner, A. J. Non-Cryst. Solids 2000, 265, 83.

14. Hanley, T. L.; Luca, V.; Pickering, I.; Howe, R. F. J. Phys. Chem. B 2002, 106, 1153.

15. Kallala, M.; Sanchez, C.; Cabane, B. Phys. Rev. B 1993, 48, 3692.

16. Kallala, M.; Sanchez, C.; Cabane, B. J. Non-Cryst. Solids 1992, 147&148, 189.

17. Murakami, Y.; Matsumoto, T.; Watanabe, Y.; Takasu, T. Trans. Mater. Res. Soc. Jpn. 1999, 24, 425.

18. Matsumoto, T.; Murakami, Y.; Takasu, Y. Chem. Lett. 2000, 4, 348.

19. Orthaber, D.; Bergmann, A.; Glatter, O. J. Appl. Cryst. 2000, 33, 218.

20. Glatter, O. J. Appl. Crystallogr. 1977, 10, 415.

21. Glatter, O. Acta Phys. Austriaca 1977, 47, 83.

22. Glatter, O.; Kratky, O. Small-Angle X-Ray Scattering, Academic, London, 1982.

23. Strobl, G. R. The Physics of Polymers: Concepts for Understanding Their Structures and Behavior, 3rd ed., Springer, Berlin, 2007.

24. Ornstein, L. S.; Zernike, F. Proc. Acad. Sci. Amsterdam 1914, 17, 793.

25. Pedersen, J. S.; Schurtenberger P. J. Polym. Sci., Part B: Polym. Phys. 2004, 42, 3081.

26. Fisher, M. E., Burford, R. J. Phys. Rev. 1967, 156, 583.

27. Toporowski P. M.; Roovers, J. E. L. Macromolecules 1978, 11, 365.

28. Tande, B. M.; Wagner, N. J.; Mackay, M. E.; Hawker, C. J.; Jeong, M. Macromolecules 2001, 34, 8580.

29. Mackay, M. E.; Dao T. T.; Tuteja, A.; Ho D. L.; Horn V. H.; Kim, H-C.; Hawker, C. J. Nature materials 2003, 2, 762.

30. Pedersen, J.S.; Schurtenberger P. Macromolecules 1996, 29, 7602.

CHAPTER 6

Fabrication of High Refractive Index Amorphous

Dense Titanium Oxide Thin Films

6.1. Introduction

High refractive index films have widely been used for diverse optical devices, such as anti-reflective glass,

planar waveguides, dielectric multilayer mirrors, and interference filters.[1-9] Titanium dioxides (TiO_2) are among

promising candidates for optically–functionalized films that are transparent in the visible light region and

simultaneously exhibit high refractive indices, n. It is known that crystalline TiO_2 shows a greater n value than

amorphous TiO_2, as anatase and rutile crystal forms exhibit $n = 2.54$ and 2.75 at $\lambda = 550$ nm, respectively.[10]

Nevertheless, amorphous TiO_2 is still preferable for optical films to suppress multiple light scattering[10] because

the growth of crystalline TiO_2 is accompanied by the creation of inhomogeneous grains or particles having various anisotropic microcrystals, which induces birefringence of the films. Additionally, when plastic substrates are needed to use, crystalline TiO_2 are unfavorable because of its photocatalytic activity that may decompose the substrates.

In order to increase the refractive indices of amorphous TiO_2 films, dense films containing a reduced amount of air must be synthesized by suitable techniques. Various vacuum techniques of physical vapor deposition[10-18] have actively been studied to produce high–refractive index amorphous TiO_2 thin films. These vacuum processes yielded a dense amorphous film having a high refractive index ($n > 2.0$).[12-17] However, evaporation sources or a target were to be placed at a short distance (< 100 mm) from a substrate. This exposes the substrate to heat radiation and high temperatures ($> 100°C$), which inevitably causes damage to the substrate.[11,12,14,16] This fact discourages use of plastic substrates despite their number of advantages, e.g., flexibility, workability, and light weight. For example, a commonly-used plastic substrate like poly(methyl methacrylate) (PMMA) have such low heat-resistance that the films need to be fabricated at temperatures below 80°C. Attempts to protect the substrate against heat radiation by increasing the target-to-substrate distance resulted in reduced film density.[13,14] Thus, it has been so far difficult to increase the refractive index of amorphous TiO_2 thin films without thermal damage to the substrates.

An alternative deposition method may be spin or dip coating of the solution prepared via the sol–gel process.[19-29] Resulting films are formed at room temperature under atmospheric pressure. When the use of plastic substrates is targeted, such mild and moderate condition should be useful. As for polymeric precursors, they are synthesized from hydrolysis and polymerization reactions of titanium alkoxides. Packing density of the TiO_2 films depends on primary conformation of the precursor polymers in the coating solution, i.e., either a low–fractal dimension (weakly–branched) structure or high–dimensional (highly–branched) one.[30] The weakly-branched polymeric precursors are expected to provide a denser film, while the highly-branched

precursors generally leading to globular particle—like aggregates may create void spaces in the product film due to their apertures.

Weakly–branched (low–fractal dimension) titanium oxide polymers were synthesized by using organic ligands to retard the hydrolysis and polymerization reaction rates or by accelerating the polymerization reaction.[30] Rantala et al. fabricated amorphous TiO_2 film with $n = 1.81$ (at $\lambda = 632.8$ nm) using methacrylic acid as an organic ligand at 85°C.[26] However, the use of organic ligands prevented the TiO_2 film from being densified because of the organic residue. The film fabricated from these precursors involved many apertures filled with air, and as a result, the refractive index of the film did not attain a sufficiently high value. Alternatively, the polymerization reaction was accelerated by high concentration alkoxide. The rate of polymerization was proportional to the square of the hydrolyzed alkoxide concentration whereas that of hydrolysis was to the alkoxide and water concentration. Kuwabara et al. studied a high concentration sol–gel process, in which they produced transparent solutions.[21,31] Although monolithic denser films can be produced from high concentration solutions, the process needed an organic additive, such as 2-methoxymethanol, to prevent rapid hydrolysis.

In this chapter, an amorphous dense TiO_2 film with a high refractive index is tried to fabricate below 60°C, overcoming all abovementioned issues revealed in previous studies, i.e., creation of void space or inhomogeneous grains, high heating temperature, and side effects of an organic residue. As also shown in Chapter 5, the salt catalyst is expected to increase the polymerization rate in the sol–gel process compared to that of hydrolysis,[32] which helps produce a transparent sol or gel exhibiting low light scattering.[33,34] The coating solution was prepared via a catalytic sol–gel process using hydrazine monohydrochloride, which involved accelerated polymerization of hydrolyzed titanium alkoxide. Small angle X-ray scattering (SAXS) confirmed the formation of an expanded polymer chain—like titanium oxide aggregates ($d_f \approx 5/3$) having microscopic transient mesh size (2–3 nm) in the precursors. A successful production of a high refractive index amorphous TiO_2 film ($n > 2.0$) on poly(methyl methacrylate) (PMMA) substrates is demonstrated by a unique

low–temperature process. The resulting films were characterized by means of spectroscopic ellipsometry, transmission electron microscope (TEM), X-ray diffraction (XRD), and atomic force microscope (AFM).

6.2. Experimental Section

6.2.1. Preparation of titanium oxide thin films

Materials. Tetra-n-buthoxide (TTBO; Ti(OC$_4$H$_9$)$_4$ > 97 %) was purchased from Kanto Chemical, Japan. 2-propanol (C$_3$H$_7$OH > 99.5 %) was purchased from Wako Pure Chemical Industries, Japan. Hydrazine monohydrochloride (N$_2$H$_4$ HCl > 98 %) was purchased from Tokyo Chemical Industry, Japan. All reagents were used without further purification.

Synthesis. To prepare the film coating solution, TTBO, 2-propanol, distilled water, and the catalyst hydrazine monohydrochloride were mixed together. Different molar ratio in the precursor solutions was prepared by treating water content as a tunable parameter while fixing [N$_2$H$_4$ HCl]/[Ti(OC$_4$H$_9$)$_4$] to 0.04. [Ti(OC$_4$H$_9$)$_4$] was adjusted to 0.5 mol L^{-1} for all precursors. Table 6.1 summarizes the sample preparation. The solution was mixed slowly at 0 °C to avoid generation and precipitation of TiO$_2$ particles. Without hydrazine monohydrochloride in this preparation, white colored fine particles were immediately generated and precipitated as soon as the solutions were mixed. The mixed solution was then stirred at 25°C for several hours. Silicon(100) (25 × 25 × 1 mm) and PMMA (50 × 50 × 1 mm) substrates were coated with the solution by spin coating (3500 rpm) at 25°C for 60 s. The coated films were dried in a closed container below 10 % relative humidity at 25°C for 1 h, which was followed by a heating process at 40–150°C for 1 h.

6.2.2. Thin film characterization

SAXS experiments were carried out on precursor solutions, in which a SAXSess camera (Anton Paar, Austria) was employed. A Göbel mirror and a block collimator provided a focused monochromatic X-ray beam of Cu Kα radiation. Two-dimensional scattering patterns recorded by an imaging-plate (IP) detector (a Cyclone, Perkin-Elmer) were integrated into to one-dimensional scattering intensities, $I(q)$, where q is the magnitude of

scattering vector. All $I(q)$ data were corrected for the background scattering from a capillary and solvents, and the absolute intensity calibration was made using water as a secondary standard.[35] A model-independent collimation correction (desmearing) procedure was made via an indirect Fourier transformation (IFT) routine. All fitting and fractal analyses were performed on the collimation corrected SAXS intensities. The refractive index, extinction coefficient, and thickness of the films were measured with a spectroscopic ellipsometer UVISEL M200 (Horiba Jobin Yvon, Japan) by using a DeltaPsi 2 simulation software (Horiba Jobin Yvon). The film thickness was also determined from a cross-sectional image of the films using a field-emission scanning electron microscope S-5000 (FE-SEM, Hitachi, Japan). A transmission electron microscope (TEM) image of the amorphous TiO_2 thin film was obtained by means of a JEM-2010 transmission electron microscope (JEOL, Japan) with an acceleration voltage of 200 kV. Fine ground powders of the peeled thin film was dispersed in methanol by ultrasonication. One drop of the suspension was put on a 150 mesh carbon-coated copper grid, and then dried at 60 °C in air. The crystallinity of the dried and heated precursor powders was estimated using a X-ray diffractometer (XRD, Rigaku, RINT2500HF), which was operated at 40 kV and 40 mA, with Cu Kα radiation (λ = 0.1542 nm) in the scanning angles between 20° and 70°. The surface morphology was observed using an atomic force microscope (AFM, Seiko Instruments, SPA400), and the surface root-mean-square roughness values were calculated from AFM images.

Table 6.1. Molar Ratio of Water and 2-Propanol to TTBO in the Precursor Solutions and the Reaction Time in the Sol–Gel Process.

Sample code	Water	2-propanol	reaction time (h)
W2	2.00	21.07	6
W225	2.25	21.02	1
W25	2.50	20.95	0.5

6.3. Results and discussion

6.3.1. Structure of the precursor solutions as obtained by SAXS

SAXS has been used to investigate conformation and the fractal nature of polymer-like aggregates produced in a sol-gel process.[36,37] In order to monitor the microstructure of titanium oxide aggregates in the liquid precursors, their static structures were evaluated by means of SAXS.[38] Figure 6.1 shows SAXS experiments on the titanium oxide precursor solutions, W2, W225, and W25 prepared in varied molar ratio of water, in which collimation-corrected SAXS intensities, $I(q)$, are given in a double-logarithmic plot (Fig. 6.1(A)).

It is established that liner polymers and globular particles show fairly different scattering behavior, leading to different shapes of $I(q)$. Branching of polymer chains imposes somewhat particle-like nature on the polymer chains. For instance, star-branched polymers,[39] dendrimers,[40] nanoparticles comprising tightly crosslinked liner chain precursors,[41] and sol-gel derived high-fractal dimension silica aggregates (indicated in Chapter 2), give a local maximum in a Kratky plot as globular particles do. It is found that all the titanium oxide precursor solutions were to be assigned to a liner polymeric structure in terms of their scattering patterns. Power-law behavior was observed in the intermediate to high-q regime, indicating the emergence of the fractal structure, i.e., self-similarity of the internal structure independent of the chosen length scale. The fractal dimension, d_f, directly appears in the slope of $I(q)$, as represented by the following formula

$$I(q) \propto q^{-d_f} \qquad (6.1)$$

A Kratky plot, $q^2 I(q)$ versus q, is an instructive expression often used to highlight a fractal nature of an ideal or Gaussian coil polymer ($d_f \approx 2$). Instead, a modified Kratky plot, $q^{5/3} I(q)$ versus q was used (Fig. 6.1(B)). The water contents modified the fractal nature of the structure as d_f increased with increasing water content, W2 < W225 ≈ W25. W225 and W25 gave a high-q plateau ($q^{5/3} I(q) \propto q^0$) in this expression, demonstrating $q^{-5/3}$ behavior in $q > \sim 1$ nm^{-1}. The revealed $d_f \approx 5/3 = 1.67$ for W225 and W25 coincides well with d_f of an expanded chain with excluded volume in good solvent. W2, i.e., the liquid precursor with a restricted amount of water,

showed slightly but definitely gentler high–q slope of $q^{-4.7/3}$ corresponding to $d_f \approx 1.54$, which sensitively

showed up as a positive slope in the modified Kratky plot.

$I(q)$ for the titanium oxide precursors in the low–q to intermediate regime can formally be fitted by the

Ornstein-Zernike (OZ) equation[42]

$$I(q) = \frac{I(0)}{1 + \xi^2 q^2} \qquad (6.2)$$

where ξ is the correlation length and $I(0)$ the asymptotic zero-q intensity. It is believed that despite marked

high–q deviation, a fitting analysis based on OZ equation was almost sufficient to evaluate ξ, see Figure 6.1(A).

ξ can be interpreted as the mesh–size of the transient polymer network.[43,44] The radius of gyration, R_g, reflecting

the overall geometry of the polymers, was also evaluated by a Guinier plot based on a Guinier equation, $I(q) =$

$I(0)\exp[-R_g^2 q^2/3]$. The mesh–size ξ for W2 was found to be smallest, giving 2.1 nm. Increasing water content

increased ξ, W225 and W25 showing 2.7 nm and 2.9 nm, respectively. Accordingly, R_g for W2, W225, and

W25 was an increasing function of the water content and estimated to be 3.0 nm, 3.8 nm, and 4.1 nm,

respectively (Table 6.2). The cross-over from expanded coil-like scattering [$I(q) \propto q^{-5/3}$] to rod-like one [$I(q) \propto$

q^{-1}] can clearly be seen for W225 and W25 at $q \sim 3.5$ nm^{-1} whereas such transition is somewhat vague for W2 in

the available q-range.

All abovementioned findings unambiguously demonstrate that the titanium oxide polymers having the

expanded polymer chain–like structure were synthesized using the hydrazine monohydrochloride catalyst in a

reasonably short time (within several hours). To the best of my knowledge, such a weakly-branched structure of

the titanium oxide polymers has never been produced from titanium alkoxides via a ligand–free sol–gel process.

Generally, in order to synthesize a weakly-branched titanium oxide polymers, organic ligands are needed to

stabilize titanium alkoxides. However, organic residues often put issues like coloration on the solid products.

An alternative way is to use an extremely low water content system to retard hydrolysis reactions of titanium

alkoxides, which takes a very long time for the reaction (> 1 month),[36] and thus would not be very practical. In

the next section, it will discuss the interplay of the liquid precursor structures and the properties of the resulting solid film materials.
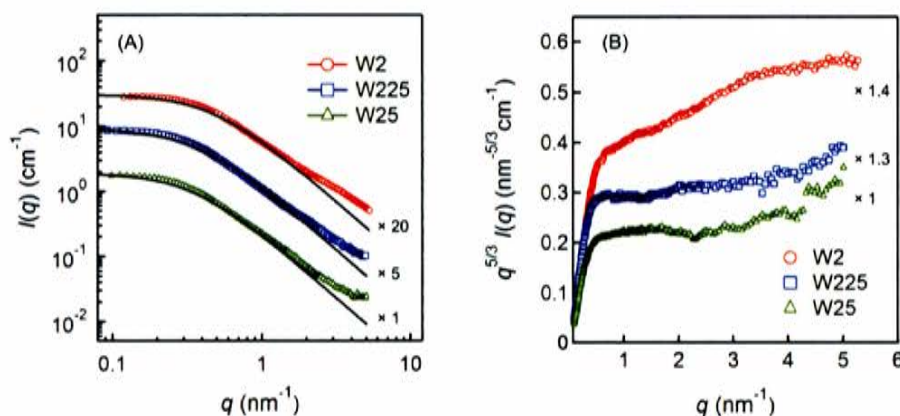

Figure 6.1. SAXS intensities, $I(q)$, on absolute scale and a modified Kratky plot, $q^{5/3}I(q)$ versus q, for the precursor solutions prepared at different water molar ratio, W2 (red), W225 (blue), and W25 (green). The solid lines shown in panel (A) represent optimized fit curves based on the OZ equation.

6.3.2. Optical properties of the amorphous TiO$_2$ thin films on a silicon substrate

Silicon(100) substrates were coated with the precursor solutions, W2, W225, and W25, dominated by the weakly-branched titanium oxide polymers, by spin coating, and then heat–treatment was applied to the dried spin–coated films at varied temperatures ($40 \leq T/°C \leq 150$). In order to investigate optical properties, i.e., refractive index, n, and extinction coefficient, k, of the resulting thin films, a spectroscopic ellipsometry measurement was conducted. Figure 6.2 shows complex optical constants, the n and k curves of the low–temperature (60 °C) heat–treated TiO$_2$ thin films on a Si substrate as a function of wavelength of light, λ. Table 6.3 lists the n values at 550 and 633 nm, the k values at 380 nm, and the film thickness. A noteworthy fact is that as targeted, all the thin films exhibited relatively high n values (> 1.9 at 633 nm) despite such a mild heating condition, which is obviously advantageous for widening a range of applications of the TiO$_2$ optical coating. The attained high n values also imply that the dense amorphous films were produced owing to the mutual interpenetration of the expanded chain-like titanium oxide polymers ($d_f \approx 5/3$) during the drying and

curing processes while avoiding void space creation. Figure 6.3 shows the relation between the mesh size

(correlation length), ξ, of the extended chain–like titanium oxide polymers in the liquid precursors and the

refractive indices, n, of the resulting TiO_2 thin film. Importantly, as shown in Fig. 6.3, it found that the n values

of the thin films almost linearly increased with decreasing water content in the precursor solutions, which

demonstrates that the titanium oxide polymer having smaller ξ was transcribed into finer and denser solid

structures in the thin film (Table 6.2). This view is well supported by the nanoporous silica production via the

catalytic sol–gel process that is discussed in Chapter 2; the silica powders having exclusively micropores

(diameter < 2nm) were produced from a low–fractal dimension polymeric precursor whereas the high–fractal

dimension particle–like aggregates in the liquid precursor resulted in the generation of mesopores (diameter > 5

nm) due to their excluded volume effect.

The k values were found to be almost identical for all the films at 380 nm, giving $< 1\times10^{-4}$ in the wide

visible light range of $\lambda > 390$ nm. The small k values were expected to be accomplished thanks to the absence of

organic residues in this ligand–free synthetic strategy because an organic ligand–coordinated, stabilized

titanium alkoxide generally imposes coloration on the consequent solid products because of its visible light

absorption. In addition, the thin films containing no such organic ligands are expected to be denser, and thereby

to be equipped with higher refractive indices.

Table 6.2. Microscopic Geometries of the Liquid Precursors Prepared at Different Water Concentrations and the Optical Properties and Thickness of the Resulting Amorphous TiO_2 Thin Films Fabricated on a Si Substrate with Low–Temperature Heat–Treatment at 60 °C.[a]

Precursor solution	ξ (nm)	R_g (nm)	Film thickness (nm)	n_{550}	n_{633}	k_{380}
W2	2.1	3.0	100	2.100	2.074	2.96×10^{-3}
W225	2.7	3.8	117	1.991	1.968	3.10×10^{-3}
W25	2.9	4.1	118	1.926	1.905	2.10×10^{-3}

[a]The thickness and optical constants were determined by an analysis of ellipsometric spectra. Notation: ξ, the correlation length estimated by fitting the SAXS curves based on the Ornstein–Zernike equation (eq 2); R_g, the radius of gyration determined with Guinier plot; n_{550}, refractive index at $\lambda = 550$ nm; n_{633}, refractive index at $\lambda = 633$ nm; k_{380}, extinction coefficient at $\lambda = 380$ nm.
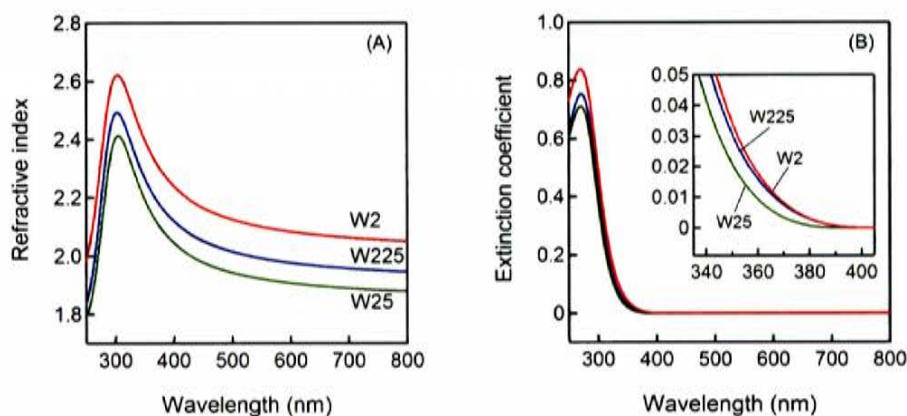
Figure 6.2. Refractive indices (A) and extinction coefficients (B) of the amorphous TiO_2 thin films fabricated form the W2 (red), W225 (blue), and W25 (green) precursor solutions applying low–temperature heat treatment at 60 °C as a function of wavelength, λ. In an inset of the panel (B), the absorption edge ($\lambda = 380$–400nm) is highlighted.
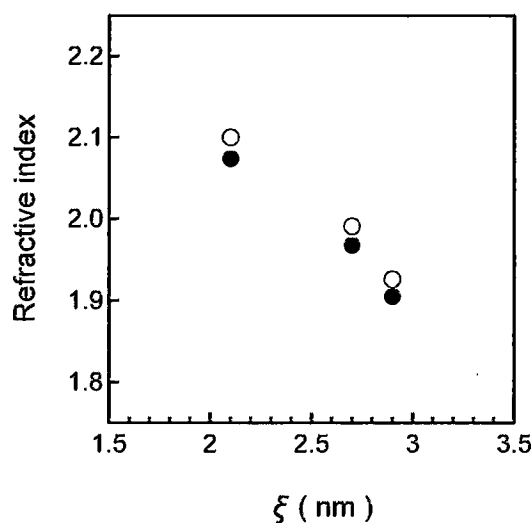
Figure 6.3. The relation between the transient mesh size (correlation length), ξ, of the extended chain–like titanium oxide polymers in the liquid precursors and the refractive indices, n, of the resulting TiO_2 thin film at λ = 550nm (open) and λ = 633 nm (filled), indicating the production of the finer and denser solid architecture from the more microscopic linear polymeric liquid structure.

6.3.3. Structures of the amorphous TiO_2 thin films

The TEM images of the TiO_2 thin films fabricated from the weakly-branched titanium oxide polymer solutions, W2, W225, and W25, with heat–treatment at 60°C are presented in Fig. 6.4. In an optical thin film containing particles dispersed in a matrix, an optical transmission loss may arise from Mie scattering in case that the refractive-index difference between a matrix and particles is large enough, and when the correlation length of the density fluctuation of the aggregates of the dispersed particles becomes comparable to a wavelength of light. In the TEM images, it is hardly observed obvious apertures or particulates at this magnification. The texture of the films was not porous, showing no traces of agglomerated particles, but rather, it looked dense and monolithic. If crystalline particles are dispersed in an amorphous thin film, they often act as scattering objects of lights and become the source of birefringence. A selected-area electron diffraction (SAED) pattern of the W2–based thin film confirms an amorphous nature of the present TiO_2 film, as shown in the inset of Fig. 6.4(A). The dense amorphous TiO_2 monolith involving quite few void spaces and no crystalline particles helps achieve a high n value, simultaneously suppressing optical scattering owing to its fine textured matrix. It is

noteworthy that condensation of the weakly-branched titanium oxide polymers provided the TiO$_2$ films with ultrafine structural features, which is intrinsic to an optical thin film to avoid Mie scattering and to lower the Rayleigh scattering loss in the visible light range.

Structural difference among the TiO$_2$ thin films generated from the precursors having different transient mesh–size, ξ, was not very clear in the TEM images. The revealed notable difference in the refractive indices, i.e. the higher n value of the film for smaller ξ in the liquid precursor, suggests that a microscopic length scale structure as small as ξ contributed to the enhancement of the optical property of the film.

The film thickness of the W2–derived TiO$_2$ film on the silicon substrate with heating at 60°C was found to be ca. 110 nm in view of its cross-sectional SEM image (Fig. 6.5(A)). This is consistent with that evaluated from the ellipsometric data (Table 6.2). The AFM image (Fig. 6.5(B)) and the cross-section profile (Fig. 6.5(C)) of the TiO$_2$ film show that the film is very smooth, showing surface asperity within 1 nm. The root-mean-square surface roughness was estimated to be ca. 0.4 nm. Low roughness reduces the surface scattering loss, and consequently provides excellent optical properties.
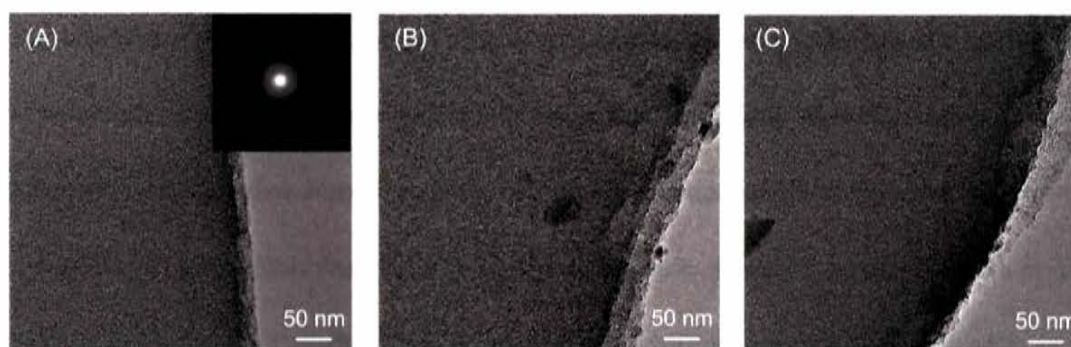

Figure 6.4. TEM images of the TiO$_2$ thin films produced from the (A) W2, (B) W225, and (C) W25 precursor solutions. The inset of the figure (A) shows the selected–area electron diffraction pattern of the TiO$_2$ thin film from W2.
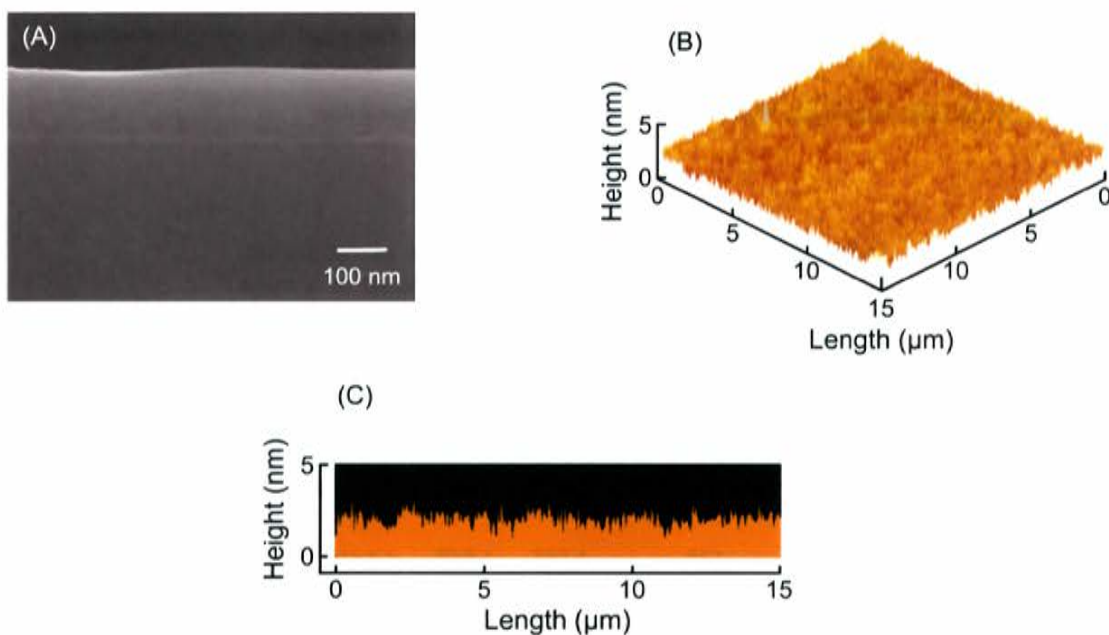
Figure 6.5. Typical images of the W2–derived TiO$_2$ thin film coated on a Si substrate: (A) cross-sectional SEM image, (B) AFM image, and (C) cross-sectional profile. The film was heated at 60°C.

Effects of heating–temperatures on the optical properties were investigated in the amorphous TiO$_2$ thin films prepared from the W2 precursor. Table 6.2 shows the film thicknesses, n values at $\lambda = 550$ and 633 nm, and k values at $\lambda = 380$ nm of the TiO$_2$ thin films coated on the Si substrate. The n value of the TiO$_2$ film was lower than 1.9 with no heat treatment or when the film was heated at < 40°C. With increasing heating temperature, n at $\lambda = 550$ exceeded 2.0, reaching ca.2.1 at 60°C, and finally approached to 2.2 at 80 °C. The heating–temperature dependence of n shown in Fig. 6.6 highlights the presence of the threshold around 60 °C for the n values and the appearance of a plateau at ca. 100 °C. The observation indicates that the low–fractal dimension titanium oxide polymers were able to be sufficiently densified at > 60°C. When a low–heat resistant plastic is used as a substrate, 60°C may be an optimum temperature that can compromise the refractive index and heat resistance of a substrate material. The k values of the films heated below 80°C were $< 5 \times 10^{-3}$ around the absorption edge ($\lambda \approx 380$ nm) and $< 1 \times 10^{-4}$ in the nearly entire visible light range ($390 \leq \lambda/\text{nm} \leq 800$). All TiO$_2$ products heated below 150°C were found to be amorphous by XRD measurements (Fig. 6.7). The optical

data confirm that in comparison to other amorphous TiO_2 thin films fabricated via sol–gel processes at $T <$

$80°C^{26,28,31}$ in previous works, the W2–derived films possessed a higher n value.

Table 6.3. Thickness and Optical Constants of Amorphous TiO_2 Films Fabricated on the Silicon Substrate at Various Heating Temperatures[a]

Heating temperature (°C)	Film thickness (nm)	n_{550}	n_{633}	k_{380}
—	136	1.863	1.846	$< 1 \times 10^{-4}$
40	138	1.885	1.868	$< 1 \times 10^{-4}$
60	100	2.100	2.074	2.96×10^{-3}
80	92	2.155	2.127	4.10×10^{-3}
120	86	2.185	2.153	14.5×10^{-3}
150	88	2.190	2.157	11.9×10^{-3}

[a]The thickness and optical constants were determined by analysis of ellipsometric spectra. Notation: n_{550}, refractive index at $\lambda = 550$ nm; n_{633}, refractive index at $\lambda = 633$ nm; k_{380}, extinction coefficient at $\lambda = 380$ nm.
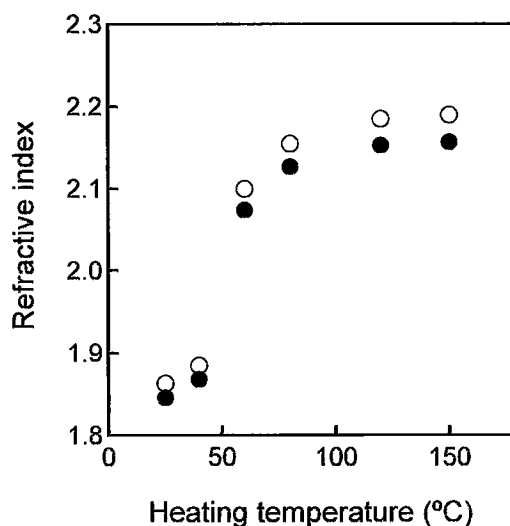
Figure 6.6. Heating–temperature dependence of the refractive indices n at $\lambda = 550$ nm (open circles) and 633 nm (filled circles) of the amorphous TiO_2 thin films fabricated from the W2 precursor on a Si substrate.
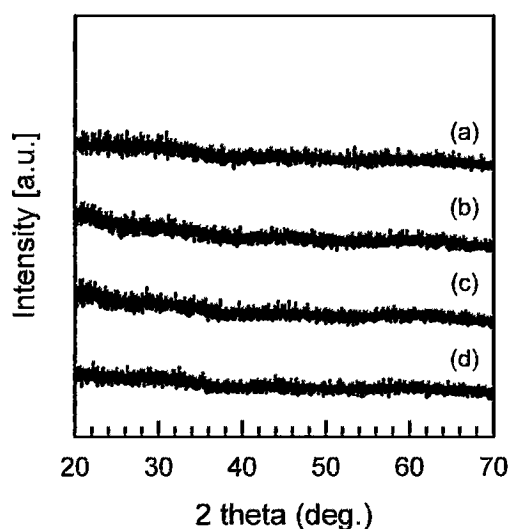
Figure 6.7. XRD patterns of the W2-derived amorphous TiO$_2$ powders heated at 60°C (a), 80°C (b), 120°C (c), and 150°C (d).

6.3.4. Fabrication of the amorphous TiO$_2$ thin film on a PMMA substrate

To widen a range of applications of optical thin films, obviously, the low–temperature process is highly advantageous. However, in the formation of a thin film, physical and chemical properties of a substrate often affect morphological and physical properties of thin films.[9,10] A PMMA plate was used as a substrate of the amorphous TiO$_2$ thin film produced from the W2 precursor solution with heating temperature at 60°C. The surface morphology of the amorphous TiO$_2$ film on a PMMA substrate was found to be very similar to the film on Si shown in Fig. 6.5(B), and its roughness was estimated to be ca. 0.5 nm. Unlike the case of typical crystalline films, the amorphous structure was little affected by the substrate materials.

Figure 6.8 shows the n and k of the amorphous TiO$_2$ film coated on PMMA prepared from the W2 precursor solution at 60°C as a function of wavelength of light. An n of 2.064 at 633 nm and a k of 2.23×10^{-4} at 380 nm can read out from the spectrum. The n value for the film on a PMMA substrate was quite identical with that on a Si substrate obtained at the same heating temperature. The film thickness was also not largely affected by the substitution of the plastic substrate, giving 95 nm. The k value was also $< 1 \times 10^{-4}$ in the almost entire visible light range.

Synthesis of weakly–branched titanium oxide precursors attempted so far needed organic ligands to stabilize titanium alkoxides, and removal of tightly bound organic ligands from a film body required a high temperature process to produce a dense film. This ligand–free catalytic sol–gel technique overcame these issues, and would promote the use of various plastics for a wider range of optical applications.
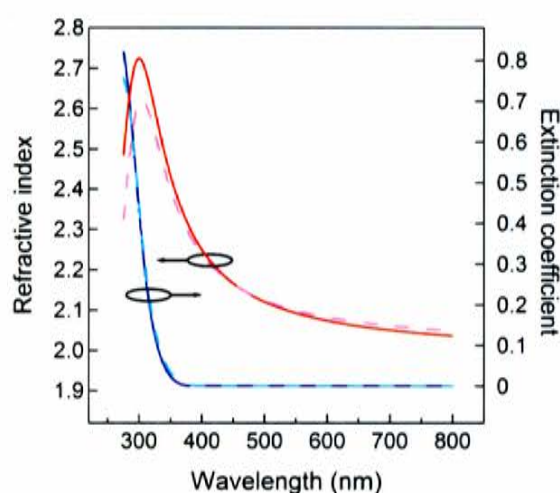

Figure 6.8. Refractive index, n, (solid red) and extinction coefficient, k, (solid blue) of an amorphous TiO_2 thin film coated on a PMMA substrate as a function of wavelength of the light. The film was fabricated from the W2 precursor solution at 60°C. For comparison, the n and k of the amorphous TiO_2 thin film fabricated on a Si substrate under the identical condition are shown together in the broken lines, which are the same data as shown in Fig. 6.2.

6.4. Conclusions

Highly dense amorphous TiO_2 thin films were fabricated from the titanium oxide precursor sols synthesized via the catalytic sol–gel process with the hydrazine monohydrochloride catalyst. The expanded chain-like conformation ($d_f \approx 5/3$) of the titanium oxide polymers were confirmed by SAXS experiments on the precursor sols. The water content in the sol-gel systems, treated as a tuning parameter in this study, did influence the fractal natures as well as the transient mesh size, ξ, of the titanium oxide polymers. Increasing water content increased d_f and ξ. When a silicon (100) wafer was used as a substrate, the thin films obtained by spin coating of the liquid precursor having smaller d_f and ξ showed a higher refractive index, n, which reached

2.074 (at λ = 633 nm) after heat–treatment at 60 °C. The data suggest that densification was accompanied by mutual interpenetration of the expanded polymer–like TiO_2 through the drying and curing of the thin film, which created the monolithic structure involving few apertures, and thus suppressed light scattering loss of the film due to void spaces. The extremely smooth surface of the film confirmed by AFM whose surface roughness was as small as 0.5 nm is a desirable feature for optical materials. The n exceeding 2.0 was identified for the films heat–treated at > 60 °C, and their amorphous structure was preserved even after heating at 150 °C. Such amorphous nature is essential to prevent photocatalytic activity and birefringence. An excellent optical property was demonstrated in the amorphous TiO_2 film coated on PMMA with low temperature (60 °C) heat–treatment; n = 2.064 (at λ = 633 nm), which is identical with that on a Si substrate.

Synthesis of weakly–branched titanium oxide precursors has been attempted so far by using ligands to stabilize titanium alkoxides or spending a long time for the reaction (>1 month) in an extremely low water content system to retard hydrolysis reactions of titanium alkoxides. The catalytic sol–gel technique using hydrazine monohydrochloride as a catalyst enables rapid synthesis (within several hours) of the low-fractal dimension titanium oxide polymers without introducing any organic stabilizers. The resulting amorphous TiO_2 thin films containing no ligand residues are free of coloration caused by optical absorption, and thus are employable as a good optical thin film. The established low–temperature route to the amorphous TiO_2 thin films with high refractive index would open new combination with various resin materials, which potentially develops the use of plastics for a variety of optical applications.

References

1. Bange, K.; Ottermann, C. R.; Anderson, O.; Jeschkowski, U.; Laube, M.; Feile, R. Thin Solid Films 1991, 197, 279–285.

2. Orignac, X.; Barbier, D.; Du, X. M.; Almeida, R. M. Appl. Phys. Lett. 1996, 69, 895–897.

3. Yang, P. D.; Wirnsberger, G.; Huang, H. C.; Cordero, S. R.; McGehee, M. D.; Scott, B.; Deng, T.; Whitesides, G. M.; Chmelka, B. F.; Buratto, S. K.; Stucky, G. D. Science 2000, 287, 465–467.

4. Lee, L. H.; Chen, W. C. Chem. Mater. 2001, 13, 1137–1142.

5. Bartl, M. H.; Boettcher, S. W.; Hu, E. L.; Stucky, G. D. J. Am. Chem. Soc. 2004, 126, 10826–10827.

6. Karaman, M.; Kooi, S. E.; Gleason, K. K. Chem. Mater. 2008, 20, 2262–2267.

7. Rao, Y. Q.; Chen, S. Macromolecules 2008, 41, 4838–4844.

8. Zhang, L.; Li, Y.; Sun, J.; Shen, J. Langmuir 2008, 24, 10851–10857.

9. Hasan, M. M.; Haseeb, A. S. M. A.; Saidur, R.; Masjuki, H. H.; Hamdi, M. Opt. Mater. 2010, 32, 690–695.

10. Martinu, L.; Poitras, D.;   J. Vac. Sci. Technol. A 2000, 18, 2619–2645.

11. Hou, Y. Q.; Zhuang, D. M.; Zhang, G.; Zhao, M.; Wu, M. S. Appl. Surf. Sci. 2003, 218, 97–105.

12. Yamada, Y.; Uyama, H.; Murata, T.; Nozoye, H. J. Vac. Sci. Technol. A 2001, 19, 2479–2482.

13. Kim, S. H.; Lee, J. H.; Hwangbo, C. K.; Lee, S. M. Surf. Coat. Technol. 2002, 158–159, 457–464.

14. Barnes, M. C.; Kumar, S.; Green, L.; Hwang, N. M.; Gerson, A. R. Surf. Coat. Technol. 2005, 190, 321–330.

15. Zhao, Z.; Tay, B. K.; Yu, G. Appl. Opt. 2004, 43, 1281–1285.

16. Musil, J.; Heřman, D.; Šícha, J.   J. Vac. Sci. Technol. A 2006, 24, 521–528.

17. Lin, S. S.; Hung, Y. H.; Chen, S. C. Thin Solid Films 2009, 517, 4621–4625.

18. Hu, Z. G.; Li, W. W.; Wu, J. D.; Sun, J.; Shu, Q. W.; Zhong, X. X.; Zhu, Z. Q.; Chu, J. H. Appl. Phys. Lett. 2008, 93, 181910.

19. Ozer, N.; Demiryont, H.; Simmons, J. H.   Appl. Opt. 1991, 30, 3661–3666.

20. Hu, L. L.; Yoko, T.; Kozuka, H.; Sakka, S. Thin Solid Films 1992, 219, 18–23.

21. Shimooka, H.; Kuwabara, M. J. Am. Ceram. Soc. 1995, 78, 2849–2852.

22. Lee, S. W.; Ichinose, I.; Kunitake, T. Langmuir 1998, 14, 2857–2863.

23. Mosaddeq-ur-Rahman, M.; Yu, G.; Soda, T.; Jimbo, T.; Ebisu, H.; Umeno, M. J. Appl. Phys. 2000, 88, 4634–4641.

24. Hanley, T. L.; Luca, V.; Pickering, I.; Howe, R. F. J. Phys. Chem. B 2002, 106, 1153–1160.

25. He, J. H.; Ichinose, I.; Fujikawa, S.; Kunitake, T.; Nakao, A. Chem. Mater. 2002, 14, 3493–3500.

26. Rantala, J. T.; Kärkkäinen, A. H. O. Opt. Express 2003, 11, 1406–1410.

27. Stathatos, E.; Lianos, P.; Tsakiroglou, C. Langmuir 2004, 20, 9103–9107.

28. Sheng, Y.; Liang, L.; Xu, Y.; Wu, D.; Sun, Y. Opt. Mater. 2008, 30, 1310–1315.

29. Song, X. M.; Wu, J. M.; Tang, M. Z.; Qi, B.; Yan, M. J. Phys. Chem. C 2008, 112, 19484–19492.

30. Brinker, C. J.; Scherer, G. W. In Sol–gel Science, The Physics and Chemistry of Sol–gel Processing, Academic Press: New York, 1990, pp. 797.

31. Shimada, S.; Matsuu, M.; Miyazawa, K.; Kuwabara, M. J. Ceram. Soc. Jpn. 2002, 110, 391–394.

32. Murakami, Y.; Matsumoto, T.; Takasu, Y. J. Phys. Chem. B 1999, 103, 1836–1840.

33. Matsumoto, T.; Murakami, Y.; Takasu, Y. Chem. Lett. 1999, 2, 177–178.

34. Murakami, Y.; Matsumoto, T.; Watanabe, Y.; Takasu, Y. Trans. Mater. Res. Soc. Jpn. 1999, 24, 425–427.

35. Orthaber, D.; Bergmann, A.; Glatter, O. J. Appl. Crystallogr. 2000, 33, 218–225.

36. Kallala, M.; Sanchez, C.; Cabane, B. Phys. Rev. B 1993, 48, 3692–3704.

37. Pattier, B.; Henderson, M.; Brotons, G.; Gibaud, A. J. Phys. Chem. B 2010, 114, 5227–5232.

38. Glatter, O.; Kratky, O. Small-Angle X-Ray Scattering, Academic, London, 1982.

39. Toporowski P. M.; Roovers, J. E. L. Macromolecules 1978, 11 365-368.

40. Tande, B. M.; Wagner, N. J.; Mackay, M. E.; Hawker, C. J.; Jeong, M. Macromolecules 2001, 34, 8580–8585.

41. Mackay, M. E.; Dao T. T.; Tuteja, A.; Ho D. L.; Horn V. H.; Kim, H-C.; Hawker, C. J. Nature materials 2003, 2, 762-766.

42. Ornstein, L. S.; Zernike, F. Proc. Acad. Sci. Amsterdam 1914, 17, 793–806.

43. Pedersen, J. S.; Schurtenberger P. J. Polym. Sci., Part B: Polym. Phys. 2004, 42, 3081–3094.

44. Strobl, G. R. The Physics of Polymers: Concepts for Understanding Their Structures and Behavior, 3rd ed., Springer, Berlin, 2007.

CHAPTER   7

Platinum Nanowire Network with Silica Nanoparticle Spacers for use as an Oxygen Reduction Catalyst

7.1.   Introduction

Platinum-based catalysts in polymer electrolyte membrane fuel cells efficiently convert electricity from

hydrogen and oxygen at low temperature, and have attracted attention because of recent growth in the demand

for alternative energy sources and environmental awareness.[1,2] Platinum nanoparticles (PtNPs) supported on

carbon black (Pt/C) are commercially available and commonly used as anode and cathode catalysts. Most

recent studies have focused on development of cathode catalysts with high catalytic activities and durability for

the oxygen reduction reaction (ORR).[2,3] To increase the ORR activity, PtNPs ($\varnothing$<10 nm) loaded on an

electrically conducting support with a high surface area, such as carbon black, are used to increase the reactive surface area of the platinum. However, such small nanoparticles are generally unstable under fuel cell operating conditions. During initial operation of the fuel cells, the catalytic activity is reduced as the particle diameter increases from 3–4 nm to >5 nm because of dissolution and reprecipitation of the PtNPs.[4-7] Oxidative corrosion of the carbon support has also been observed at applied potentials >0.9 V_{RHE}, which results in aggregation of the PtNPs and a large decrease in the reactive surface area.[7-10]

To increase the durability, alternative support materials have been investigated, including metal compounds with good electrical conductivity and chemical stability.[11,12] For example, Ioroi et al. reported that PtNPs dispersed on Ti_4O_7, a conducting titanium oxide, exhibited improved oxidative resistance compared to that of a commercial Pt/C catalyst.[13,14] Other conducting metal oxides such as SnO_2,[15,16] RuO_2,[17] and sulfated ZrO_2[18] have also been suggested as possible alternatives. Although conducting oxide supports can suppress corrosion, the electrical conductivities of such oxides are lower than carbon blacks and are also not as abundant.

Here, a platinum nanowire network with silica nanoparticle spacers (Pt_{net}/SiO_2) via spray drying and hydrogen reduction was prepared. The use of a platinum nanowire network[19-23] instead of PtNPs eliminated the need for a conducting support. As a novel non-conducting material with good chemical stability and size uniformity to support the high surface area platinum nanowire network, silica nanoparticles (average ø 75 nm) were investigated and the activity and stability with respect to the electrochemical oxygen reduction reaction of the electrocatalysts were studied.

7.2.   Experimental Section

7.2.1.   Preparation of the Pt$_{net}$/SiO$_2$ catalysts

Materials.   Hydrogen hexachloroplatinate(IV) hexahydrate (H$_2$PtCl$_6$·6H$_2$O, >99.9%) and 2-propanol

(>99.7%) were purchased from Wako Pure Chemical Industries (Osaka, Japan). Anhydrous ethylenediamine

(>98%) was purchased from Tokyo Chemical Industry (Tokyo, Japan). PL-7 colloidal silica nanoparticles

(SiO$_2$NPs) dispersed in water (average ø 75 nm, silica mass fraction 23%) was obtained from Fuso Chemical

(Osaka, Japan). Carbon black (EC300J, 800 m^2 g^{-1}) was received from Mitsubishi Chemical Corporation

(Tokyo, Japan). As a control, commercial Pt/C catalyst (TEC10E50E, platinum mass fraction 46.4% on C

Black EC-300J) was obtained from Tanaka Kikinzoku Kogyo (Tokyo, Japan). All chemicals were used as

received.

Preparation of catalysts.   For preparation of the platinum network, H$_2$PtCl$_6$·6H$_2$O was slowly dissolved

in ethylenediamine to make sure the temperature did not rapidly increase. The clear yellow solution was kept in

a tightly sealed bottle at 25 °C for 1 day, and during this time it turned into an opaque paste. 2-Propanol was

added to adjust the platinum concentration to 0.132 mol L^{-1}. The solution was heated at 80 °C for 1 h, and then

added to a nanoparticle dispersion of colloidal silica or carbon black dispersed in 2-propanol at room

temperature. The platinum concentration in the nanoparticle dispersion was 0.066 mol L^{-1}, the molar ratio of

H$_2$PtCl$_6$·6H$_2$O to ethylenediamine was 1 to 22.7, and silica was added at equal mass to the platinum. The

mixture was stirred at 25 °C for 1 h and then sprayed onto a glass plate, which was heated to 105 °C to dry the

nanoparticles without aggregation. A beige powder was obtained, and this was finely ground and reduced in a

tube furnace with an Ar/H$_2$ (H$_2$ volume fraction 10 %) gas stream at 270 °C for 2 h.

7.2.2.   Characterization

Structural and Morphological Characterization.   Each mass fraction of platinum in the black fine

powders, Pt$_{net}$/SiO$_2$ and Pt$_{net}$/C, was determined by means of an EX-200 energy-dispersive X-ray analyzer

(Horiba, Kyoto, Japan). X-ray diffraction (XRD) measurements were conducted with a RINT2500HF X-ray

diffractometer (Rigaku, Tokyo, Japan) with Cu $K\alpha$ radiation ($\lambda = 1.54056$ Å). The diffractometer was operated

at an accelerating voltage of 40 kV with a tube current of 40 mA. Diffraction patterns were collected at

scanning angles between 20° and 90° with a scanning rate of 2° min^{-1} and a step size of 0.02°. The mean

crystallite size, D, of platinum was calculated using the Scherrer formula $D=(0.9\lambda)/(\beta\cos\theta)$, where λ is the X-ray

wavelength, β is the full-width at half-maximum expressed in radians, and θ is the diffraction angle of the

crystalline phase determined at the peak maximum. Transmission electron microscope images of the Pt_{net}/SiO_2

and Pt_{net}/C powders were obtained using a JEM-2100 transmission electron microscope (JEOL, Tokyo, Japan)

equipped with an UltraScan 1000 CCD camera (Gatan, Pleasanton, CA). The accelerating voltage was 200 kV.

Finely ground powder was dispersed in methanol by ultrasonication. One drop of the suspension was placed on

a 150 mesh carbon-coated copper grid, and then dried at 60 °C in air. A S-5000 scanning electron microscope

(Hitachi, Tokyo, Japan) was used to examine the surface morphologies of the Pt_{net}/SiO_2 and Pt_{net}/C powders

with a beam current of 10 μA and an acceleration voltage of 20 kV.

Electrochemical characterization. Electrochemical measurements were carried out using a

three-electrode cell composed of a glassy carbon (GC) disk working electrode (ø 6 mm), a platinum mesh

counter electrode, and a reversible hydrogen electrode as the reference electrode. The solution used for

electrochemical measurements was 0.5 mol L^{-1} H_2SO_4 prepared from sulfuric acid (Wako Pure Chemical

Industries, >96%) and Milli-Q deionized water (>18 MΩ, Millipore, Billerica, MA). The solution temperature

was 60 °C. A HSV-100 potentiostat (Hokuto Denko, Tokyo, Japan) was used for potential control and

recording data. Before the measurements, the GC working electrode was polished to a mirror-like finish with 1

and 0.05 μm alumina polishing suspensions (Baikowski, Annecy, France), and then washed with deionized

water and ethanol. A catalyst layer on the GC electrode was formed using 5 μg of the electrocatalyst and

Nafion® as a binder. A Nafion alcohol/water solution (Nafion mass fraction 5 %, Sigma-Aldrich, St. Louis,

MO) was diluted with ethanol (Wako Pure Chemical Industries, >99.5 %) to one three-hundredth of the

original concentration, and 10 μL of the dilute solution was coated on the GC electrode. Catalyst powder (10

mg) was dispersed in a water/ethanol mixture to a concentration of 1 g L^{-1}. An aliquot (10 μL) of this

homogeneous dark dispersion was dropped onto the Nafion layer on the GC electrode. This embedded the

catalyst in the semidry Nafion layer. After drying at 80 °C for 45 min, the Pt loading on the working electrode

was 17.7 μg cm^{-2}.

Cyclic voltammograms (CVs) were measured in N_2-bubbled electrolyte solution at a scan rate of 50 mV

s^{-1} between 0.05 and 1.20 V$_{RHE}$. The electrochemical surface area of the platinum in each of the catalysts was

derived from hydrogen desorption charges estimated from the CVs.[24-26] Rotating disk electrode experiments

were performed to evaluate the catalytic activity for the ORR.[27-30] The working electrode was mounted on a

rotating disk electrode holder equipped with a rotation speed controller (Nikko Keisoku, Atsugi, Japan). Linear

sweep voltammetry measurements were conducted in O_2-saturated electrolyte at a scan rate of 5 mV s^{-1} from

1.05 to 0.05 V$_{RHE}$ with rotation rates between 1000 and 3000 rpm. The data obtained at all rotation rates were

used for Koutecky–Levich analysis.[31-33] Before these measurements, the catalyst surface was activated by 20

cyclic scans at a scan rate of 50 mV s^{-1} between 0.05 and 1.20 V$_{RHE}$.

Electrochemical degradation test. Accelerated degradation tests were conducted on the three-electrode

cell with the O_2-saturated 0.5 mol L^{-1} H_2SO_4 electrolyte solution at 60 °C. The composition of the testing cell

was same as described above except that a Au disk (ø 6 mm) was used as the working electrode in place of the

GC disk. Scans were repeated 27 000 times with a scanning rate of 100 mV s^{-1} between 0.8 and 1.30 V$_{RHE}$. The

CVs and linear sweep voltammograms were determined after each scan.

Rotating ring-disk electrode (RRDE) experiments. Hydrogen peroxide generated during oxygen

reduction was detected by RRDE measurements using a platinum ring (1 mm width) and GC disk (ø 6 mm)

electrode. Before the measurements, the ring-disk electrode was polished as described above for the disk

electrode. An aliquot (10 μL) of the catalyst dispersion was dropped onto the semidry Nafion layer on the GC

disk electrode, and this step was repeated several times to prepare electrodes with different amounts of the

catalysts. The O_2-saturated 0.1 mol L^{-1} $HClO_4$ electrolyte solution was prepared from perchloric acid (Wako

Pure Chemical Industries, 60 %) and Milli-Q deionized water and kept at 60 °C. Data were collected with an

AUTOLAB PGSTAT 12 potentiostat (Metrohm Autolab B. V., Utrecht, The Netherlands). The catalyst

surface was stabilized by 20 scan cycles between 0.05 and 1.20 V_{RHE} at 50 mV s^{-1}. The GC disk electrode was

swept at 5 mV s^{-1} from 0.05 to 1.02 V_{RHE} while rotating the ring-disk electrode at 2000 rpm and holding the

platinum ring electrode at 1.0 V_{RHE}.

7.3. Results and Discussion

7.3.1. Morphologies of amorphous precursors of the Pt_{net}/SiO_2 catalyst

The transparent yellow solution containing hydrogen hexachloroplatinate(IV) hexahydrate and

ethylenediamine produced brawn colloidal precursors of Pt_{net}. Figure 7.1 shows that TEM images of dried

precursor powder of Pt_{net}/SiO_2. SiO_2 nanoparticles were covered with platinum precursors grown by continuous

reaction in the solution. Before the reduction reaction, the platinum precursors formed a mesh-like morphology.

As discussed in the following section, the conformation of the amorphous precursors is expected to reflect a part

of platinum nanowire network.
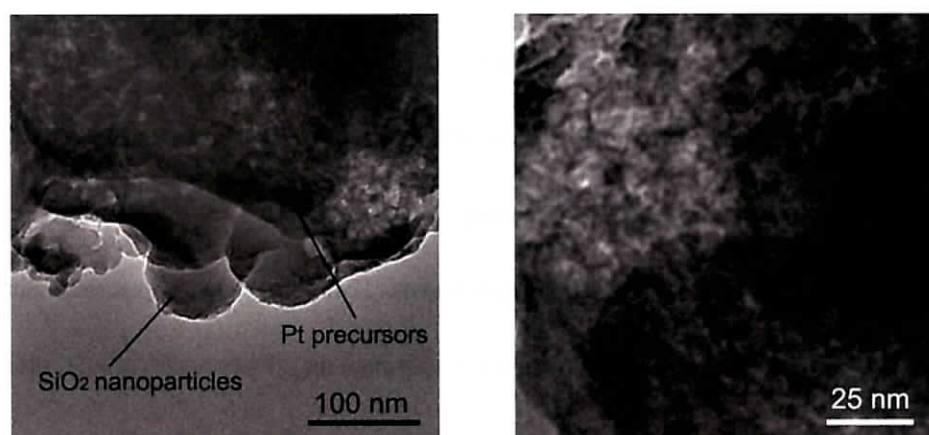
Figure 7.1.   Transmission electron microscopy images of precursor powders of Pt_{net}/SiO_2.

7.3.2. Structures and morphologies of the platinum nanowire networks

The XRD patterns of the Pt_{net}/SiO_2 and Pt_{net}/C catalysts and a commercial Pt/C catalyst confirmed the platinum crystal structure was face-centered cubic (Figure 7.2). Peaks attributed to (111), (200), (220) and (311) reflections were stronger in the diffraction patterns of the Pt_{net}/SiO_2 and Pt_{net}/C catalysts than in that of the commercial Pt/C catalyst. The crystalline sizes were estimated from the full widths at half maximum of the peaks, and those for Pt_{net}/SiO_2 (13.9 nm) and Pt_{net}/C (14.3 nm) were much larger than that of commercial Pt/C (4.2 nm) (Table 7.1).

Scanning electron microscopy images of Pt_{net}/SiO_2 and Pt_{net}/C revealed that the thin platinum nanowire network was spaced by the SiO_2NPs (approximately ø 70 nm) (Figs. 7.3(A) and 7.3(B)). The conducting platinum nanowire network prevented the electron from charging during scanning electron microscopy. The platinum nanowire networks of Pt_{net}/SiO_2 and Pt_{net}/C were also observed by transmission electron microscopy (Figs. 7.3(C) and 7.3(D)). The average diameter of the platinum nanowires in Pt_{net}/SiO_2 (4.5 nm) was less than that of the platinum nanowires in Pt_{net}/C (5.2 nm). The platinum nanowire slightly flattened in shape, like a ribbon rather than a rod. A magnified image of Pt_{net}/SiO_2 revealed continuous crystal growth of platinum with interplanar distances (0.19 nm for {200} and 0.22 nm for {111}) consistent with the face centered cubic platinum structure (Fig. 7.3(E)). The platinum nanowire networks of the prepared catalysts were more complex than platinum nanowire networks prepared by liquid-phase reduction using sodium borohydride,[19,21,22,34] and showed branching and crossing of the nanowires. Because of the branched nanowires, the platinum nanowire network had high density. Moreover, the continuous crystal growth contributed to the presence of few grain boundaries. These unique configurations gave the network high electrical conductivity.
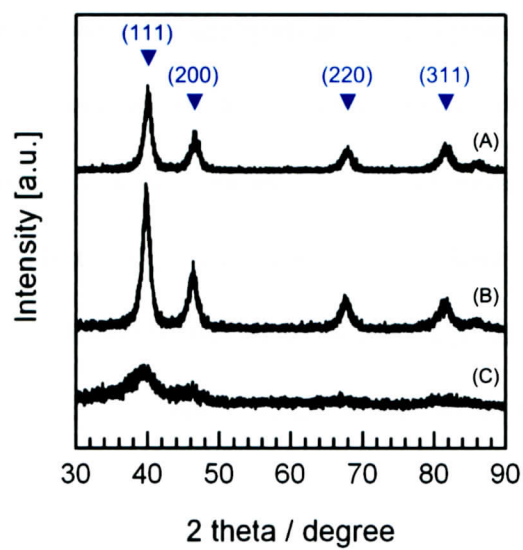
Figure 7.2. XRD patterns of synthesized Pt_{net}/SiO_2 (A) and Pt_{net}/C (B) and commercial Pt/C (C) powders. The peaks are marked with triangles labeled with the Miller indices, (*hkl*), for the face centered cubic crystal.
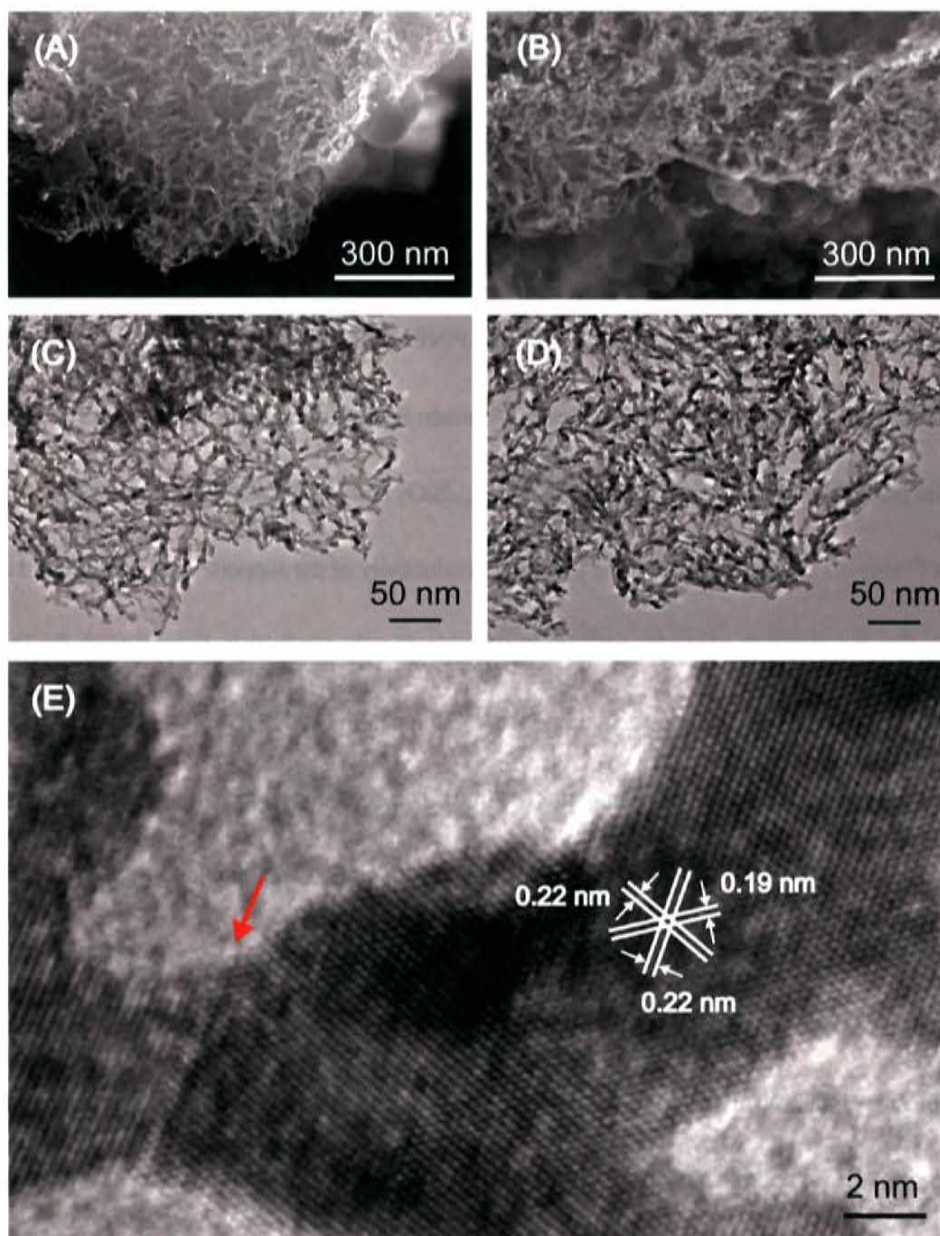
Figure 7.3. Scanning electron microscopy images of Pt_{net}/SiO_2 (A) and Pt_{net}/C (B), transmission electron microscopy images of Pt_{net}/SiO_2 (C) and Pt_{net}/C (D), and a typical magnified transmission electron microscopy image of the networked platinum (E). The red arrow indicates the location of a grain boundary.

7.3.3. Comparison of electrochemical properties

The CVs of Pt_{net}/SiO_2 and Pt_{net}/C showed characteristic double anodic current peaks at approximately 0.12 and 0.25 V_{RHE} (Figs. 7.4(A) and 7.5(A)). These peaks could be attributed to hydrogen desorption from the

platinum surface on the (110) plane (0.12 V_{RHE}) and (100) plane (0.25 V_{RHE}).[35] The peak shapes for the platinum nanowire networks were similar to that of Pt black[36] and Pt/C, which indicates that the platinum nanowire networks consist of polycrystalline platinum.[37] For commercial Pt/C, a third anodic current peak was observed between those at 0.12 and 0.25 V_{RHE} (Fig. 7.5(D)), which can be attributed to the high content of platinum atoms with low surface coordination in the PtNPs.[35,38] By contrast, this peak was not observed for the platinum nanowire networks, which indicates they contain few platinum atoms with low surface coordination.

The electrochemical surface areas (ESA) of Pt_{net}/SiO_2 and Pt_{net}/C were half that of the commercial Pt/C catalyst (Table 7.1). Independence of the electrical conductivity of the support, such as silica and carbon black, suggests that the platinum nanowire network itself is electrically conductive. Even though the Pt_{net}/SiO_2 (13.9 nm) and Pt_{net}/C (14.3 nm) had large crystalline sizes (estimated by XRD), the ESA were quite high because the networks are made of fine platinum nanowires (ø 4 nm). The ESA of a support-free platinum nanowire network catalyst, 21.8 m^2 g_{pt}^{-1}, derived from the platinum precursor solution containing no SiO_2NPs was smaller than the ESA of Pt_{net}/SiO_2, 27.9 m^2 g_{pt}^{-1}. The data imply that the SiO_2NPs acted as a spacer inhibiting densification during the crystal growth of platinum through the calcination and reduction process.

Kinoshita indicated that the number of the edge and corner sites decreased with increasing platinum particle size.[39] Low coordination platinum atoms are exposed at edges and corners. Large crystal size and diameter of the platinum nanowire networks probably decreased these sites. Also, from TEM images (Figs. 7.3 (C) and 7.3(D)), the flat surface of the platinum nanowire network were expected to decrease the edge and corner sites.

Koutecky-Levich plots (Fig. 7.4(B)) were constructed from linear sweep voltammograms measured using a GC

disc (ø 6 mm) electrode at rotation rates between 500 and 3000 rpm (Fig. 7.4(C)). The mass activity, $j_{k\text{-mass}}$, of

Pt_{net}/SiO_2 (115.8 A g_{Pt}^{-1} at 0.85 V_{RHE}) was higher than that of commercial Pt/C (103.4 A g_{Pt}^{-1} at 0.85 V_{RHE}).

Because Pt_{net}/SiO_2 had half the ESA of the commercial catalyst but higher mass activity, its specific activity, j_k

(0.415 mA cm_{Pt}^{-2} at 0.85 V_{RHE}) was twice that of the commercial Pt/C (0.155 mA cm_{Pt}^{-2} at 0.85 V_{RHE}). The j_k

of Pt_{net}/C (0.358 mA cm_{Pt}^{-2} at 0.85 V_{RHE}) was relatively low compared to that of Pt_{net}/SiO_2 even though the

platinum nanowire network was identical. The specific activity depends on surface properties of platinum, such

as an electronic state and a coordination number, and is affected by the chemical characteristics of the support[40]

and the number of platinum atoms, i.e., particle size.[39,41] The large crystal size of platinum of Pt_{net}/SiO_2 and

Pt_{net}/C would contribute to the high specific activity of ORR.[42]

Table 7.1. Summary of the catalyst properties.[a]

Sample	w_{pt} (%)	$D_{(111)}$ / nm	S / $m^2 g_{Pt}^{-1}$	j_k at 0.85 V_{RHE} / mA cm_{Pt}^{-2}	$j_{k\text{-mass}}$ at 0.85 V_{RHE} / A g_{Pt}^{-1}
Pt_{net}/Si_2	51.1	13.9	27.9	0.415	115.8
Pt_{net}/C	48.8	14.3	28.5	0.358	102.0
Pt/C (commercial)	46.4	4.2	56.6	0.155	103.4

[a]Notation: w_{pt}, Pt mass fraction determined from the EDX analysis except Pt/C (commercial); $D_{(111)}$, Pt crystallite diameter calculated using the Scherrer equation with full width at half maximum of the (111) peak; S, electrochemical surface area (ESA) calculated from hydrogen desorption charges; j_k, specific activity given as kinetic current density in Koutecky-Levich plots; $j_{k\text{-mass}}$, mass activity calculated from j_k and ESA. All electrochemical measurements were conducted using a glassy carbon disc electrode.
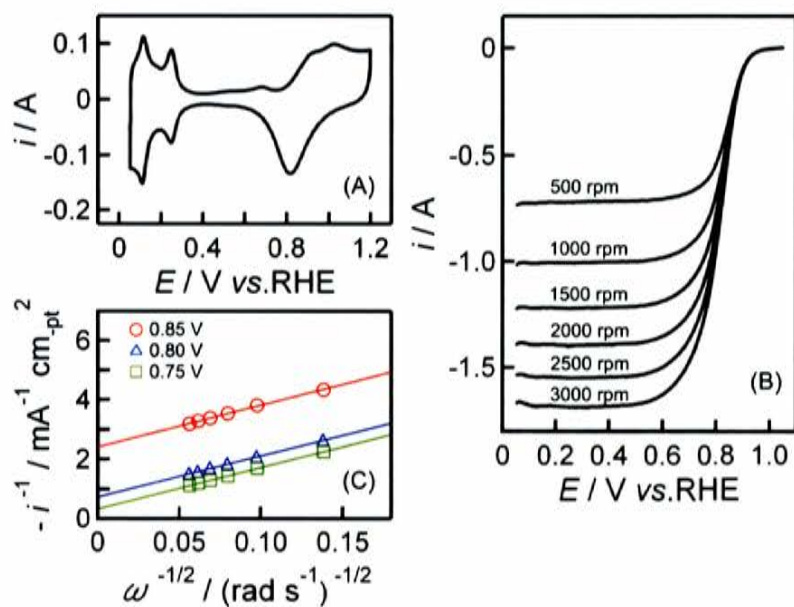
Figure 7.4. Electrochemical properties of the Pt$_{net}$/SiO$_2$ catalyst. (A) A cyclic voltammogram measured in a N$_2$-saturated electrolyte solution of 0.5 mol L^{-1} H$_2$SO$_4$ at 60 °C with a scan rate of 50 mV s^{-1}, (B) linear sweep voltammograms measured in O$_2$-saturated electrolyte solution of 0.5 mol L^{-1} H$_2$SO$_4$ at 60 °C with a scan rate of 5 mV s^{-1}, and (C) Koutecky-Levich plots using extracted data from the kinetic ORR currents at 0.85 V$_{RHE}$ (red circle), 0.80 V$_{RHE}$ (blue triangle), and 0.75 V$_{RHE}$ (green square).
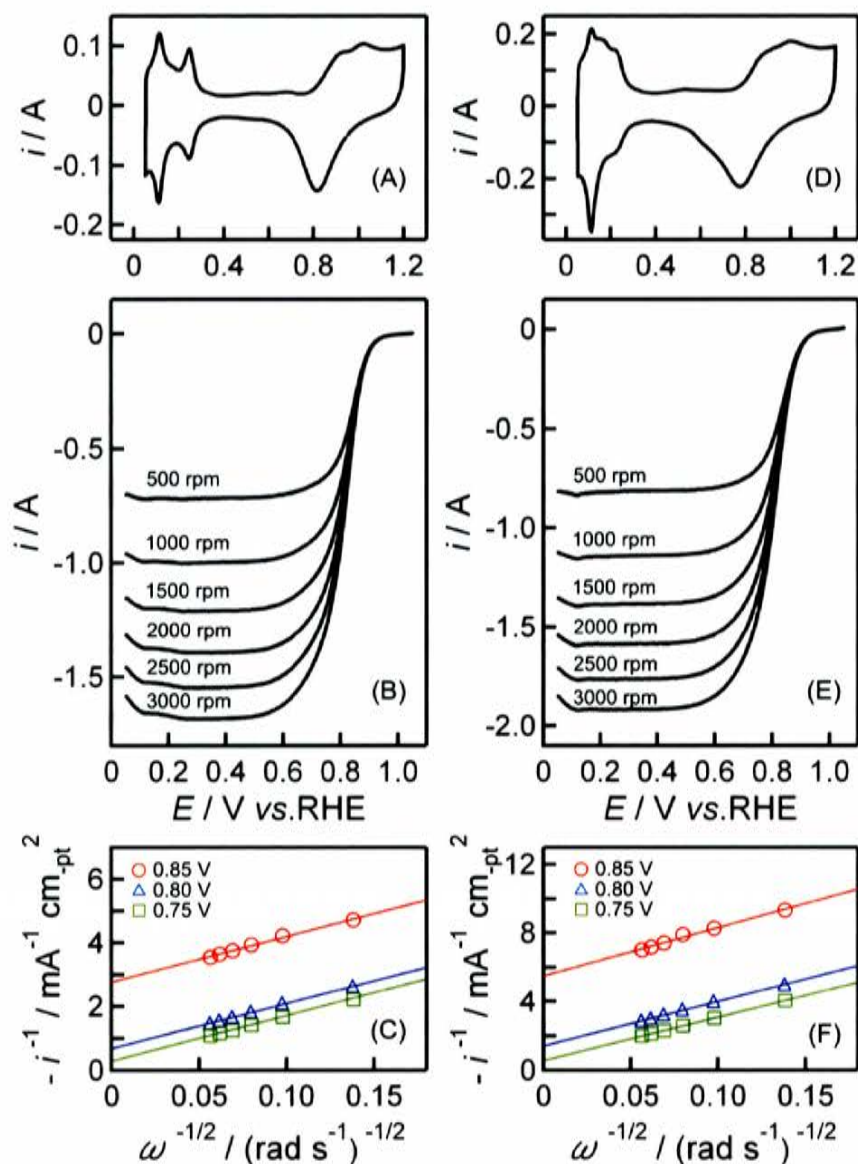
Figure 7.5. Electrochemical properties of the Pt_{net}/C (left) and commercial Pt/C catalysts (right). (A) and (D) Cyclic voltammograms measured in a N_2-saturated electrolyte solution of 0.5 mol L^{-1} H_2SO_4 at 60 °C with a scan rate of 50 mV s^{-1}, (B) and (E) linear sweep voltammograms measured in an O_2-saturated electrolyte solution of 0.5 mol L^{-1} H_2SO_4 at 60 °C with a scan rate of 5 mV s^{-1}, and (C) and (F) Koutecky-Levich plots using extracted data from the kinetic ORR currents at 0.85 V_{RHE} (red circle), 0.80 V_{RHE} (blue triangle), and 0.75 V_{RHE} (green square).

7.3.4. Durability studies of platinum nanowire networks

Accelerated durability testing (ADT) of Pt_{net}/SiO_2 (Fig. 7.6 (A)) was carried out by 27 000 repeat cyclic voltammetry scans between 0.8 and 1.3 V_{RHE} at a scanning rate of 100 mV s^{-1}. The results were compared to those for commercial Pt/C (Fig. 7.6 (C)). To avoid electrode corrosion, a Au rotation electrode was used for the ADT instead of the glassy carbon electrode that is widely used for fuel cell catalysts. The ESA of Pt_{net}/SiO_2 (Fig. 7.6(B)) decreased by 4% after the ADT, whereas that of Pt_{net}/C decreased by 23% (Table 7.2). These reductions were attributed to oxidative corrosion of the carbon support, which would partially collapse the platinum nanowire network. Oxidation of the carbon supports was reflected the increase in double layer capacitance between about 0.4 and 0.6 V_{RHE} with repetition of the cyclic voltammetry of Pt_{net}/C and commercial Pt/C.[43,44] The use of SiO_2NPs stabilized the platinum nanowire network during ORR. The high durability of Pt_{net}/SiO_2 was probably caused by the stability of the silica support against corrosion and of the platinum nanowire network structure during ORR.

The ESA of the commercial Pt/C decreased by >50% (Fig. 7.6 (D)), and this was much larger than the decrease for Pt_{net}/C (23%). This difference between the catalysts could arise from the degree of platinum dissolution. The PtNPs in commercial Pt/C have a high concentration of low-coordination platinum edge sites, which are more likely to dissolve during potential cycling.[4,6,45] The low-coordination platinum edge sites would be easily oxidized with the oxygen species, gradually producing dissoluble platinum ion during the oxidation-reduction cycles. The platinum nanowire network has a low concentration of low-coordination platinum edge sites, which is advantageous over the PtNPs because it stops platinum dissolution during the redox cycle.

The $j_{k\text{-mass}}$ of Pt_{net}/SiO_2 decreased by 23%, and with the small ESA decrease for this catalyst the $j_{k\text{-mass}}$ decrease could be attributed to the j_k decrease (38%). By contrast, larger decreases in the $j_{k\text{-mass}}$ of Pt_{net}/C (34%) and commercial Pt/C (43%) were observed, and with the slight j_k changes for these catalysts the $j_{k\text{-mass}}$ decrease could be attributed to their ESA decreases. The j_k decrease for Pt_{net}/SiO_2 would be caused by changes in the

state of the platinum on the inside of the structure during ORR. The j_k of Pt_{net}/C, which had the same platinum

nanowire network, remained constant even after the ADT, whereas its ESA decreased. The j_k decrease of

platinum strongly depended on its surface and sub-surface state. Changes in the state of the platinum on the

inside of the structure occur through processes at the platinum surface, such as diffusion of oxygen species into

subsurfaces of the bulk platinum.[46,47]

Table 7.2.   Summary of the catalyst properties for the cycle test.[a]

Sample	S $/ m^2 g_{Pt}^{-1}$		j_k at 0.85 V_{RHE} $/ mA cm_{Pt}^{-2}$		j_{k-mass} at 0.85 V_{RHE} $/ A g_{Pt}^{-1}$	
	initial[b]	last[c]	initial	last	initial	last
Pt_{net}/SiO_2	31.3	29.8	0.37	0.28	110.5	84.8
Pt_{net}/C	26.9	20.4	0.39	0.34	105.9	70.1
Pt/C (commercial)	58.3	29.0	0.17	0.20	100.2	57.0

[a]Notation: S, electrochemical surface area (ESA) calculated from hydrogen desorption; j_k, specific activity given as kinetic current density in Koutecky-Levich plots; j_{k-mass}, mass activity calculated from j_k and ESA. All electrochemical measurements were conducted using a Au disc electrode.
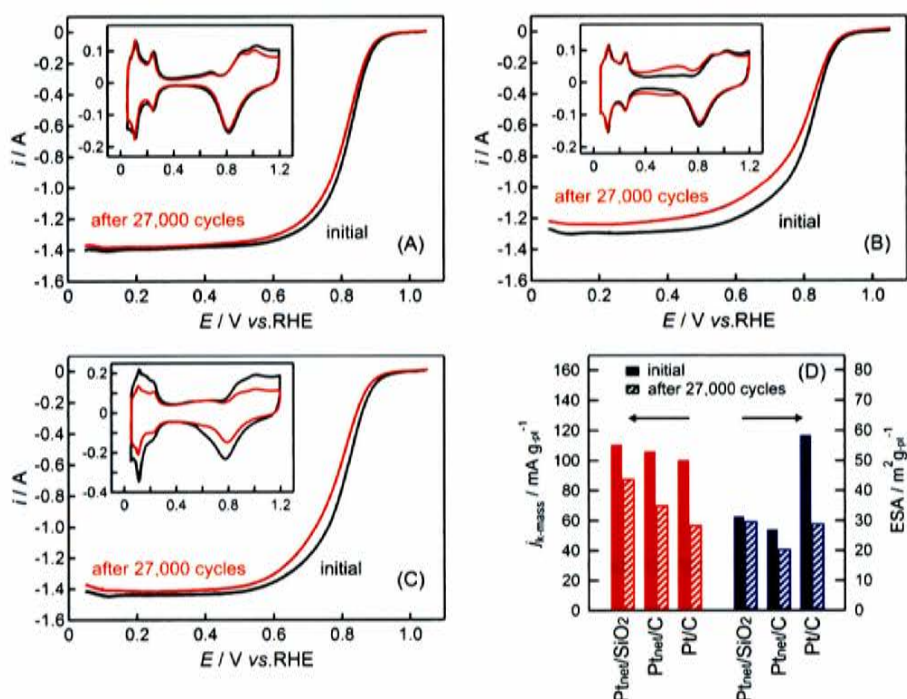
Figure 7.6. Comparison of the linear sweep voltammograms and cyclic voltammograms (inset) before (black) and after (red) accelerated degradation testing for the Pt_{net}/SiO_2 (A), Pt_{net}/C (B), and commercial Pt/C (C) catalysts, and comparison of the ORR mass activities s (red) and ESAs (blue) of each catalyst (D). Linear sweep voltammograms were measured in an O_2-saturated electrolyte solution of 0.5 mol L^{-1} H_2SO_4 at 60 °C with a scan rate of 5 mV s^{-1} and electrode rotation rate of 2000 rpm. Cyclic voltammograms were measured in a N_2-saturated electrolyte solution of 0.5 mol L^{-1} H_2SO_4 at 60 °C with a scan rate of 50 mV s^{-1}.

5.3.5. Selectivity of oxygen reduction on platinum nanowire networks

The electrocatalytic activities of the Pt_{net}/SiO_2 and commercial Pt/C catalysts toward the reduction of oxygen to hydrogen peroxide were evaluated using the ring-disk electrode.[29,48] Hydrogen peroxide molecules generated from a platinum catalyst on the disk electrode will diffuse through the electrolyte to the ring electrode, where the hydrogen peroxide is oxidized to water. The magnitude of the ring current reflects the amount of hydrogen peroxide decomposed on the ring electrode. In large quantities, the platinum catalysts considerably decreased the ring current (Fig. 7.7). Hydrogen peroxide was partially decomposed to water over the platinum catalysts on the disk electrode during diffusion to the ring electrode.[49] High ring currents were observed with the Pt_{net}/SiO_2 (1.0 μg_{-Pt}) and the commercial Pt/C (0.5–1.0 μg_{-Pt}) catalysts over a wide potential range (0.05–0.6

V_{RHE}), and the influence of catalytic decomposition of hydrogen peroxide would be small. When the ring

currents of these catalysts were compared at an arbitrary potential below 0.6 V_{RHE}, the ring current of Pt_{net}/SiO_2

(1.0 μg_{Pt}) was less than the half that of the commercial Pt/C catalyst (0.5 and 1.0 μg_{Pt}). These results imply that

the platinum nanowire network in the Pt_{net}/SiO_2 prevents hydrogen peroxide from forming, unlike the PtNPs in

the commercial Pt/C catalyst. This phenomenon was especially notable at low potentials (<0.4 V_{RHE}). The

characteristics of hydrogen peroxide generation on the Pt_{net}/C catalyst were similar to those for the Pt_{net}/SiO_2

catalyst, and this was confirmed by the RRDE experiments. It is expected that the higher j_k for Pt_{net}/SiO_2 and

Pt_{net}/C (Table 7.1) is because of the low selectivity for hydrogen peroxide generation in the oxygen reduction

reaction.

Bridge site adsorption of an oxygen molecule will occur on the flat platinum surface of the platinum

nanowire network in Pt_{net}/SiO_2 and Pt_{net}/C, which helps dissociation of oxygen into oxygen atoms and the

four-electron ORR into water. Bidentate site adsorption on the low-coordination platinum edge site in the

commercial Pt/C catalyst will prevent the oxygen molecule from dissociating, which favors hydrogen peroxide

formation via the two-electron ORR. The decrease in hydrogen peroxide formation will prevent decreases in

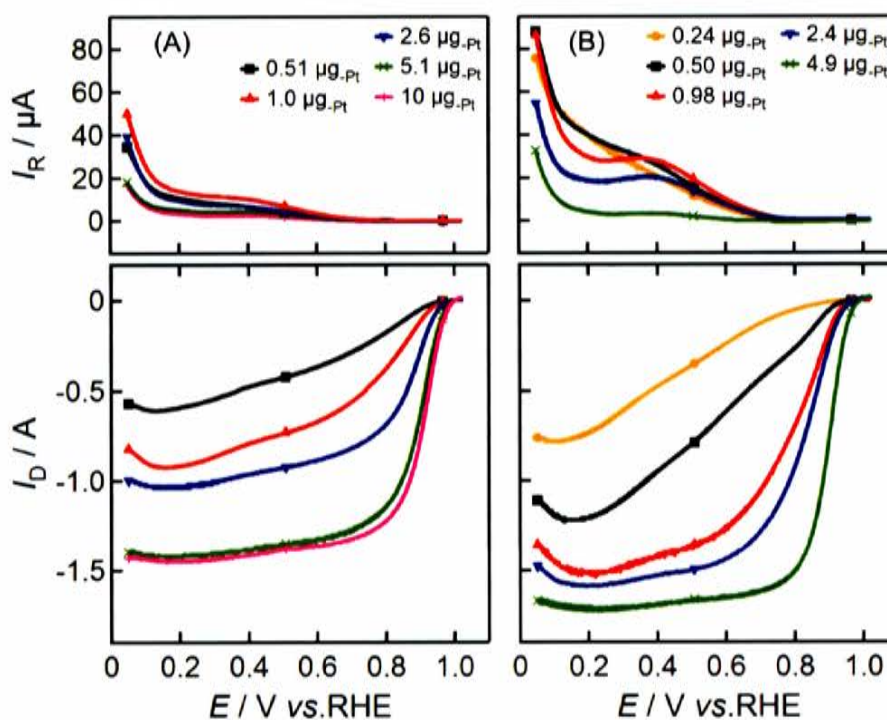the cell performance that are caused by polymer membrane decomposition because of hydrogen peroxide.[7,50]

Figure 7.7. Ring, I_R, (top) and disk, I_D, (bottom) currents of different quantities of the Pt_{net}/SiO_2 (A) and commercial Pt/C (B) catalysts loaded on the GC disk electrode during ORR in an O_2-saturated electrolyte solution of 0.1 mol L^{-1} HClO$_4$ at 60 °C. The potential of the GC disk electrode was swept at 5 mV s^{-1} from 0.05 to 1.02 V_{RHE} with rotating the ring-disk electrode at 2000 rpm, while the platinum ring electrode was held at 1.0 V_{RHE}.

7.5.4. Conclusions

Platinum nanowire (ø 4 nm) networks with SiO$_2$NP spacers were synthesized by reduction using H$_2$ gas instead of metal borohydride. These networks exhibited higher electrocatalytic activity and durability for the ORR then commercial Pt/C. The high ORR mass activity of Pt_{net}/SiO_2 could be attributed to its high specific activity per platinum surface area compared to the PtNPs. The use of SiO$_2$NPs stabilized the platinum nanowire network during both calcination and H$_2$ reduction in the catalyst preparation and ORR. After ADT of Pt_{net}/SiO_2, the ESA remained constant and the mass activity decreased by 23.2%. This decrease was much smaller than that of commercial Pt/C (43.1%). The selectivity of the ORR for hydrogen peroxide on Pt_{net}/SiO_2 was lower than that on the commercial Pt/C. The decrease in the hydrogen peroxide formation is also expected to increase the durability of polymer membranes.

References

1. B. C. H. Steele, A. Heinzel, Nature 414 (2001) 345–352.

2. H. A. Gasteiger, S. S. Kocha, B. Sompalli, F. T. Wagner, Appl. Catal. B: Environ. 56 (2005) 9–35.

3. P. Mani, R. Srivastava, P. Strasser, J. Phys. Chem. C 112 (2008) 2770–2778.

4. Kinoshita, K.; Lundquis, J. T.; Stonehart, P. J. Electroanal. Chem. Interfacial. Electrochem. 1973, 48, 157.

5. Yasuda, K.; Taniguchi, A.; Akita, T.; Ioroi, T.; Siroma, Z. Phys. Chem. Chem. Phys. 2006, 8, 746.

6. Wang, X. P.; Kumar, R.; Myers, D. J. Electrochem. Solid State Lett. 2006, 9, A225.

7. Borup, R.; Meyers, J.; Pivovar, B.; Kim, Y. S.; Mukundan, R.; Garland, N.; Myers, D.; Wilson, M.; Garzon, F.; Wood, D.; Zelenay, P.; More, K.; Stroh, K.; Zawodzinski, T.; Boncella, J.; McGrath, J. E.; Inaba, M.; Miyatake, K.; Hori, M.; Ota, K.; Ogumi, Z.; Miyata, S.; Nishikata, A.; Siroma, Z.; Uchimoto, Y.; Yasuda, K.; Kimijima, K.; Iwashita, N. Chem. Rev. 2007, 107, 3904.

8. Antolini, E. J. Mater. Sci. 2003, 38, 2995.

9. Roen, I. M.; Paik, C. H.; Jarvi, T. D. Electrochem. Solid-State Lett. 2004, 7, A19.

10. Maass, S.; Finsterwalder, F.; Frank, G.; Hartmann, R.; Merten, C. J. Power Sources 2008, 176, 444.

11. Shao, Y. Y.; Liu, J.; Wang, Y.; Lin, Y. H. J. Mater. Chem. 2009, 19, 46.

12. Antolini, E.; Gonzalez, E. R. Solid State Ionics 2009, 180, 746.

13. Ioroi, T.; Siroma, Z.; Fujiwara, N.; Yamazaki, S.; Yasuda, K. Electrochem. Commun. 2005, 7, 183.

14. Chen, G. Y.; Bare, S. R.; Mallouk, T. E. J. Electrochem. Soc. 2002, 149, A1092.

15. Santos, A. L.; Profeti, D.; Olivi, P. Electrochim. Acta 2005, 50, 2615.

16. Masao, A.; Noda, S.; Takasaki, F.; Ito, K.; Sasaki, K.; Electrochem. Solid-State Lett. 2009, 12, B119.

17. Lasch, K.; Hayn, G.; Jorissen, L.; Garche, J.; Besenhardt, O. J. Power Sources 2002, 105, 305.

18. Suzuki, Y.; Ishihara, A.; Mitsushima, S.; Kamiya, N.; Ota, K. Electrochem. Solid-State Lett. 2007, 10, B105.

19. Song, Y.; Garcia, R. M.; Dorin, R. M.; Wang, H. R.; Qiu, Y.; Coker, E. N.; Steen, W. A.; Miller, J. E. Shelnutt, J. A. Nano Lett. 2007, 7, 3650.

20. Chen, A.; Holt-Hindle, P. Chem. Rev. 2010, 110, 3767.

21. Koenigsmann, C.; Zhou, W. P.; Adzic, R. R.; Sutter, E.; Wong, S. S. Nano Lett. 2010, 10, 2806.

22. Wang, S. Y.; Jiang, S. P.; Wang, X.; Guo, J. Electrochim. Acta 2011, 56, 1563.

23. Antolini, E.; Perez, J. J. Mater. Sci. 2011, 46, 4435.

24. Min, M. K.; Cho, J. H.; Cho, K. W.; Kim, H. Electrochim. Acta 2000, 45, 4211.

25. Shih, Y. H.; Sagar, G. V.; Lin, S. D.; J. Phys. Chem. C 2008, 112, 123.

26. Mayrhofer, K. J. J.; Strmcnik, D.; Blizanac, B. B.; Stamenkovic, V.; Arenz, M.; Markovic, N. M. Electrochim. Acta 2008, 53, 3181.

27. Watanabe, M.; Igarashi, H.; Yosioka, K. Electrochim. Acta 1995, 40, 329.

28. Schmidt, T. J.; Gasteiger, H. A.; Stab, G. D.; Urban, D. M.; Behm, R. J. J. Electrochem. Soc. 1998, 145, 2354.

29. Paulus, U. A.; Wokaun, A.; Scherer, G. G.; Schmibt, T. J.; Stamenkovic, V.; Radmilovic, V.; Markovic, N. M.; Ross, P. N. J. Phys. Chem. B 2002, 106, 4181.

30. Dutta, I.; Carpenter, M. K.; Balogh, M. P.; Ziegelbauer, J. M.; Moylan, T. E.; Atwan, M. H.; Irish, N. P. J. Phys. Chem. C 2010, 114, 16309.

31. Koutecky, J.; Levich, V. G. Zh. Fiz. Khim. 1958, 32, 1565.

32. Colon-Mercado, H. R.; Popov, B. N. J. Power Sources 2006, 155, 253.

33. Unni, S. M.; Dhavale, V. M.; Pillai, V. K.; Kurungot, S. J. Phys. Chem. C 2010, 114, 14654.

34. Naohara, H.; Yoshimoto, T.; Toshima, N. J. Power Sources 2010, 195, 1051.

35. Solla-Gullon, J.; Rodriguez, P.; Herrero, E.; Aldaz, A.; Feliu, J. M. Phys. Chem. Chem. Phys. 2008, 10, 1359.

36. Han, K. S.; Han, O. H. Electrochim. Acta, 2001, 47, 519.

37. Garbarino, S.; Ponrouch, A.; Pronovost, S.; Gaudet, J.; Guay, D. Electrochem. Commun. 2009, 11, 1924.

38. Gómez, R.; Clavilier, J. J. Electroanal. Chem. 1993, 354, 189.

39. Kinoshita, K. J. Electrochem. Soc. 1990, 137, 845.

40. Stakheev, A. Y.; Kustov, L. M. Appl. Catal. A 1999, 188, 3.

41. Mukerjee, S.; McBreen, J. J. Electroanal. Chem. 1998, 448, 163.

42. Takasu,Y.; Ohashi, N.; Zhang, X. G.; Murakami, Y.; Minagawa, H.; Sato, S.; Yahikozawa, K. Electrochim. Acta 1996, 41, 2595.

43. Wang, J. J.; Yin, G. P.; Shao, Y. Y.; Zhang, S.; Wang, Z. B.; Gao, Y. Z. J. Power Sources 2007, 171, 331.

44. Cherstiouk, O. V.; Simonov, A. N.; Moseva, N. S.; Cherapanova, S. V.; Simonov, P. A. Zaikovskii, V. I.; Savinova, E. R. Electrochim. Acta 2010, 55, 8453.

45. Jinnouchi, R.; Toyoda, E.; Hatanaka, T.; Morimoto, Y. J. Phys. Chem. C 2010, 114, 17557.

46. Danilov, A. I.; Molodkina, E. B.; Polukarov, Y. M.; Russ. J. Electrochem. 2004, 40, 585.

47. Gu, Z. H.; Balbuena, P. B. J. Phys. Chem. C 2007, 111, 9877.

48. Yang, H.; Vogel, W.; Lamy, C.; Alonso-Vante, N. J. Phys. Chem. B 2004, 108, 11024.

49. Inaba, M.; Yamada, H.; Tokunaga, J.; Tasaka, A. Electrochem. Solid-State Lett. 2004, 7, A474.

50. Ohma, A.; Suga, S.; Yamamoto, S.; Shinohara, K. J. Electrochem. Soc. 2007, 154, B757.

CHAPTER 8

General Summary

The series of studies demonstrate the relations ranging from conformation of precursor polymers to

nanostructures of resulting solids and their excellent properties (Scheme 8.1). The characteristic nanostructures

of porous silica and dense titania solids were produced by the catalytic sol–gel technique using unique catalysts,

i.e., hydroxyacetone and hydrazine monohydrochloride, respectively. The catalytic sol–gel processes enabled

conformation control of liquid precursors of silica and titania, affecting nanostructures of solid materials and

their characteristics. In addition, the distinctive 1-d nanostructure of platinum nanowire network also reflected

the conformation of precursor polymers fabricated by a polymerized complex process being a type of the

sol-gel technique. The excellent properties of nanostructured silica, titania and platinum materials were

investigated, indicating low and high refractive indices, superhydrophilicities and high catalyst durability. Owing to their characteristic nanostrctures, these solid materials generated noteworthy characters. In addition, each property was inevitably influenced by the nanostructure of the solid. The details of the results from each chapter are summarized below.
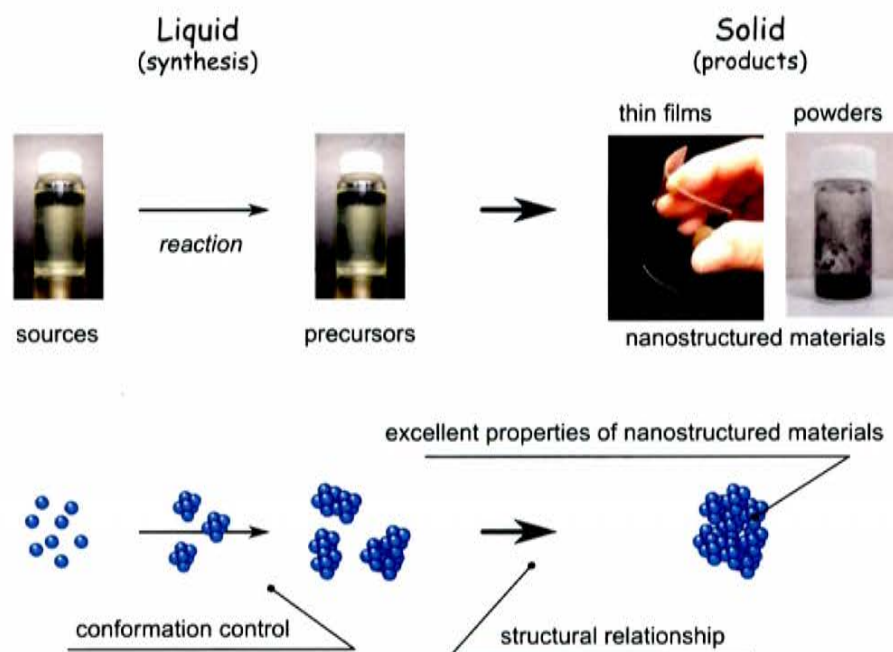
Scheme 8.1. The manifestation and achievement on this study through the nanostructured materials fabrication.

Chapter 2 presented fabrication of microporous silica from tetramethyl orthosilicate (TMOS) using the catalytic sol–gel process based on the non–ionic hydroxyacetone catalyst. Small angle X-ray scattering (SAXS), nitrogen adsorption porosimetry, and transmission electron microscope (TEM) allowed to observe the whole structural evolution, ranging from polymer-like aggregates in the precursor solution, agglomeration with heat treatment and microporous morphology of silica powders after drying and hydrolysis. Using the hydroxyacetone (HA) catalyst with short chain monohydric alcohols (methanol or ethanol) in the precursor

solution, polymer-like aggregates having microscopic correlation length (or mesh-size) < 2 nm and low fractal

dimensions $d_f \approx 2$ which is identical to that of an ideal coil polymer, were selectively synthesized, yielding the

uniform micropores with diameters < 2 nm in the solid materials. In contrast, the absence of HA or substitution

of 1-propanol led to considerably different scattering behavior reflecting the particle-like aggregate formation in

the precursor solution, which resulted in the formation of mesopores (diameter > 2 nm) in the solid product due

to apertures between the particle-like aggregates. The data demonstrated that the extremely fine porous silica

architecture comes essentially from a Gaussian polymer-like nature of the silica aggregates in the precursor

having the microscopic mesh-size and their successful imprint on the solid product.

From the perspective of an applicative aspect, the microporous silica thin films were fabricated from the

silica precursor solution synthesized from TMOS via the catalytic sol–gel process (Chapter 3 and 4). The

refractive indices were characterized by means of spectroscopic ellipsometry, and simultaneously, a typical

elastic modulus was measured by nanoindentation (in Chapter 3). The microporous silica thin film presented a

low refractive index (low-n) of 1.27 and a high Young's modulus of 19.5 GPa, The high mechanical strength of

resultant microporous thin films was considered to be provided, thanks to their extremely small and uniform

micropores. Unlike other microporous synthesis methods, this method did not require sacrificial reagents as

templates. This enabled low temperature fabrication of high-strength low-n silica.

The generation of superhydrophilicity on the microporous silica film was discussed in Chapter 4. This

section demonstrated that low-temperature fabrication, $T \approx 80$ °C, of superhydrophilic silica thin films having a

huge number of micropores exposed on the extremely smooth surface. Also, the superhydrophilic microporous

silica film was able to be formed on a polyethylene terephthalate substrate. The small pores ($d < 1$ nm)

embedded in the surface of the films were able to absorb water from the air and could be not easy to desorb

them. Owing to a lot of waterbearing micropores on the flat surfaces, the hydrophilicity of the silica coating

were expected to be enhanced.

As for amorphous titania material, in Chapter 5, the rapid generation and growth (within hours) of low–fractal dimension titania polymers derived from titanium-n-butoxide via the catalytic sol–gel process with the hydrazine monohydrochloride catalyst was confirmed by the time-resolved small angle X-ray scattering. It was confirmed that the generated titanium oxide polymers possess the expanded chain-like fractal architecture ($d_f \approx 5/3$) with local rod–like structure. The low fractal dimension titania polymers gave a highly transparent solution without light scattering. The results exhibited the efficient fabrication of the low–fractal dimension titanium oxide polymers, highly transparent solutions.

In Chapter 6, the amorphous dense titania film with a high refractive index (>2.1) was fabricated from low–fractal dimension ($d_f \approx 5/3$) titanium oxide precursor solutions below 60°C. This result revealed that the smaller correlation length $\xi \approx 2$ nm showed a higher refractive index, n, which reached 2.074 and 2.139 (at $\lambda =$ 633 nm) after heat–treatment at 60 and 80°C, respectively. Also, the amorphous titania film was successfully coated on PMMA with low temperature (60 °C) heat–treatment; $n = 2.064$ (at $\lambda = 633$ nm). Like the results of the sol–gel derived silica solid materials (Chapter 2), the microstructure of the solid titania materials were expected to reflect that of liquid precursors significantly. It believed that the expanded chain-like titanium oxide polymers produced the highly dense solids through mutual interpenetration during the drying and curing processes.

In the last chapter, the platinum nanowire network (approximate ⌀ 4 nm) with silica nanoparticle (Pt_{net}/SiO_2) spacers was prepared via spray drying and hydrogen reduction. Different from the conventional metal oxide supported platinum nanoparticles, the characteristic nanostructure of platinum nanowire network required no electric conductivity from the support materials because of their own electricity-conducting network. The nanowire network had a high electrochemical surface area (31.3 m^2 g_{Pt}^{-1}), and acted as a catalyst for the oxygen reduction reaction. Its initial mass activity (110.5 A g_{Pt}^{-1} at 0.85 V_{RHE}) was high compared to commercial Pt/C catalyst (100.2 A g_{Pt}^{-1} at 0.85 V_{RHE}). Because of the chemical stability of the silica and the

minimal amount of low-coordinated platinum in the platinum nanowires, Pt_{net}/SiO_2 retained 77 % of its initial

activity after 27 000 cycles compared to 57 % for commercial Pt/C.

The nanostructural relationships between precursors and solids revealed throughout this study can be

expected to contribute to the development of synthesis technique and design of various nanostructured

materials.

List of Accomplishments

Publications Associated with This Study

1. <u>Wataru Shimizu</u>, Taki Matsumoto, Shohei Hosoo, Hitoshi Nagahira, and Yasushi Murakami, Superhydrophilic Microporous Silica Coatings on Polymer Substrate, Journal of the Ceramic Society of Japan 2007, 115, 712-716.

2. <u>Wataru Shimizu</u> and Yasushi Murakami, Microporous Silica Thin Films with Low Refractive Indices and High Young's Modulus, ACS Applied Materials and Interfaces 2010, 2, 3128-3133.

3. <u>Wataru Shimizu</u>, Junsuke Hokka, Takaaki Sato, Hisanao Usami, and Yasushi Murakami, Microstructure Investigation on Micropore Formation in Microporous Silica Materials Prepared via a Catalytic Sol–Gel Process by Small Angle X-Ray Scattering, The Journal of Physical Chemistry B 2011, 115, 9369-9378.

4. <u>Wataru Shimizu</u>, Kazuyoshi Okada, Yoshitaka Fujita, ShanShan Zhao, and Yasushi Murakami, Platinum Nanowire Network with Silica Nanoparticle Spacers for Use as an Oxygen Reduction Catalyst, Journal of Power Sources (in press).

5. <u>Wataru Shimizu</u>, Takaaki Sato, Taki Matsumoto, and Yasushi Murakami, Rapid Synthesis of Low-Fractal Dimension Titanium Oxide Polymers by a Sol–Gel Technique using Hydrazine Monohydrochloride, Journal of Nanoscience and Nanotechnology (in press).

Acknowledgements

Wataru Shimizu

March 21, 2012